Fundamental Study on Si Nanowires for Advanced MOSFETs and Light-Emitting Devices

2010

Hironori Yoshioka

Abstract

Since nanotechnology made it possible to fabricate and control structures with dimensions much smaller than 1 μm, physical phenomena peculiar to the nanoscale structures have attracted much attention and have been expected to be utilized in novel devices. Si nanowires (NWs) are one of the structures: quantum confinement effect (QCE) becomes conspicuous in Si NWs, and Si NWs are potential structures for applications to advanced metal-oxide-semiconductor field effect transistors (MOSFETs) and light-emitting devices.

Although Si MOSFETs have made progress with miniaturization according to the scaling law so far, further scaling will not be easy in the future because of problems such as short channel effects. To overcome the problems, surrounding-gate structures such as NW MOSFETs have been proposed. The structures can control the short channel effects effectively. Unlike bulk Si, Si nanostructures including Si NWs are promising candidates of light-emitting devices, because the QCE in nanostructures increases the uncertainty of the crystal momentum, by which no-phonon radiative recombination may increase, and with which improvement in light-emitting efficiency is expected.

In this thesis, first, a fabrication process of Si NWs with a cross-sectional size below 10 nm is established, and then carrier transport characteristics in Si NW MOSFETs were studied. The size dependence of the mobility was investigated, from which the electronic states and the carrier scattering mechanism peculiar to Si NWs were inferred. Moreover, to clarify the origin of the current oscillation with gate-voltage sweep in NW MOSFETs, the author proposed an analytical transport model, taking account of acoustic phonon scattering in Si NWs. In addition to the transport characteristics, the optical properties of Si NWs were also studied, aiming at light-emitting diodes. The light-emitting properties of Si NWs were estimated by calculating the absorption coefficients for band-to-band transition. Si-NW pn-diodes were fabricated, and their electroluminescence was investigated.

In Chapter 2, a fabrication process of Si NWs by a top-down approach using silicon-on-insulator, electron beam lithography and sacrificial oxidation was established. The NW shapes were investigated by cross-sectional and top views using TEM and SEM. Formation of NWs as narrow as 13 nm was accomplished by electron beam lithography. After downsizing by sacrificial oxidation, formation of an NW with a minimum cross-sectional size W (square root of the area) of 4 nm (height: 2 nm, width: 7 nm) was achieved.

In Chapter 3, Si-NW MOSFETs, whose NW size (W) was changed from 18 nm to 4 nm, were characterized. Both n- and p-channel MOSFETs showed good gate control with a nearly ideal subthreshold swing of 63 mV/decade. The shift of subthreshold voltage with decreasing the NW size was observed and can be explained by the band-edge shift by the QCE. Electron and hole mobilities were compared and characterized in one Si NW using a special device structure. The W dependence of the ratio of the electron and hole mobilities indicated two types of

carrier-confinement conditions: electric-field-confinement and volume-inversion. For electric-field-confinement condition (W > 7 nm), mobility was explained by the combination of bulk-MOSFET mobility with different channel faces. For volume-inversion condition (W < 7 nm), mobility decreased, and the decrease probably originates in the increase of the surface-roughness scattering. The mobility ratio changed remarkably, which may originate in the unique band structure of NW.

In Chapter 4, the drain-current oscillation peculiar to NW MOSFETs was experimentally and theoretically investigated. The transconductance of a fabricated Si-NW MOSFET with W = 6 showed clear oscillation up to 309 K. A transport model that reproduces the drain-current oscillation was proposed. The model assumes one-dimensional electronic states determined from the effective mass approximation as well as elastic and isotropic phonon scattering. The mobility was calculated from the relaxation time approximation as a function of the Fermi level and the carrier concentration was also determined as a function of the Fermi level. Relation between the gate voltage and the Fermi level was estimated from the MOSFET structure, by which the gate-voltage dependence of the carrier mobility and the concentration in Si NW MOSFETs was calculated. The calculated results showed similar oscillation to the experimental results. The model indicates that the oscillation originates from the periodic variations in the scattering rate caused by one-dimensional density of states ($\propto E^{-0.5}$), and one set of peak and valley of the oscillation reflects one subband.

In Chapter 5, to reveal optical properties of Si NWs, the author calculated the electronic states and absorption coefficient by direct band-to-band transition of <100> and <111> Si NWs with a W of about 1-3 nm by the density functional theory. The band-gap energy increased with a decrease in size as a result of QCE effects. The <100> NWs showed direct band structure, while the band structure of <111> NWs changed from indirect to direct with decrease in size. The near-band-edge absorption-coefficient of <100> NWs with a size below about 2 nm for the polarization being parallel to NW was larger than that of the experimental results of the bulk and increased remarkably with decrease in size. The <111> NWs showed a smaller absorption coefficient than the <100> NWs. Therefore, the <100> NWs with a size below about 2 nm are attractive from the standpoint of efficient luminescence. The absorption edge for the perpendicular polarization shifted to the higher energy side than the band gap energy because of the forbidden transitions.

In Chapter 6, Si-NW pn diodes were fabricated and the dependence of the electroluminescence on the NW size was investigated. For the diode with an expected W of 88 nm, a single peak at 1.092 eV was observed, which undoubtedly originates in the emission by band-edge transition in bulk-wire Si. For the diodes with expected W smaller than 31 nm, three peaks were observed. The peak energies were 1.104 eV, 1.050 eV, and about 1.0 eV for an expected W of 9 nm. Since the energy 1.104 eV is slightly larger than bulk-Si energy of 1.092 eV, the peak at 1.104 eV perhaps originates in band edge transition in Si NWs with the band gap widened by QCE.

In Chapter 7, conclusions of the present study are given with suggestions for future work.

Acknowledgements

I would first like to express my most sincere gratitude to Professor Tsunenobu Kimoto for providing me the opportunity to accomplish this work and for his continuous guidance, invaluable advice, supervision, and ceaseless encouragement through fruitful discussions.

I would like to acknowledge Professor Shizuo Fujita and Associate Professor Hirofumi Yamada for their valuable advice and critical comments on this dissertaion.

I am deeply grateful to Mr. Eiji Ohmura of Kyoto-Advanced Nanotechnology Network, Kyoto University, supporting me in the device fabrication process of electron beam lithography. I would like to thank Associate Professor Jun Suda for constructive advice and support of my work, especially setup and maintenance of the computer system for calculation by the density functional theory. I am also indebted to Research Associate Yusuke Nishi for supporting of my experiments. I woud like to thank Associate Professor Mitsuru Funato for help in using focused ion beam systems and scanning electron microscopy. I would like to thank Dr. Hiroshi Yano, Research Associate of Nara Institute of Science and Technology, for allowing me to use a low-temperature prober system.

I am indebted to Mr. Yuichiro Nanen and Mr. Naoya Morioka for helping my work in part and valuable discussion on Si nanowire or MOSFETs with three-dimensional gate structure.

I would lile to express my deep appreciation to Dr. Masato Noborio and Dr. Masahiro Horita for their helpful comments and support for handling experimental equipment as well as sharing meaningful university life for three years. I have benefited significantly from meaningful discussion about many fields and support for handling experimental equipment by Dr. Atsushi Koizumi, Dr. Giovanni Alfieri, Dr. Katsunori Danno, Mr. Koichi Amari, Mr. Katsuhiko Fukunaga, Mr. Ryota Suzuki, Mr. Kei Senga, with warmly welcoming me. I would like to thank Dr. Gan Feng, Mr. Toshihiko Hayashi, Mr. Hironori Okumura, Mr. Hiroki Miyake, Mr. Toru Hiyoshi, Mr. Kazuki Yamaji, Mr. Koutarou Kawahara, Mr. Naoki Watanabe, Mr. Tatsuya Iwata, Mr. Shunsaku Ueta, Mr. Yuichirou Hayashi, Mr. Yibo Zhang, Mr. Muneharu Kato, Mr. Ryohei Kanno, Mr. Ryosuke Kikuchi, Mr. Sho Sasaki, and all of the Semiconductor Science and Engineering Laboratory for sharing meaningful time with their kindness and support.

I wish to thank Ms. Yoriko Ohnaka and Ms. Mizuki Yamada who support me by daily work. This work was financially supported in part by the 21st century COE program (No. 14213201) and the Grobal COE program (C09) from the Ministry of Education, Culture, Sports, Science, and Technology, Japan.

Finally, I am grateful to my parents, sisters, and all of my friends for their understanding, continuous care, support, and heartfelt encouragemet.

June, 2010

Hironori Yoshioka

Contents

Chapter 1

Introduction

1.1 Background

Technology products have been changing and improving our lives. Personal computers, the Internet, mobile phones, car navigation systems, and electronic dictionaries are examples from recent years. Such technological innovations are largely based on miniaturization of devices, by which larger information can be processed, transmitted, and stored faster in a smaller space with lower electric energy. In spite of efficiency improvement, total electric-energy consumption has been increasing because of the infinite demand of dealing with more and more information. "BRICs," which refer to the fast-developing nations of Brazil, Russia, India and China, have become a very popular term nowadays. Such large economic growth increases anxiety about exhaustion of energy resources and global environmental change. Therefore, sustainable development is strongly needed, which, of course, is of great interest in the fields of science and technology.

Nanotechnology has been developed with device miniaturization and made it possible to fabricate and control structures with dimensions much smaller than 1 μm. Physical phenomena peculiar to such nanoscale structures, like ballistic transport or Coulomb blockade, have attracted much attention and have been expected to be utilized in novel devices. Si nanowires (NWs) are one of the structures: quantum confinement effect (QCE) becomes conspicuous in Si NWs, and Si NWs are potential structures for applications to advanced metal-oxide-semiconductor field effect transistors (MOSFETs) and light-emitting devices.

Large-scale integrated circuits (LSIs) based on Si MOSFETs are widely used in electronic equipment and are also applied to home appliances, that is "digital appliances." The market is worth about 200 billion US dollars a year worldwide [1]. The LSIs have been increasingly miniaturized in accordance with the Moore's law. G. Moore predicted in 1965 that the number of transistors per chip would increase four times every three years [2]. A MOSFET first reported in 1960 had a gate length of 20 μm and a gate oxide thickness of 100 nm [3]. By the progress of minute processing technology, the gate length of the latest MOSFETs has reached less than 50 nm. However, further scaling will not be easy in the future because of many problems. New structures, concepts, or materials are needed to evolve the devices further, which is expressed by the slogans "more than

Moore" or "beyond CMOS." Si NWs are one of the potential materials to be used in the LSIs and improve the performance by the structural characteristics. Since the Si NWs for such application would have a small cross-sectional size of below about 10 nm, QCE must undoubtedly be managed.

Unlike bulk Si, Si NWs are promising candidates of light-emitting devices, because the QCE in nanostructures increases the uncertainty of the crystal momentum, with which improvement in light-emitting efficiency is expected.

1.2 Properties of Si

1.2.1 Bulk

Crystal structure and phonon dispersion

A bulk-Si crystal has a diamond-lattice structure (space group: 227, O_h^7, $Fd\bar{3}m$ [4]), of which lattice constant a is 0.543 nm at room temperature [5-7]. Figure 1.1 shows the phonon dispersion for Si [8]. The symbol and position of the high symmetry points are summarized in Table 1.1. There are six modes: one longitudinal acoustic, two transverse acoustic, one longitudinal optical, and two transverse optical modes. Velocity of longitudinal acoustic and transverse acoustic phonons is 9×10^3 $m\cdot s^{-1}$ and 5×10^3 $m\cdot s^{-1}$, respectively. The energy of optical phonons is 63 meV at Γ.

Band structure

The bulk-Si crystal is a semiconductor with an indirect band-gap and the energy is 1.12 eV at 300K [9]. Figure 1.2 shows the band structure calculated by the pseudopotential method [10], where the parameters are determined to fit experimental data such as optical gaps. Figure 1.3 shows the constant energy surfaces near the conduction band minimum (CBM) and valence band maximum (VBM) [11]. There are six equivalent CBMs located at 0.85X. Near the CBMs, the constant energy surface is a spheroid and the E-k dispersion relation can be well approximated by a quadratic using two electron effective masses: m^*_T (= $0.19m_0$) and m^*_L (= $0.98m_0$) [12]. The VBM is located at Γ and consists of doubly degenerate bands named heavy-hole band and light-hole band. As shown in Fig. 1.3, for both the heavy-hole and light-hole bands, the constant energy surface is warped and the E-k relation cannot be accurately approximated by a quadratic, which makes hole transport difficult to treat. To treat it simply, it is roughly assumed that the bands are spherical and parabolic, and one effective mass for each band is derived based on the assumption: heavy-hole effective mass m^*_H (= $0.53m_0$ [13] or $0.49m_0$ [14]) and light-hole effective mass m^*_L (= $0.16m_0$ [13, 14]). Near the VBM, there is another band named the split-off band, which is separated from VBM by only −44 meV at Γ [15] and can also play a role in hole transport.

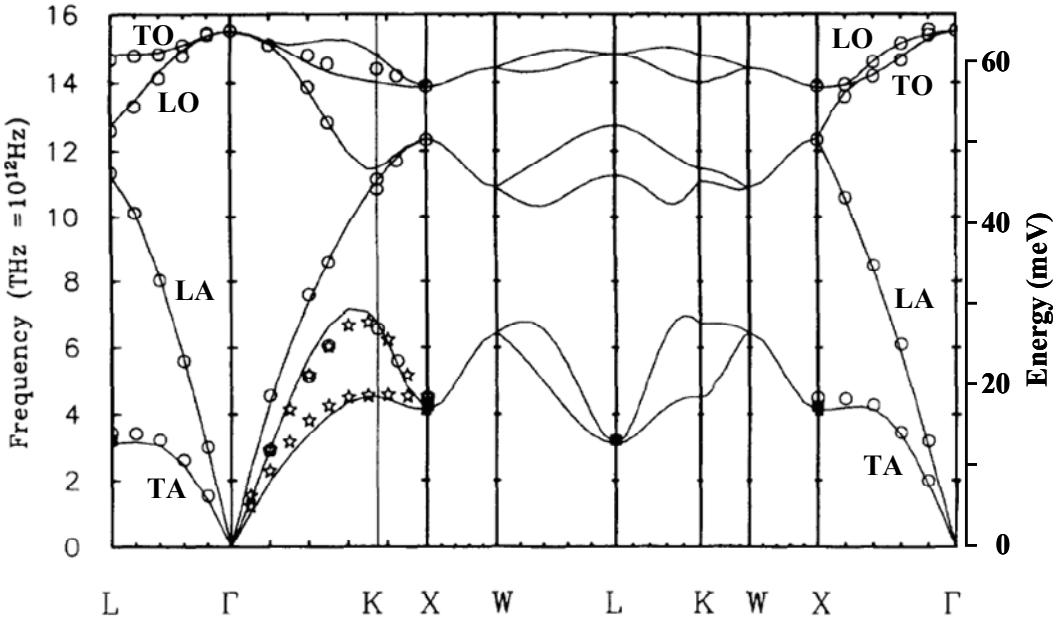

Fig. 1.1 Phonon dispersion relation for bulk Si. Solid lines are calculated results, and circles and stars are experimental results. (Reproduced from Ref. [8].)

Table 1.1 Symbol and position of high symmetry points in reciprocal lattice.

Symbol	Position
Γ	$\frac{2\pi}{a}(0,0,0)$
L	$\frac{2\pi}{a}(1/2,1/2,1/2)$
X	$\frac{2\pi}{a}(1,0,0)$
K	$\frac{2\pi}{a}(3/4,3/4,0)$
W	$\frac{2\pi}{a}(1/2,1,0)$
U	$\frac{2\pi}{a}(1,1/4,1/4)$

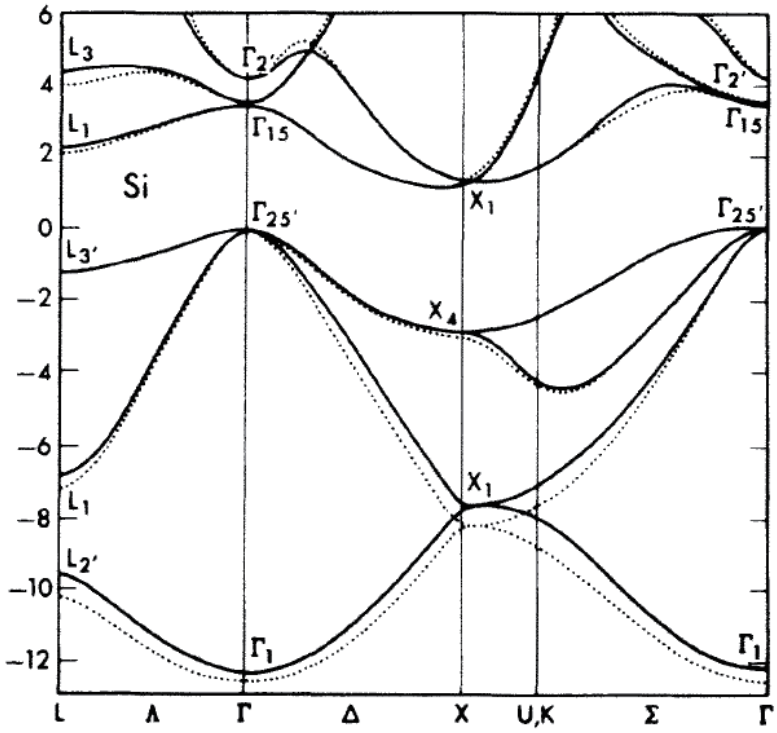

Fig. 1.2 Band structure of bulk Si calculated by the pseudopotential method, where two results of solid and dashed lines are shown. (Reproduced from Ref. [10].)

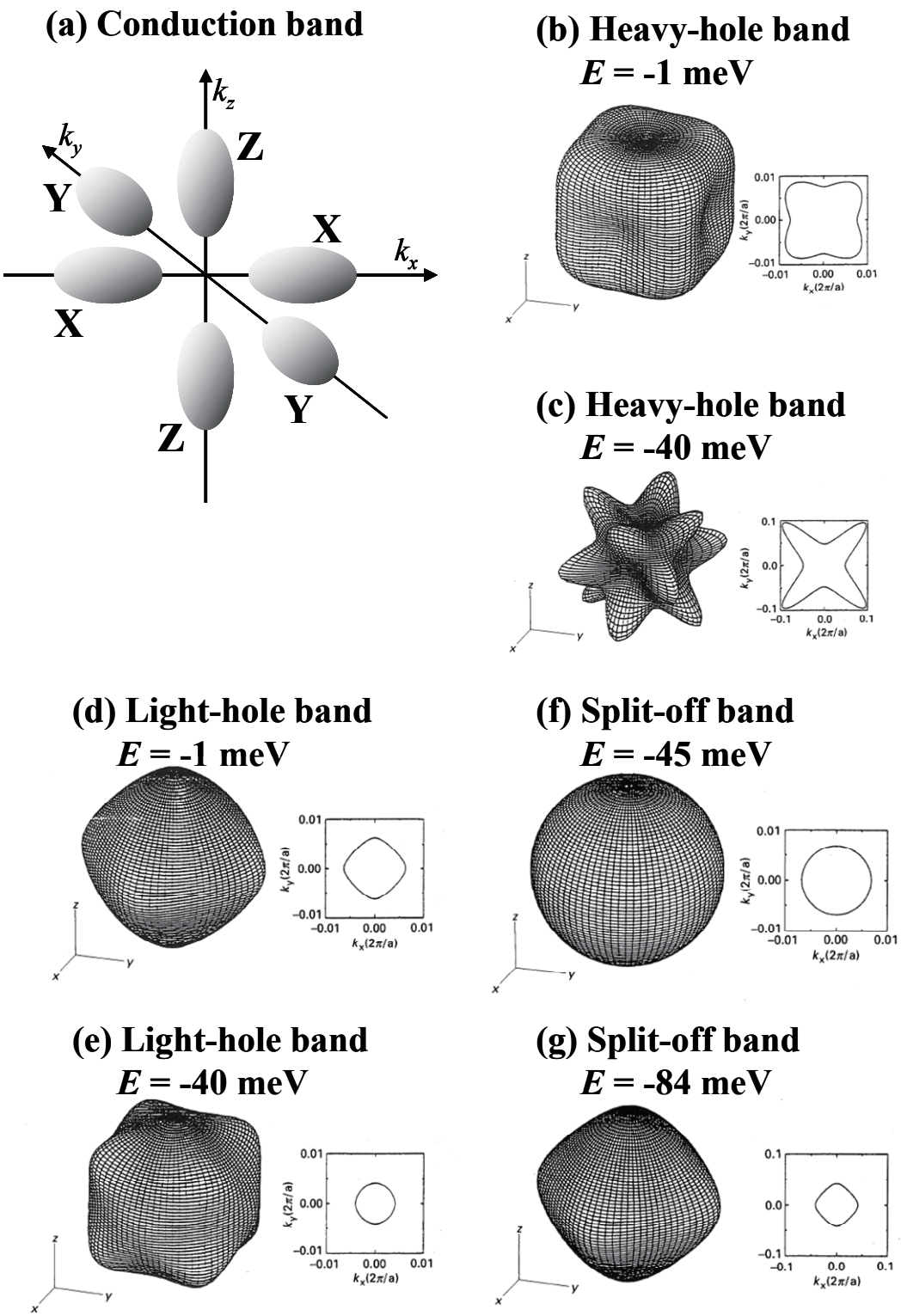

Fig. 1.3 Shapes of constant-energy surfaces for (a) conduction, (b, c) heavy-hole, (d, e) light-hole, and (f, g) split-off bands. ((b-g) are reproduced from Ref. [11]. The scale value of the right figure in (e) is probably not 0.01 but 0.1.)

Bulk mobility

Mobility of bulk Si is 1.4×10^3 $cm^2V^{-1}s^{-1}$ for electrons and 4.7×10^2 $cm^2V^{-1}s^{-1}$ for holes at room temperature and impurity concentration of as low as 10^{14} cm^{-3} [16, 17]. Coulomb scattering by the ionized impurities significantly decreases the mobility, when the impurity concentration exceeds about 10^{16} cm^{-3} (Fig. 1.4). Temperature dependence of the mobility for the low impurity concentration is shown in Fig. 1.5 [18-20]. The mobility near room temperature varies with temperature as $\mu \propto T^{\alpha}$, where the fitting parameter α is in the range of −2.0 to −2.5 for both electrons and holes [18, 19, 21]. Mobility of acoustic phonon scattering involving small-energy acoustic-phonons is theoretically expected to vary as $\propto T^{-1.5}$. Although the acoustic phonon scattering is dominant in the bulk Si at relatively low temperature, the temperature dependence of the bulk-Si mobility near room temperature is larger than the theoretical dependence of the acoustic phonon scattering because of other scattering mechanisms. Electrons are scattered from one CVM to another by acoustic or optical phonons, which is termed intervalley scattering. Nonpolar-optical-phonon scattering occurs for holes. (It does not occur for electrons by a selection rule.) Since these kinds of scattering involve phonons with as high as several tens of meV, the scattering is enhanced above about 100 K and is as frequent as the acoustic phonon scattering near room temperature [19].

Channel mobility of bulk MOSFETs

Mobility in an inversion layer of bulk-Si MOSFETs has dependence on electric field normal to the interface, which is expressed by

$$\mu \propto E_{\mathrm{eff}}{}^{\beta} \tag{1.1}$$

at E_{eff} lower than about 0.5 $MV\cdot cm^{-1}$ and low impurity concentration near room temperature, where the fitting parameter β is about −0.3 for electrons on {100}, {110}, and {111}, and holes on {100} [22-25]. E_{eff} is the effective field defined by

$$E_{\mathrm{eff}} = \frac{e}{\varepsilon_{\mathrm{Si}}}\left(N_{\mathrm{D}} + \eta N_{\mathrm{I}}\right), \tag{1.2}$$

where $\varepsilon_{\mathrm{Si}}$, N_{D}, and N_{I} are the dielectric constant of Si, concentration of depletion-layer impurities, and concentration of inversion-layer carriers, respectively. The parameter η is set so that the mobility is independent of impurity concentration or substrate bias when the mobility is plotted as a function of E_{eff}. By this method, the η is set to be 1/2 for electrons on {100}, 1/3 for electrons on {110} and {111}, and 1/3 for holes on {100} [22-24, 26, 27]. It is explained in Ref. 16 that the mobility is mainly determined by acoustic phonon scattering, and the β and η are theoretically derived to be −1/3 and 11/32, respectively, by assuming that the carriers in the inversion layer are two-dimensional electron gas and are only scattered by acoustic phonons. Large deviation of {100}-electrons' η (= 1/2) from the theoretical value may originate from nonequivalent CBMs in the inversion layer, which is discussed in [24, 25]. Figure 1.6 shows the effective field dependence

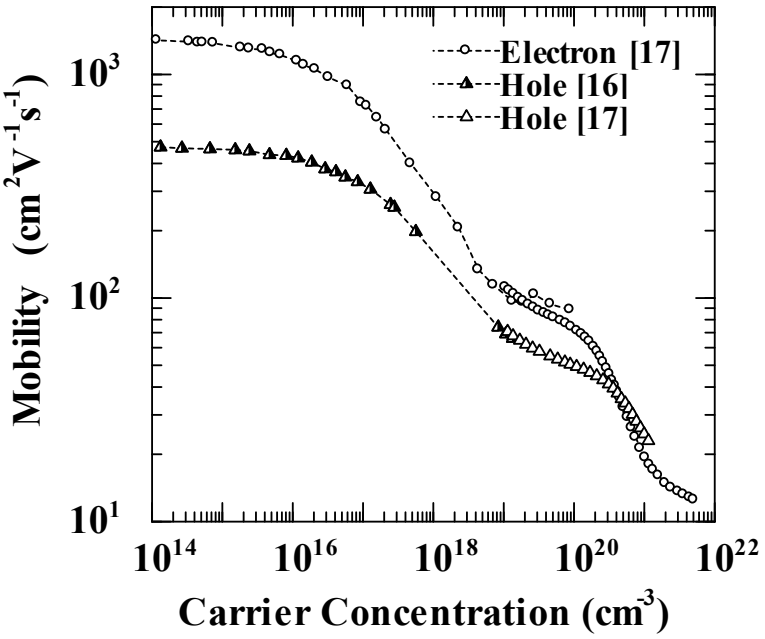

Fig. 1.4 Mobility of electrons and holes as a function of carrier (ionized impurity) concentration [16, 17].

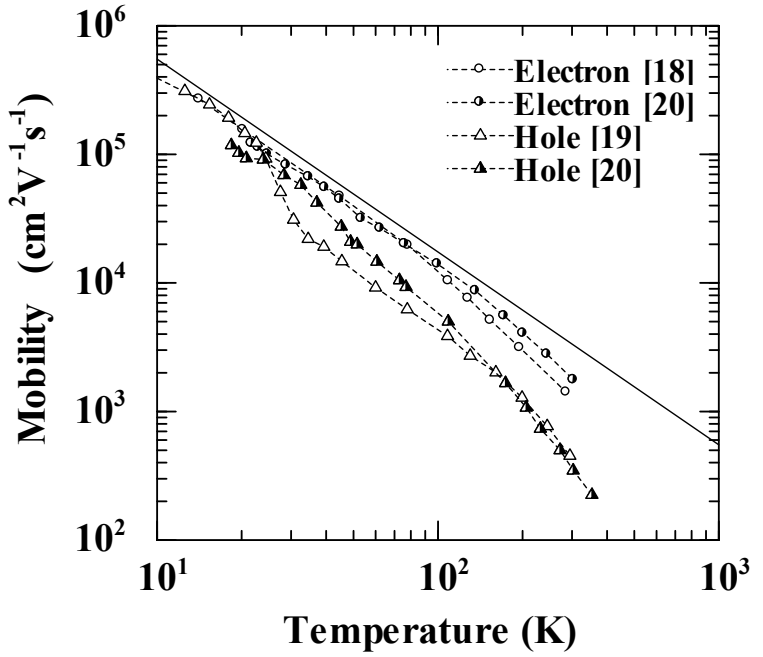

Fig. 1.5 Mobility of electrons and holes as a function of temperature [18-20]. The solid line shows temperature dependence of $\propto T^{-1.5}$.

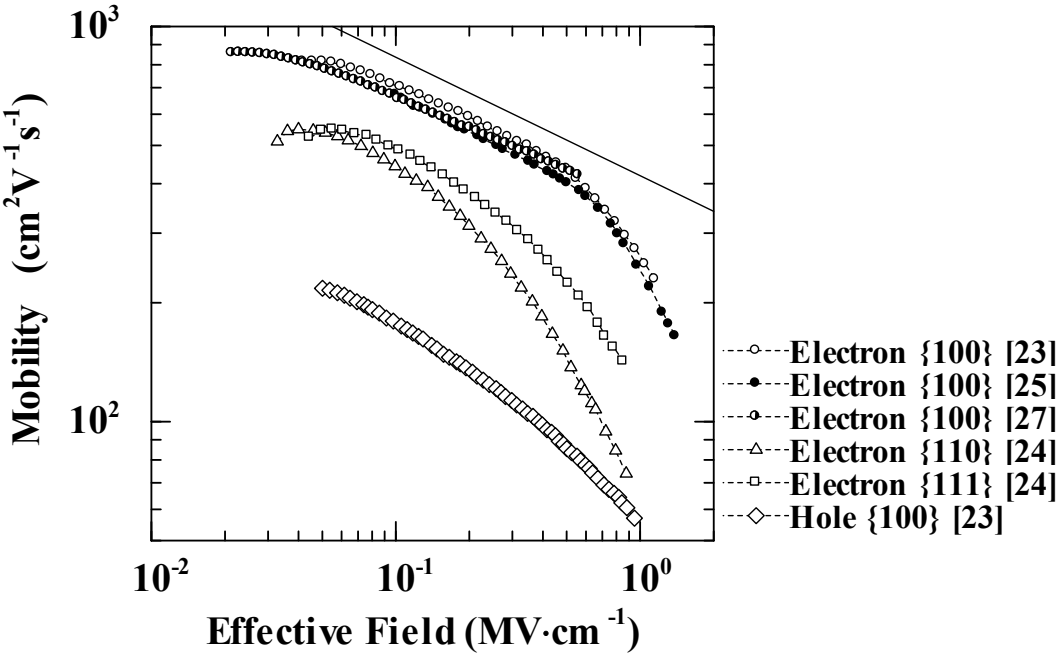

Fig. 1.6 Mobility in an inversion layer of bulk-Si MOSFET as a function of effective field, where the η is set to be 1/2 for electrons on {100}, 1/3 for electrons on {110} and {111}, and 1/3 for holes on {100} [23-25, 27]. The solid line shows effective-field dependence of $\propto E_{\mathrm{eff}}{}^{-0.3}$.

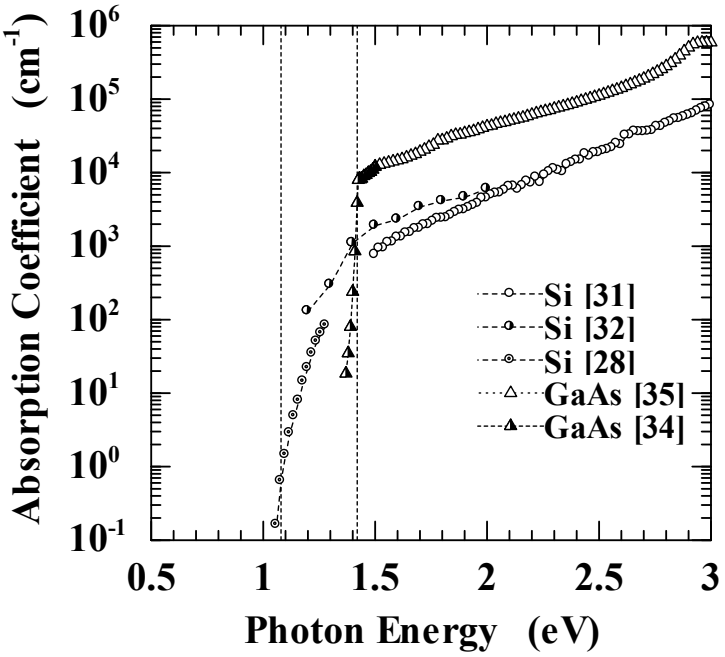

Fig. 1.7 Absorption coefficient for Si and GaAs near band-gap energy [28, 31, 32, 34, 35]. The broken lines show band-gap energy of Si (1.08 eV) and GaAs (1.42 eV).

of the mobility [23-25, 27]. At E_{eff} larger than about 0.5 MV·cm^{-1}, surface-roughness scattering significantly decreases the mobility with increase of the electric field, and its degree is varied by the surface orientation [24, 25, 27]. The mobility on {100} is largest for electrons. The Coulomb scattering becomes dominant for high impurity concentration and low electric field, but decreases with increase in carrier concentration because of the screening effect [23, 24, 27].

Absorption coefficient

Si is an indirect-band-gap semiconductor and optical transitions involve phonons [28]. The involved phonons are longitudinal acoustic, transverse acoustic, longitudinal optical, and transverse optical phonons with energy of 46.5 meV, 18.2 meV, 55.3 meV, and 57.5 meV, respectively [29, 30]. Figure 1.7 shows the absorption coefficient of Si near band-gap energy [28, 31-33], where the band-gap energy is 1.08 eV at 300K [28]. The absorption coefficient of direct-gap GaAs is also shown in the figure for reference [33-35]. The absorption coefficient of indirect-gap Si at band-gap energy is far smaller than that of direct-gap GaAs. Therefore, bulk Si is a less attractive material for light-emitting devices.

1.2.2 Nanowire

Band structure

In Si NWs, carriers are confined and energy subbands are formed. First, the concepts will be reviewed by using the simplest model [36]. It is assumed that an Si NW is square in the cross section, the crystalline orientations and the coordinate axes are set as shown in Fig. 1.8, and carriers in the Si NW are confined in the *y*- and *z*-directions by an infinite quantum well of width *W* and are free to move in the *x*-direction. The Schrödinger equation using the effective mass approximation (EMA) is solved and the envelope function Ψ and energy E for electrons in each CBM denoted by labels of X, Y, and Z as in Fig. 1.3(a) are given by

$$\begin{aligned}\Psi_{\mathrm{X}}(x,y,z) &= \sin\left(\frac{n_y\pi}{W}y\right)\sin\left(\frac{n_z\pi}{W}z\right)\exp\left(i\left(k_x-k_0\right)x\right)\\ \Psi_{\mathrm{Y}}(x,y,z) &= \sin\left(\frac{n_y\pi}{W}y\right)\sin\left(\frac{n_z\pi}{W}z\right)\exp\left(ik_x x\right)\end{aligned}, \tag{1.3}$$

$$\begin{aligned}E_{\mathrm{X}}(n_y,n_z;k_x) &= E_{\mathrm{C}}+\frac{\hbar^2}{2m^*_{\mathrm{T}}}\left(\frac{n_z\pi}{W}\right)^2+\frac{\hbar^2}{2m^*_{\mathrm{T}}}\left(\frac{n_y\pi}{W}\right)^2+\frac{\hbar^2}{2m^*_{\mathrm{L}}}\left(k_x-k_0\right)^2\\ E_{\mathrm{Y}}(n_y,n_z;k_x) &= E_{\mathrm{C}}+\frac{\hbar^2}{2m^*_{\mathrm{T}}}\left(\frac{n_z\pi}{W}\right)^2+\frac{\hbar^2}{2m^*_{\mathrm{L}}}\left(\frac{n_y\pi}{W}\right)^2+\frac{\hbar^2}{2m^*_{\mathrm{T}}}k_x{}^2\end{aligned}, \tag{1.4}$$

$$n_y, n_z = 1,2\ldots,$$

where E_{C} is the energy of bulk CBMs, k_x is the wave number, and k_0 is $0.15(2\pi/a)$ or $-0.15(2\pi/a)$. Since the Y-CBMs and Z-CBMs remain degenerate to each other, only the equations for Y-CBMs

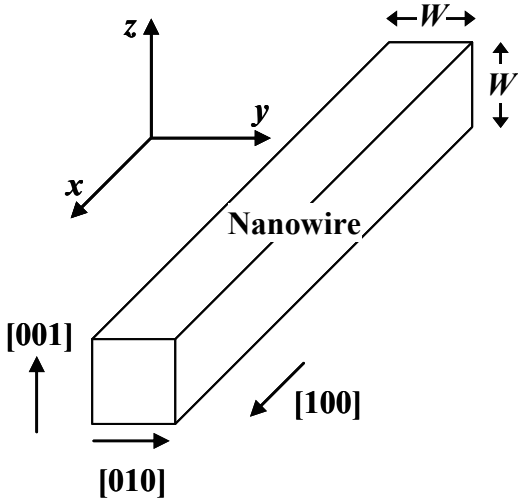

Fig. 1.8 Shape and crystalline orientations of a nanowire and the coordinate axes for the calculations using EMA.

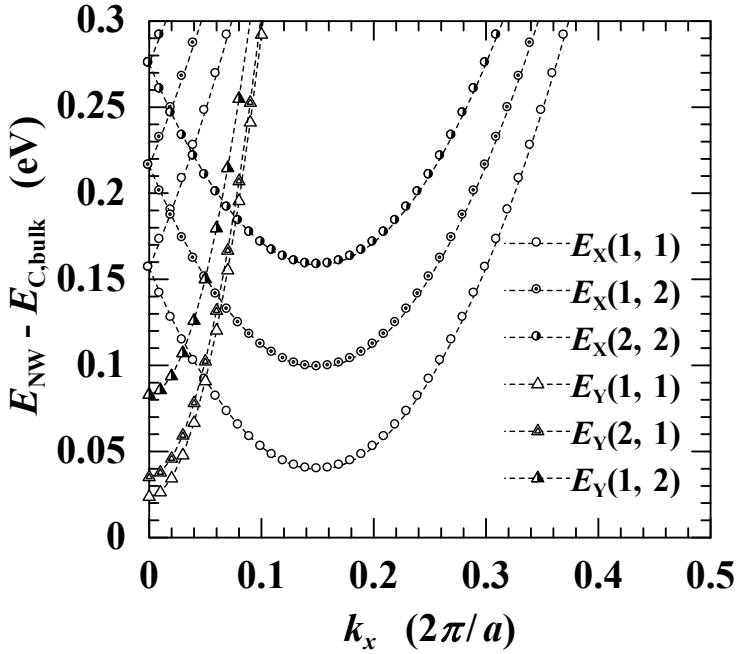

Fig. 1.9 E-k_x relation of the conduction band for the Si [100] NW (W = 10 nm) calculated by EMA, where the first to third lowest subbands for each CBM are plotted.

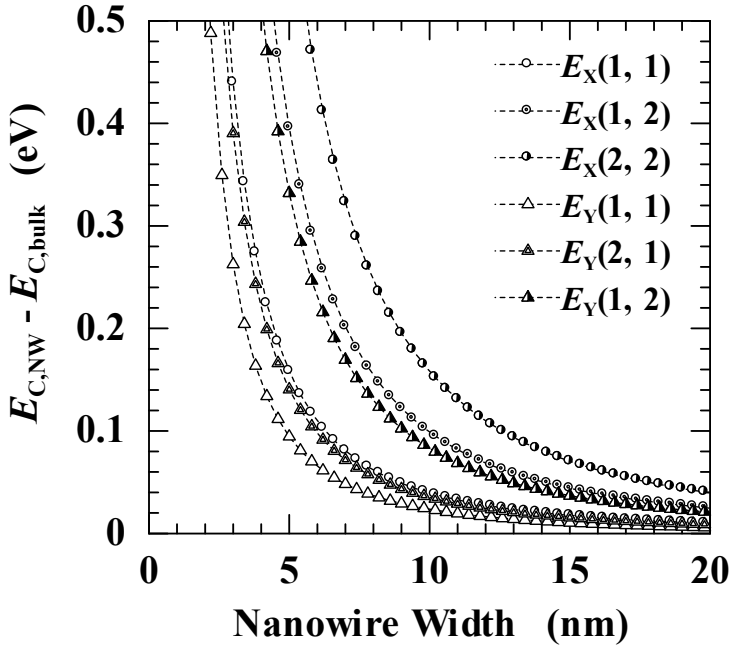

Fig. 1.10 Minimum energy of subbands for Si [100] NW as a function of width W, where the first to third lowest subbands for each CBM are plotted.

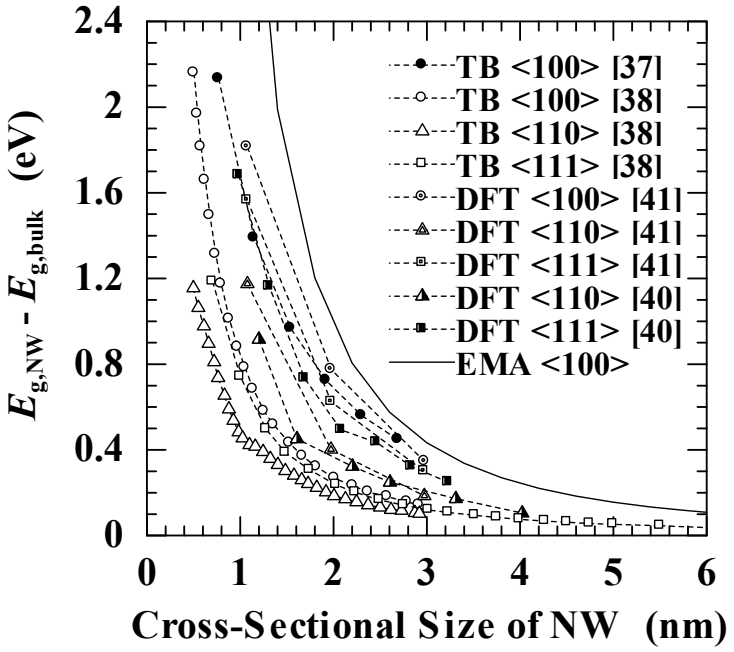

Fig. 1.11 Band-gap energy of Si NWs with different directions calculated by TB [37, 38], DFT [40, 41], and EMA as a function of the NW's cross-sectional size.

are presented. Energies specified by a set of (n_y, n_z) form an energy subband. The E-k_x relation is shown in Fig. 1.9, where a line denotes a subband, and the relation can be viewed as a projection of three-dimensional E-k relation of bulk on the k_x-axis. (The coefficient in k_0 is not only 0.85 but also 0.15 because X-CBMs with 0.15 exist outside the first Brillouin zone.) Degeneracy of X-CBMs and Y-CBMs is broken by anisotropy of effective mass. The minimum energy of the subbands is plotted as a function of the width W in Fig. 1.10, where the first to third lowest subbands for each CBM are plotted. The subband minima shift to the higher energy side with decrease of the width and separate from each other (subband splitting). In the same way, the subbands' minimum energies of the heavy-hole and light-hole bands can also be calculated using m^*_H (= $0.49m_0$) and m^*_L (= $0.16m_0$). The subband maxima shift to the lower energy side with decrease of the width, and the band gap E_g [= $E_Y(1, 1; 0)-E_H(1, 1; 0)$] widens. The subband splitting changes the population rate of carriers in each subband and results in change of conductivity effective mass. For example, the lowest subband in the conduction band, $_Y(1, 1)$, has most of electron population and has small effective mass m^*_T in the x-direction (direction of carrier transport). That is to say, the conductivity effective mass in the NW approaches m^*_T (= $0.19m_0$) with decrease of the width, while that in the bulk is $3m^*_L m^*_T/(2m^*_L+m^*_T)$ (= $0.26m_0$). Such effects of the subband splitting on carrier transport become conspicuous when the splitting energy becomes sufficiently larger than thermal energy kT. The splitting energy with an NW width of about 10 nm is equivalent to the thermal energy at room temperature (26 meV). The subband splitting also changes the density of states (DOS). The DOS in the NW is the sum of the subband DOSs, which are given as one-dimensional DOS and vary as $\propto E^{-1/2}$ [36].

Band structures of NWs by more accurate calculations of tight-binding method (TB) [37-39] and density functional theory (DFT) [40, 41] have been reported. Figures 1.11 and 1.12 show the band gap and effective mass of the lowest/highest conduction/valence subband, respectively, as a function of the NW's cross-sectional size, where the band gap calculated by EMA following the first paragraph is also plotted. The reported values vary widely, presumably because calculation accuracy, surface termination, cross-sectional shape, and definition of cross-sectional size are different among these reports. The band gap increases with decrease of the size and changes with NW direction as $E_{g,<100>} > E_{g,<111>} > E_{g,<110>}$. The EMA overestimates the change of the band gap ($E_{g,NW}-E_{g,bulk}$). The effective mass, for the most part, increases with the size decrease. The <110> NW has relatively light effective mass for both electrons and holes, which is favorable for carrier transport.

1.3 Device applications of Si nanowires

1.3.1 Si nanowire MOSFETs for advanced CMOS

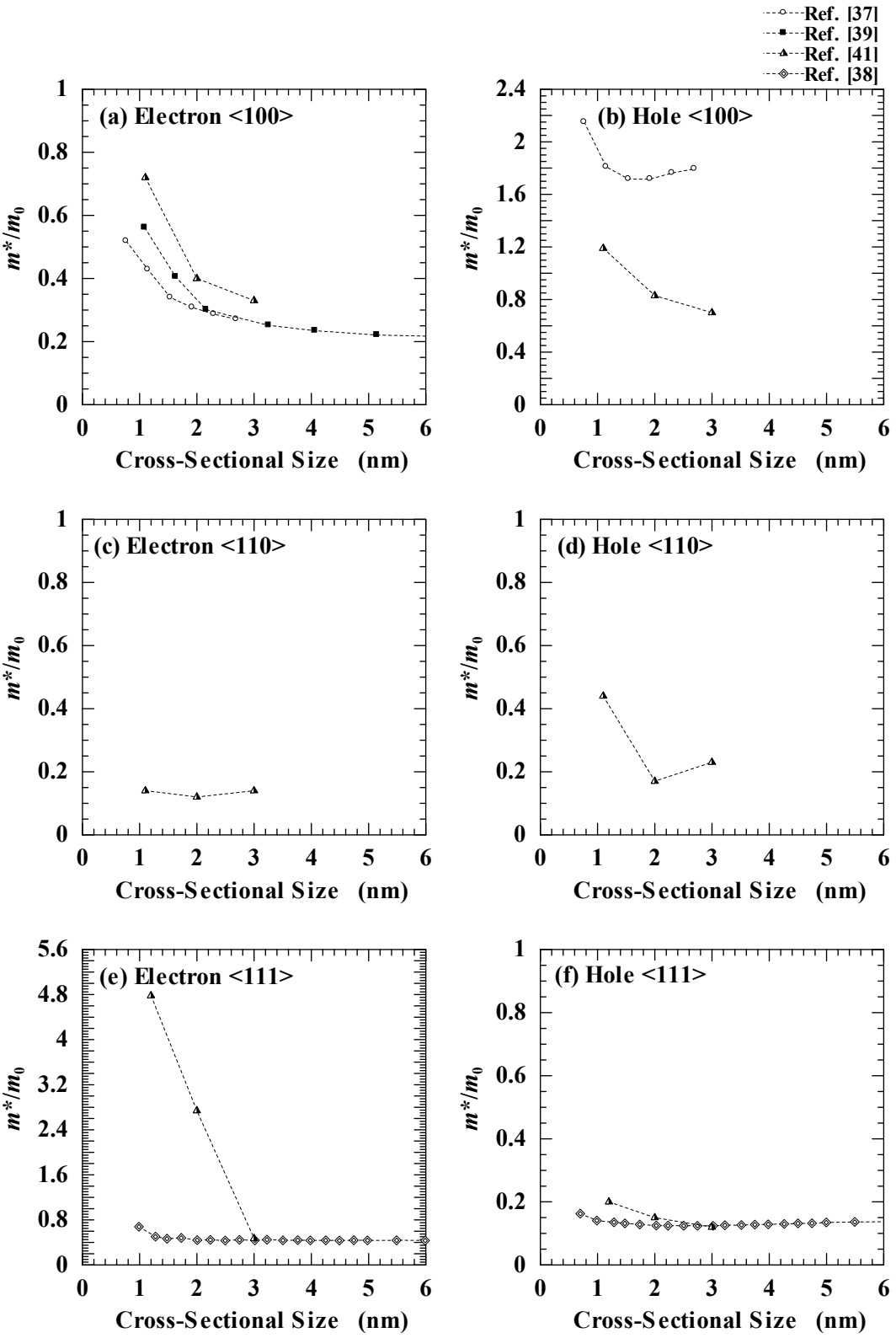

Fig. 1.12 Calculated effective mass for electrons and holes in Si NWs with different directions as a function of the NW's cross-sectional size [37-39, 41].

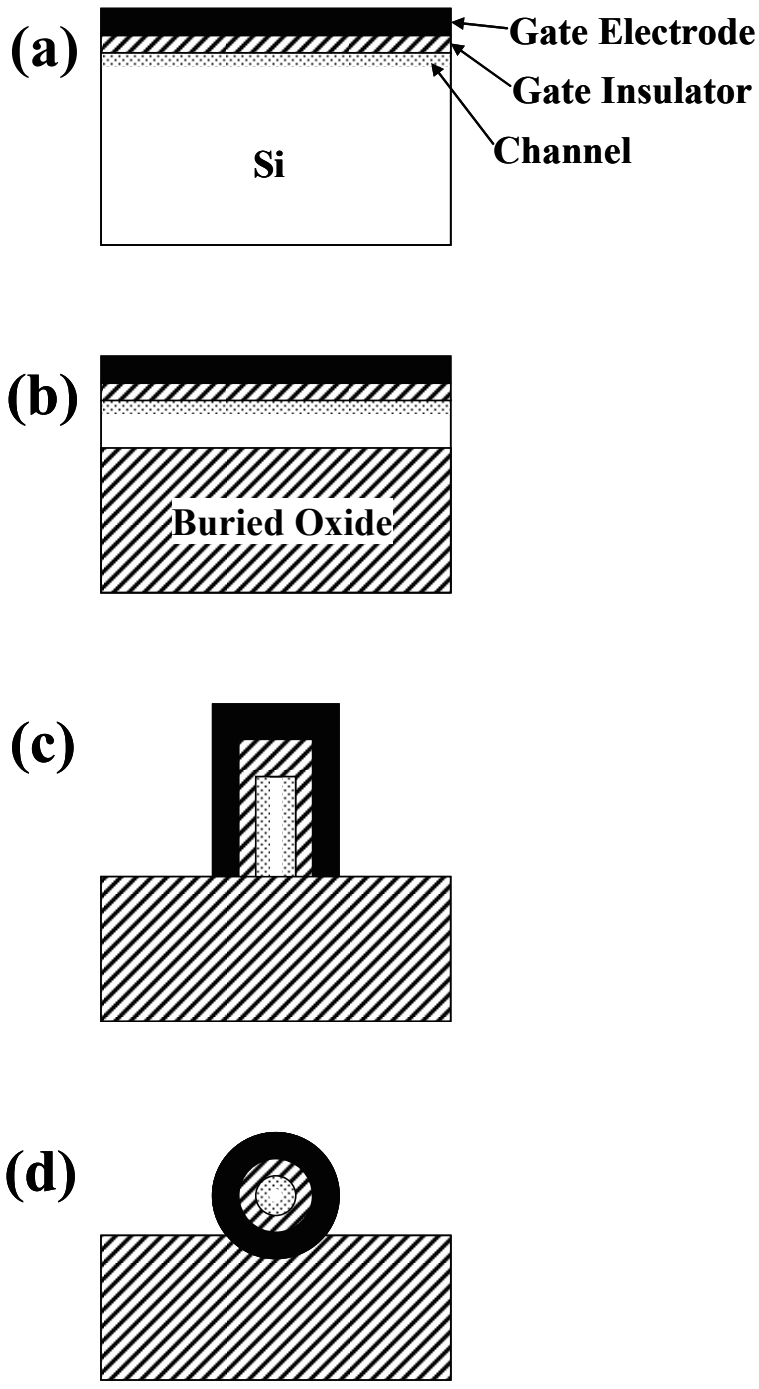

Fig. 1.13 (a) conventional structure of a planar-gate MOSFET using bulk Si, and the advanced structures of (b) SOI MOSFET and (c, d) surrounding-gate MOSFETs. The current direction is perpendicular to the paper.

Si MOSFETs have made progress with miniaturization according to the scaling law originally proposed by Dennard [42]. According to the scaling law, with decrease of the dimensions by the factor $1/a$, the speed increases by a and the power dissipation decreases by $1/a^2$ while maintaining the power density constant. To attain the scaling merits fully, all the dimensions need to be scaled properly, but some factors have become difficult to shrink further. Lowering of the threshold voltage and supply voltage is restricted by the subthreshold slope, which does not scale [43]. Thinning the gate oxide is restricted by tunneling current through the gate oxide [44]. Shallowing of the source/drain junction is restricted by ion implantation and annealing technology, as well as series resistance [45]. Improper scaling with these restrictions increases short-channel effects (SCEs) to an unacceptable level. The MOSFETs with a gate length of 5~16 nm show severe SCEs, which can be grasped by the large subthreshold slope of over 100 mV/dec. [46-49].

To overcome these difficulties, new structures such as surrounding-gate-structures have been proposed. The structures can control the SCEs effectively because the channel potential is well controlled by the gate potential and screened from the drain potential [50-52]. Figure 1.13 shows (a) the conventional structure of a planar-gate MOSFET using bulk Si, and the advanced structures of (b) an SOI MOSFET using Si-on-insulator (SOI) and (c, d) surrounding-gate MOSFETs using SOI. The structure (b) has the feature that the channel is fabricated in a thin Si layer on top of a buried oxide layer and is expected to be employed in the near future [53]. The structures (c, d), of which the channel is sandwiched or surrounded by the gate, have superior SCE immunity. However, the structures (c, d) are difficult to form, and various structural types with different process and SCE immunity are under consideration.

For the new structures, the problem of shallowing the source/drain junction and depletion depth is converted to reducing the thickness or cross-sectional area of the Si channel region. In other words, the more the Si channel is downsized, the more the SCEs are reduced. Therefore, to reduce the cross-sectional area of the channel with surrounding-gate MOSFETs is one of the choices for improving the performance besides the further miniaturization of the gate and channel length. Since the channel length of state-of-the-art MOSFETs is below 50 nm, the surrounding-gate MOSFETs with the same channel length must have a sufficiently smaller cross-sectional diameter than the length. The diameter would be smaller than 10 nm, and such devices can be called NW MOSFETs.

Surface effects such as QCE become conspicuous for such small NWs and must be clarified to put the NW MOSFETs to practical use, besides establishing the fabrication technologies. Some QCEs have been reported so far. Increase of the CBM increases the threshold voltage of n-channel MOSFETs, and likewise for p-channel MOSFETs [54, 55]. Drain current oscillates with sweep of the gate voltage at lower temperature and lower drain voltage, which would originate from oscillatory one-dimensional DOS [56-58] or Coulomb blockade phenomenon [59]. Volume inversion increases the mobility because of reduced interface scattering [60, 61]. The volume inversion is a phenomenon where induced-carriers stay more around the center of the wire than the Si/SiO_2 interface when carriers induced at an interface nearly overlap with carriers at the opposite

interface. Volume inversion would become conspicuous when the NW cross-sectional size becomes as small as the size of the inversion layer. On the other hand, mobility degradation by carrier scattering induced by interface fluctuation was reported for thin film MOSFETs with a thickness below 4 nm [62], which is apparently inconsistent with the volume inversion effect. The change of the effective mass mentioned in Section 1.2.2 is also an important factor affecting the mobility. Which factor dominantly affects the mobility must depend on conditions such as NW shape and size, temperature, and electric field. Therefore, answering this question is very difficult and requires much more research.

1.3.2 Light-emitting-devices of Si nanowires

Electrical interconnections do not shrink with the shrinking of transistors and would restrict the LSI performance. Optical interconnections are expected to replace electrical interconnections to overcome delay, power, and bandwidth problems [63, 64]. To realize optical interconnections, such devices as light emitters, waveguides, and detectors are needed. Among the devices, the realization of light emitters compatible with LSI processing is far more difficult because the light-emitting efficiency of bulk Si is extremely low because of the indirect-bandgap nature. However, the introduction of other materials, which are usually incompatible with LSI, results in high-cost processing. Therefore, Si-based light emitters are in strong demand to combine photonics with Si-based electronics [65-67].

Si nanostructures such as dots [68, 69], porous Si [70-72], nanowires [73], and nanofilms [74] are promising light-emitter candidates [75, 76]. The QCE in nanostructures increases the bandgap energy and the uncertainty of the crystal momentum, by which no-phonon radiative recombination may increase and with which improvement in light-emitting efficiency is expected [77-80]. QCE has been observed by the shift of the emission peak to the higher energy side. However, the actual external-quantum-efficiency of the nanostructures ($\leq 10^{-2}$ [72]) remains as low as the bulk's efficiency [81, 82]. Besides QCE, the interface/surface states of the nanostructures play a crucial role in the recombination process. To further increase the efficiency, the structure and the interface of the nanostructures must be optimized.

1.4 Purpose and outline

In this thesis, first, a fabrication process of Si NWs with a cross-sectional size below 10 nm is established, and then carrier transport characteristics in Si NW MOSFETs are studied. The size dependence of the mobility is scrutinized, from which the electronic states and the carrier scattering mechanism peculiar to Si NWs are inferred. Moreover, to clarify the origin of the current oscillation

with gate-voltage sweep in NW MOSFETs, The author proposes an analytical transport model, taking account of acoustic phonon scattering in Si NWs. In addition to the transport characteristics, the optical properties of Si NWs are also studied aiming at light-emitting diodes. The light-emitting properties of Si NWs are estimated by calculating the absorption coefficients for band-to-band transition. Si-NW pn diodes are fabricated, and their light-emitting properties are investigated.

In Chapter 2, a fabrication process of Si NWs with a cross-sectional size below 10 nm by a top-down approach using electron beam lithography and sacrificial oxidation is established. The NW shapes are investigated by cross-sectional and top views using TEM and SEM.

In Chapter 3, the mobility of Si NWs with a cross-sectional size of several tens of nm to 4 nm is investigated. QCE in Si NWs is confirmed by the threshold-voltage shift resulting from the band-edge shift. Confinement conditions of carriers is inferred by evaluating the change of the electron and hole mobility ratio with decreasing the size. The scattering mechanism in Si NWs is inferred from the temperature dependence of the mobility.

In Chapter 4, a transport model is proposed that reproduces the drain-current oscillation. The model assumes one-dimensional electronic states, and elastic and isotropic phonon scattering. The gate-voltage dependence of the carrier mobility and the concentration in Si NW MOSFETs is calculated by the model. The calculated results are compared with the experimental results, and the origin of the oscillation is discussed based on the model.

In Chapter 5, the electronic states and the optical absorption coefficient of the Si NWs are calculated using DFT, and their light-emitting potential is estimated from the band-edge absorption coefficient. The dependencies of the absorption coefficient for <100> and <111> Si NWs on the cross-sectional size and polarization direction are investigated. A forbidden transition is discussed based on the group theory.

In Chapter 6, Si-NW pn diodes are fabricated and the dependence of the electroluminescence on NW size is investigated.

In Chapter 7, conclusions and suggestions for future work are presented.

References

[1] *World Semiconductor Trade Statistics* (World Semiconductor Trade Statistics Inc., http://www.wsts.org/).

[2] G. E. Moore, Proc. IEEE **86**, 82 (1998).

[3] D. Kahng and M. M. Atalla, *IRE Device Research Conference*, Pittsburgh (1960).

[4] T. Hahn ed., *International Tables for Crystallography, 5th ed.* (Kluwer Academic Publishers, Dordrecht; Boston, 2002).

[5] M. E. Straumanis, P. Borgeaud, and W. J. James, J. Appl. Phys. **32**, 1382 (1961).

[6] K. G. Lyon, G. L. Salinger, C. A. Swenson, and G. K. White, J. Appl. Phys. **48**, 865 (1977).

[7] Y. Okada and Y. Tokumaru, J. Appl. Phys. **56**, 314 (1984).

[8] S. Wei and M. Y. Chou, Phys. Rev. B **50**, 2221 (1994).

[9] V. Alex, S. Finkbeiner, and J. Weber, J. Appl. Phys. **79**, 6943 (1996).

[10] J. R. Chelikowsky and M. L. Cohen, Phys. Rev. B **14**, 556 (1976).

[11] M. Lundstrom, *Fundamentals of Carrier Transport, 2nd ed.* (Cambridge University Press, Cambridge, 2000).

[12] G. Dresselhaus, A. F. Kip, and C. Kittel, Phys. Rev. **98**, 368 (1955).

[13] L. Reggiani Ed., *Hot-Electron Transport in Semiconductors* (Springer-Verlag, Berlin; New York, 1985).

[14] S. M. Sze and K. K. Ng, *Physics of Semiconductor Devices, 3rd ed*. (Wiley-Interscience, Hoboken, 2007).

[15] S. Zwerdling, K. J. Button, B. Lax, and L. M. Roth, Phys. Rev. Lett. **4**, 173 (1960).

[16] W. R. Thurber, R. L. Mattis, and Y. M. Liu, J. Electrochem. Soc. **127**, 2291 (1980).

[17] G. Masetti, M. Severi, and S. Solmi, IEEE Trans. Electron Devices **ED-30**, 764 (1983).

[18] C. Canali, C. Jacoboni, F. Nava, G. Ottaviani, and A. Alberigi-Quaranta, Phys. Rev. B **12**, 2265 (1975).

[19] G. Ottaviani, L. Reggiani, C. Canali, F. Nava, and A. Alberigi-Quaranta, Phys. Rev. B **12**, 3318 (1975).

[20] R. A. Logan and A. J. Peters, J. Appl. Phys. **31**, 122 (1960).

[21] C. Jacoboni, C. Canali, G. Otiaviani, and A. Alberigi-Quaranta, Solid-State Electron. **20**, 77 (1977).

[22] G. Baccarani, and M. R. Wordeman, IEEE Trans. Electron Devices **ED-30**, 1295 (1983).

[23] S. Takagi, A. Toriumi, M. Iwase, and H. Tango, IEEE Trans. Electron Devices **41**, 2357 (1994).

[24] S. Takagi, A. Toriumi, M. Iwase, and H. Tango, IEEE Trans. Electron Devices **41**, 2363 (1994).

[25] K. Lee, J. Choi, S. Sim, and C. Kim, IEEE Trans. Electron Devices **38**, 1905 (1991).

[26] A. G. Sabnis and J. T. Clemens, *Int. Electron Devices Meeting* (1979) p18.

[27] S. C. Sun and J. D. Plummer, IEEE Trans. Electron Devices **ED-27**, 1497 (1980).

[28] G. G. Macfarlane and V. Roberts, Phys. Rev. **98**, 1865 (1955).

[29] T. Nishino, M. Takeda, and Y. Hamakawa, Solid State Communications **14**, 627 (1974).

[30] K. L. Shaklee and R. E. Nahory, Phys. Rev. Lett. **24**, 942 (1970).

[31] D. E. Aspnes and J. B. Theeten, J. Electrochem. Soc. **127**, 1359 (1980).

[32] R. Hulthén, Physica Scripta **12**, 342 (1975).

[33] E. D. Palik ed., *Handbook of Optical Constants of Solids* (Academic Press, Boston; Tokyo, 1985).

[34] H. C. Casey Jr., D. D. Sell, and K. W. Wecht, J. Appl. Phys. **46**, 250 (1975).

[35] J. B. Theeten, D. E. Aspnes, and R. P. H. Chang, J. Appl. Phys. **49**, 6097 (1978).

[36] M. S. Lungstrom and J. Guo, *Nanoscale Transistors: Device Physics, Modeling and Simulation*

(Springer, New York, 2005).

[37] Y. Zheng, C. Rivas, R. Lake, K. Alam, T. B. Boykin, and G. Klimeck, IEEE Trans. Electron devices **52**, 1097 (2005).

[38] Y. M. Niquet, A. Lherbier, N. H. Quang, M. V. Fernández-Serra, X. Blase, and C. Delerue, Phys. Rev. B **73**, 165319 (2006).

[39] K. Nehari, N. Cavassilas, J. L. Autran, M. Bescond, D. Munteanu, M. Lannoo, Solid-state Electron. **50**, 716 (2006).

[40] X. Zhao, C. M. Wei, L. Yang, and M.Y. Chou, Phys. Rev. Lett. **92**, 236805 (2004).

[41] T. Vo, A. J. Williamson, and G. Galli, Phys. Rev. B **74**, 045116 (2006).

[42] R. H. Dennard, F. H. Gaensslen, H. Yu, V. L. Rideout, E. Bassous, and A. R. Leblanc, IEEE J. Solid State Circuits **SC-9**, 256 (1974).

[43] S. Oda and D. K. Ferry ed., *Silicon Nanoelectronics* (Taylor & Francis Group, Boca Raton, 2006).

[44] S. Lo, D. A. Buchanan, Y. Taur, and W. Wang, IEEE Electron Device Lett. **18**, 209 (1997).

[45] B. Yu, Y. Wang, H. Wang, Q. Xiang, C. Riccobene, S. Talwar, M. Lin, *Tech. Dig. of 1999 Int. Electron Devices Meeting* (1999) p. 509.

[46] A. Hokazono, K. Ohuchi, M. Takayanagi, Y. Watanabe, S. Magoshi, Y. Kato, T. Shimizu, S. Mori, H. Oguma, T. Sasaki *et al.*, *Tech. Dig. of 2002 Int. Electron Devices Meeting* (2002) p. 639.

[47] B. Yu, H. Wang, A. Joshi, Q. Xiang, E. Ibok, and M. Lin, *Tech. Dig. of 2001 Int. Electron Devices Meeting* (2001) p. 937.

[48] F. Bouef, T. Skotnicki, S. Monfray, C. Julien, D. Dutartre, J. Martins, P. Mazoyer, R. Palla, B. Tavel, P. Ribot *et al.*, *Tech. Dig. of 2001 Int. Electron Devices Meeting* (2001) p. 637.

[49] H. Wakabayashi, S. Yamagami, N. Ikezawa, A. Ogura, M. Narihiro, K. Arai, Y. Ochiai, K. Takeuchi, T. Yamamoto, and T. Mogami, *Tech. Dig. of 2003 Int. Electron Devices Meeting* (2003) p. 989.

[50] R. Yan, A. Ourmazd, and K. F. Lee, IEEE Trans. Electron Devices **39**, 1704 (1992).

[51] K. Suzuki, T. Tanaka, Y. Tosaka, H. Horie, and Y. Arimoto, IEEE Trans. Electron Devices **40**, 2326 (1993).

[52] C. P. Auth, and J. D. Plummer, IEEE Electron Device Lett. **18**, 74 (1997).

[53] *International Technology Roadmap for Semiconductors 2009 Edition* (International Technology Roadmap for Semiconductors, http://www.itrs.net/).

[54] K. Uchida, J. Koga, R. Ohba, T. Numata, and S. Takagi, *Tech. Dig. of 2001 Int. Electron Devices Meeting* (2001) p. 633.

[55] H. Majima, H. Ishikuro, and T. Hiramoto, IEEE Electron Device Lett. **21**, 396 (2000).

[56] S. C. Rustagi, N. Singh, Y. F. Lim, G. Zhang, S. Wang, G. Q. Lo, N. Balasubramanian, and D. Kwong, IEEE Electron Device Lett. **28**, 909 (2007).

[57] J. Colinge, A. J. Quinn, L. Floyd, G. Redmond, J. C. Alderman, W. Xiong, C. R. Cleavelin, T. Schulz, K. Schruefer, G. Knoblinger, and P. Patruno, IEEE Electron Device Lett. **27**, 120 (2006).

[58] M. Je, S. Han, I. Kim, H. Shin, Solid-state Electron. **44**, 2207 (2000).
[59] M. Kobayashi and T. Hiramoto, J. Appl. Phys. **103**, 053709 (2008).
[60] T. Ouisse, J. Appl. Phys. **76**, 5989 (1994).
[61] J. Colinge, Solid-State Electron. **51**, 1153 (2007).
[62] K. Uchida and S. Takagi, Appl. Phys. Lett. **82**, 2916 (2003).
[63] J. W. Goodman, F. I. Leonberger, S.-Y. Kung, and R. A. Athale, Proc. IEEE **72**, 850 (1984).
[64] D. A. B. Miller, Proc. IEEE **88**, 728 (2000).
[65] R. A. Soref, Proc. IEEE **81**, 1687 (1993).
[66] P. Ball, Nature **409** 974 (2001).
[67] B. Jalali and S. Fathpour, J. Lightwave Technol. **24**, 4600 (2006).
[68] L. Pavesi, L. D. Negro, C. Mazzoleni, G. Franzò, and F. Priolo, Nature **408**, 440 (2000).
[69] N. M. Park, T. S. Kim, and S. J. Parka, Appl. Phys. Lett. **78**, 2575 (2001).
[70] N. Koshida and H. Koyama, Appl. Phys. Lett. **60**, 347 (1992).
[71] P. Steiner, F. Kozlowski, and W. Lang, Appl. Phys. Lett. **62**, 2700 (1993).
[72] B. Gelloz and N. Koshida, J. Appl. Phys. **88**, 4319 (2000).
[73] A. G. Nassiopoulos, S. Grigoropoulos, and D. Papadimitriou, Appl. Phys. Lett. **69**, 2267 (1996).
[74] S. Saito, D. Hisamoto, H. Shimizu, H. Hamamura, R. Tsuchiya, Y. Matsui, T. Mine, T. Arai, N. Sugii, K. Torii *et al.*, Jpn. J. Appl. Phys. **45**, L679 (2006).
[75] D. J. Lockwood, J. Mater. Sci.: Mater. Electron. **20**, S235 (2009).
[76] N. Daldosso and L. Pavesi, Laser & Photon. Rev. **3**, 508 (2009).
[77] F. Buda and J. Kohanoff, Prog. Quant. Electr. **18**, 201 (1994).
[78] D. Kovalev, H. Heckler, G. Polisski, and F. Koch, Phys. Stat. Sol. (b) **215**, 871 (1999).
[79] M. S. Hybertsen, Phys. Rev. Lett. **72**, 1514 (1994).
[80] C. Delerue, G. Allan, M. Lannoo, Phys. Rev. B **48**, 11024 (1993).
[81] W. L. Ng, M. A. Lourenço, R. M. Gwilliam, S. Ledain, G. Shao, and K. P. Homewood, Nature **410**, 192 (2001).
[82] M. A. Green, J. Zhao, A. Wang, P. J. Reece, and M. Gal, Nature **412**, 805 (2001).

Chapter 2

Fabrication of Si nanowires by top-down approach

2.1 Introduction

The various fabrication methods of Si nanowires (NWs) reported so far can be categorized into bottom-up and top-down approaches. In the bottom-up approach, Si NWs are synthesized, for example, using a vapor-liquid-solid (VLS) technique [1, 2]. Although the bottom-up approach is a low-cost method, an assembly technique must be developed for device applications [3]. The top-down approach, which is based on lithography and etching, generally utilizes an SOI as a material and electron beam (EB) lithography, which results in high-cost manufacturing. In the direct-write EB lithography, low throughput could also be a problem, but throughput may be improved in the future [4]. Circular NWs with a 5- to 7-nm diameter were fabricated utilizing silicon-on-insulator (SOI), EB lithography, and stress-limited oxidation at 875˚C [5]. A circular NW with a 4-nm diameter was fabricated by a process in which twin NWs are formed at the top and bottom of an Si-fin by stress-limited oxidation, and then the top NW is dry etched [6]. A circular NW with a 5-nm diameter was also fabricated from bulk Si [7].

Additional treatments are important to reduce fluctuation of NWs and form straight and uniform NWs. For example, a smooth surface is formed by wet etching in an alkaline solution such as a tetramethylammonium hydroxide (TMAH) solution [8] and thermal etching in H_2 atmosphere [9]. However, these treatments limit the surface to the crystal face. On the other hand, sacrificial oxidation smoothes the surface and maintains the original shape.

In this study, a top-down approach with SOI, EB lithography, and sacrificial oxidation is adopted. By this approach, the NW size and direction can be easily controlled in a substrate.

2.2 Fabrication procedure

The starting material was SOI with a top Si of a 110-nm-thick (001)-oriented p-type film with a resistivity of 5~50 Ω·cm and 200-nm-thick buried-SiO_2 film, manufactured by Shin-Etsu Chemical Co., Ltd.

The top Si was thinned by sacrificial oxidation (1st oxidation) at 1,150˚C in dry O_2, by which a 153-nm-thick SiO_2 was formed, and by removal of the SiO_2. Details of the oxidation conditions are shown in Fig. 2.1(a). To passivate the Si surface, a thin SiO_2 was formed by oxidation (2nd oxidation) at 800˚C (Fig. 2.1(b)). The thickness of the passivation-SiO_2/Si/buried-SiO_2 was determined as 3.6/36.5/200.9 nm by spectroscopic ellipsometry.

NW shapes were patterned by EB lithography. A resist of ZEP520A-7 by the Zeon Co., diluted by anisol of ZEP-A by Zeon Co., was used, where the mass ratio was ZEP520A-7: ZEP-A = 1: 1. The resist was coated at 1,800 rpm for 1 min on a nearly square 1 cm × 1 cm substrate and baked at 160˚C for 3 min. Patterning was performed directly on the resist by EB under the following conditions: acceleration voltage, beam current, dose, and beam diameter were 100 kV, 100 pA, 170 μC/cm^2, and 2 nm, respectively. The patterning length of the NWs was 100 nm, and the width was changed from 56 to 18 nm by a 2-nm step. The resist was developed at 23˚C for 2 min in an n-amyl acetate of ZED-N50 by the Zeon Co., rinsed in isopropyl alcohol (IPA) for 40 sec, and blow-dried by N_2.

Si NWs were formed by reactive ion etching (RIE) using the resist as a mask. RIE was performed for 90 sec at 16 W (cathode diameter: 7.5 cm) in CF_4 gas with 16 sccm and 5 Pa. The resist was removed in SPM (H_2SO_4/H_2O_2/H_2O) at 80˚C for about 4 hours. The step heights at pattern edges before RIE, after RIE, and after resist removal were 116, 92, and 32 nm, respectively. That is, the thickness of the resist after developing was 116 nm, and the etching quantity of the resist and the Si (including passivation SiO_2) was 56 and 32 nm, respectively; the etching rates of the resist and the Si were 37 nm/min and 21 nm/min, respectively.

Sacrificial oxidation (3rd oxidation) to remove the RIE damage and reduce the NW size was carried out at 1,000˚C (Fig. 2.1(c)). The SiO_2 was removed by dipping in BHF (NH_4F/HF/H_2O). SiO_2, which is used as a gate insulator for MOSFETs, was formed on the NW surface by oxidation (4th oxidation) at 1,000˚C (Fig. 2.1(d)). The SiO_2/Si/SiO_2 thickness was changed from 3.6/36.5/200.9 to 18.8/30.3/200.6 nm after the 3rd oxidation and to 23.1/18.9/201.0 nm after the 4th oxidation, which was measured for the large area where RIE was not performed. Therefore, about 18-nm-thick Si from the NW surface was consumed by the 3rd and 4th oxidations. Note that since the side faces of the NW are not {001} and have RIE damage, the oxide thickness on the side faces does not exactly equal the thickness described above.

The shape of NWs fabricated by the procedure described in this section characterized in the next section.

2.3 Characterization of nanowire shape

2.3.1 Top-view observation by SEM

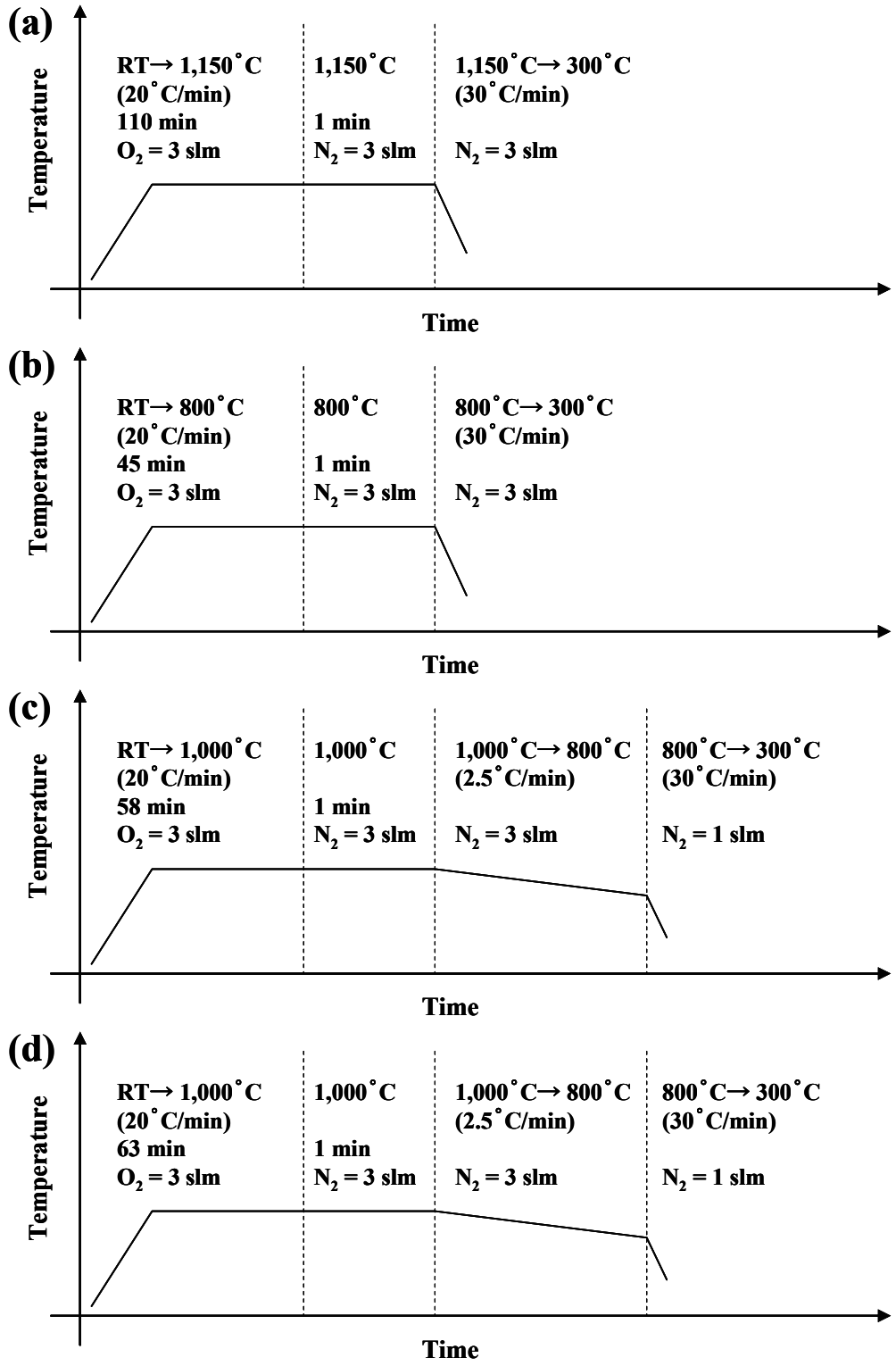

Fig. 2.1 Procedures of (a) 1st, (b) 2nd, (c) 3rh, and (d) 4th oxidation. The cooling rate of 30˚C/min is a set point and the actual rate was 7~10˚C/min.

Figure 2.2 shows the top-view images of NWs just after the resist removal following RIE measured by SEM, and Fig. 2.3 shows relation between the NW width measured from the SEM image and the patterning width (W_P) defined as a set width in EB lithography. Large areas connected at both sides of Si NWs are necessary to easily connect Si NWs and electrodes. At this stage, NWs should be as narrow and straight as possible. The thickness and width of the resist on the NWs shrink by the proximity effect of the EB and RIE. As a result, the NW width measured from the SEM image was narrower than the W_P (Fig. 2.3). The degree of reduction was larger for narrower NWs, and the Si NWs with a narrow W_P below about 18 nm were etched away because of the resist disappearance during RIE; optimization of the residual resist is important to form narrow NWs.

The EB dose, the patterning length and the width of the NWs, and the selectivity ratio and the time of the RIE were optimized. As a result, NW as narrow as 13 nm was successfully formed with a W_P of 18 nm (Fig 2.2(a)). The conditions described in Section 2.2 are the optimized conditions. The EB dose must be minimized but be enough to completely remove the resist on the exposed area by developing. Although shortening the NW length increases the residual resist on the NWs, the sides of short NWs are not straight anymore because the round corners occupy most of the NW length. Even for the optimized conditions, the round parts occupied 30% of the NW length (Figs. 2.2(a, b)). To reduce the round parts, it may be necessary that the mask covering the NW and the mask covering the areas connected at both sides of the NW are separately formed [10]. The selectivity ratio of RIE must be high, but only a low ratio of 0.57 (= Si/resist) was given. The RIE time must be minimized by thinning the Si film (including passivation SiO_2) within possible limits.

2.3.2 Cross-sectional observation by TEM

Figure 2.4 shows the cross-sectional images of NWs after the 4th oxidation measured by TEM under conditions of a bright field imaging mode and an acceleration voltage of 300 kV. Figure 2.5 shows high-magnification cross-sectional TEM images of the NW shown in Fig. 2.4(b). The topmost of the NWs was covered with an Al polycrystal. The Si-NW direction was [100]. When the diffraction conditions of the electron beam in the Si crystal are well satisfied, the Si image becomes dark. Since the thickness of TEM specimen was about 100 nm and the NW length was 100 nm, an image of the SiO_2/Si-layer structure outside the Si NW (horizontal lines) was superimposed on the NW image for some specimens. The structure of the TEM sample is illustrated in Fig. 2.6. The SiO_2/Si thickness of the outside film was 25/15 nm, which must be identified and approximately agreed with the value of 23.1/18.9 nm measured by spectroscopic ellipsometry (described in Section 2.2). The thickness of TEM specimen was scattered around 100 nm among the specimens because precise control and measurement of the thickness is difficult. The samples without outside-film images are thinner than the NW length of 100 nm.

The NW cross-sectional shape changed with a change of W_P: an ellipse for 18~24 nm, a triangle

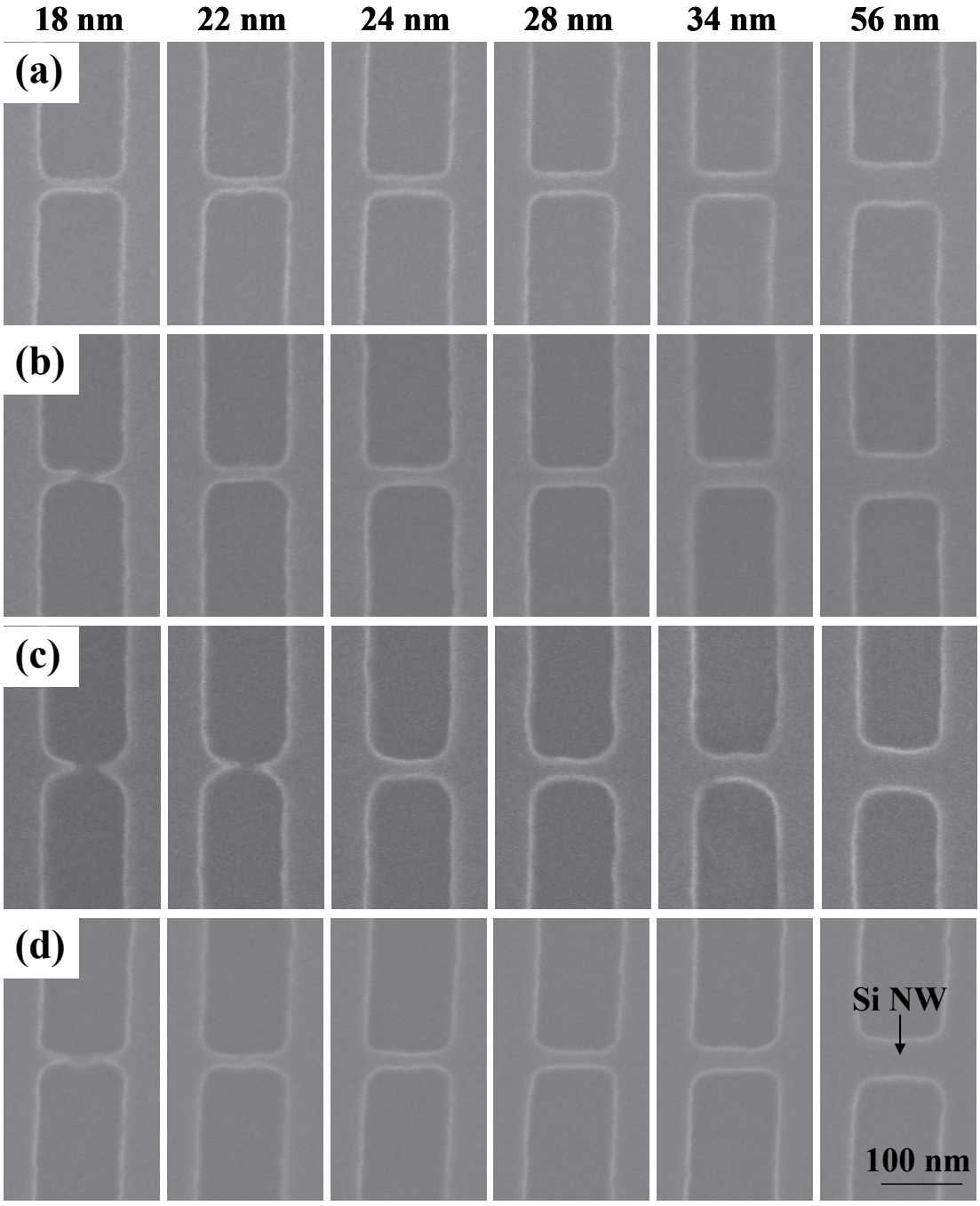

Fig. 2.2 Patterning width (W_P) dependence of top-view SEM images of NWs just after the resist removal following the RIE. Acceleration voltage was 25 kV. W_P is shown at the top. (a-d) are images for different chips. (a, b) and (c,d) are for RIE time of 90 sec and 100 sec, respectively.

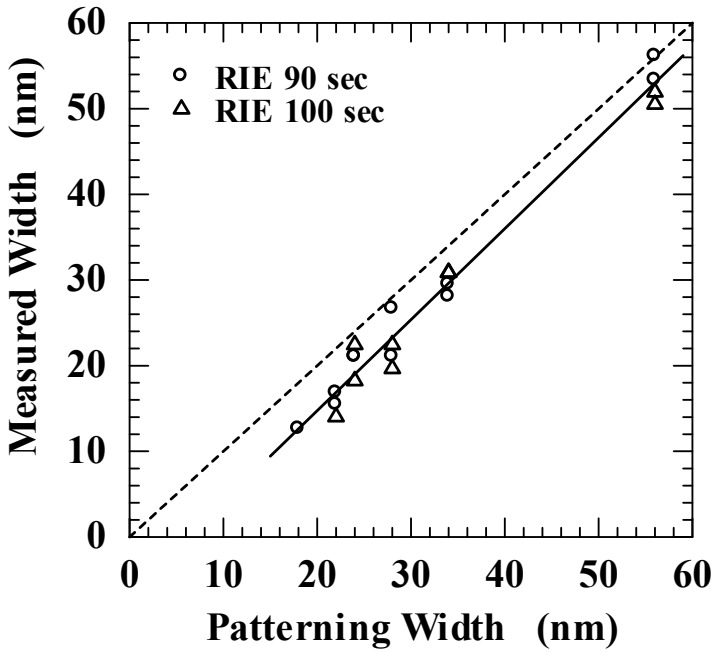

Fig. 2.3 Relation between the NW width measured from the SEM image and the patterning width (W_P). The solid line is a best-fitting line.

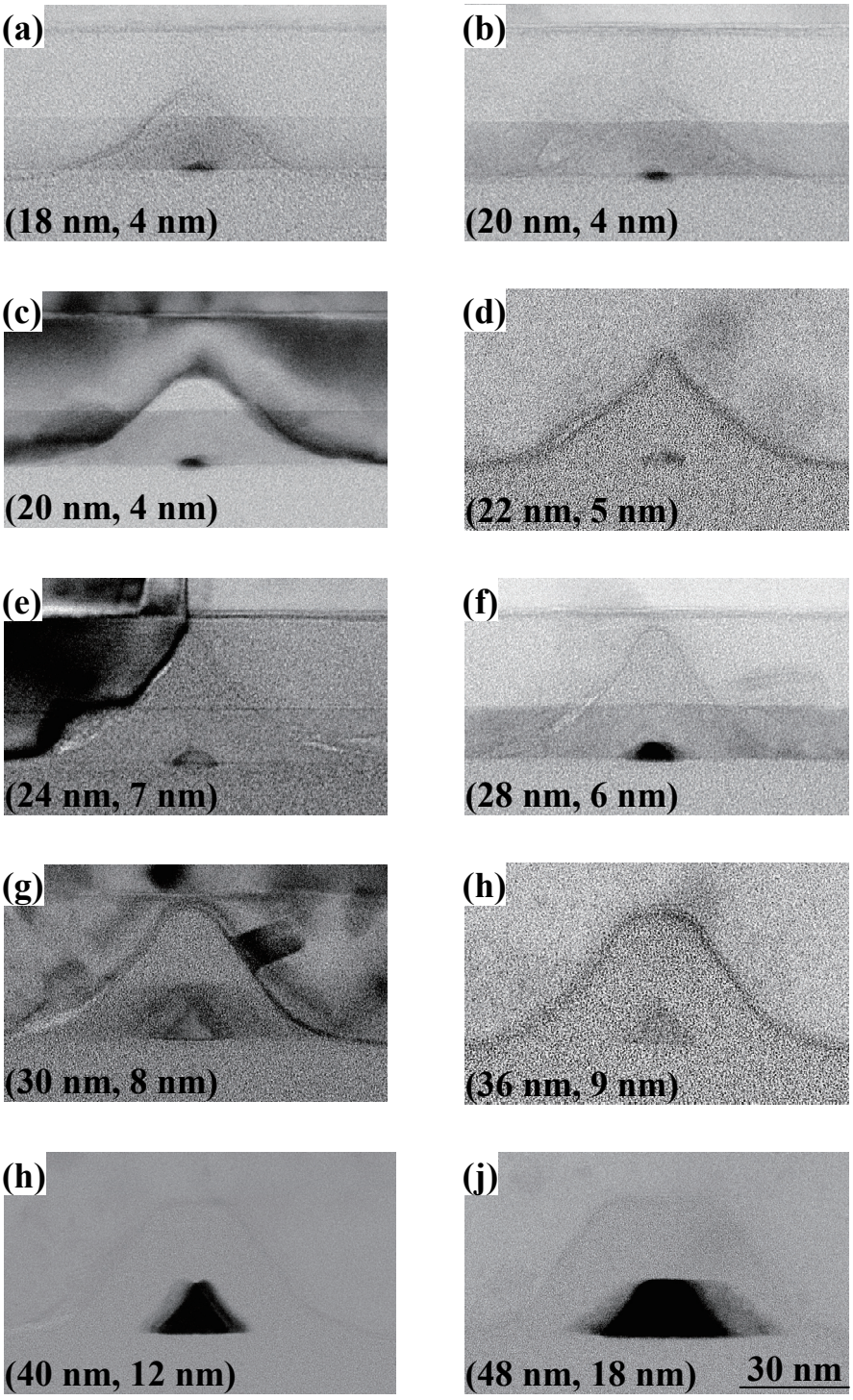

Fig. 2.4 Patterning width (W_P) dependence of cross-sectional TEM images of NWs after the 4th oxidation. The direction of NWs was [100]. The first and second values in the parentheses indicate W_P and cross-sectional size (W), respectively. The two images with a W_P of 20 nm are for different NWs.

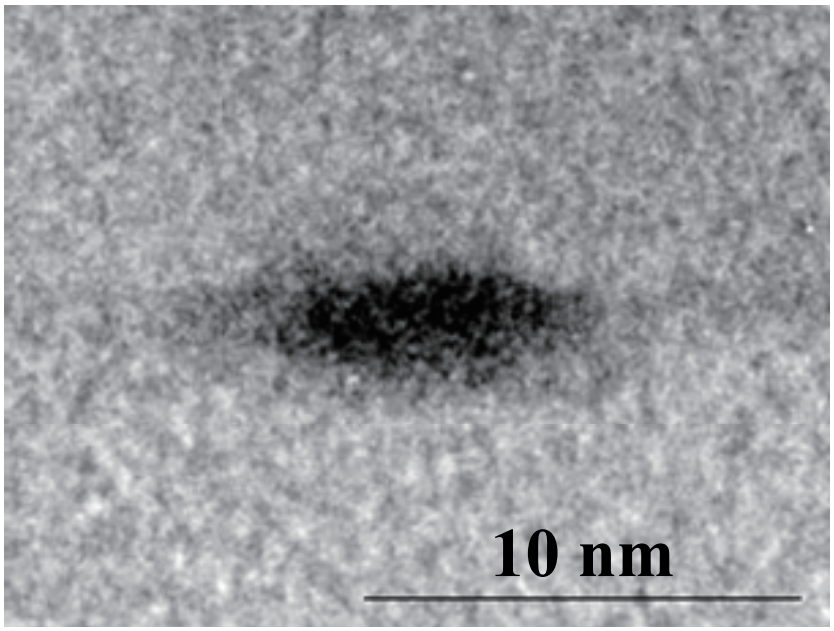

Fig. 2.5 High-magnification cross-sectional TEM images of the NW shown in Fig. 2.4(b).

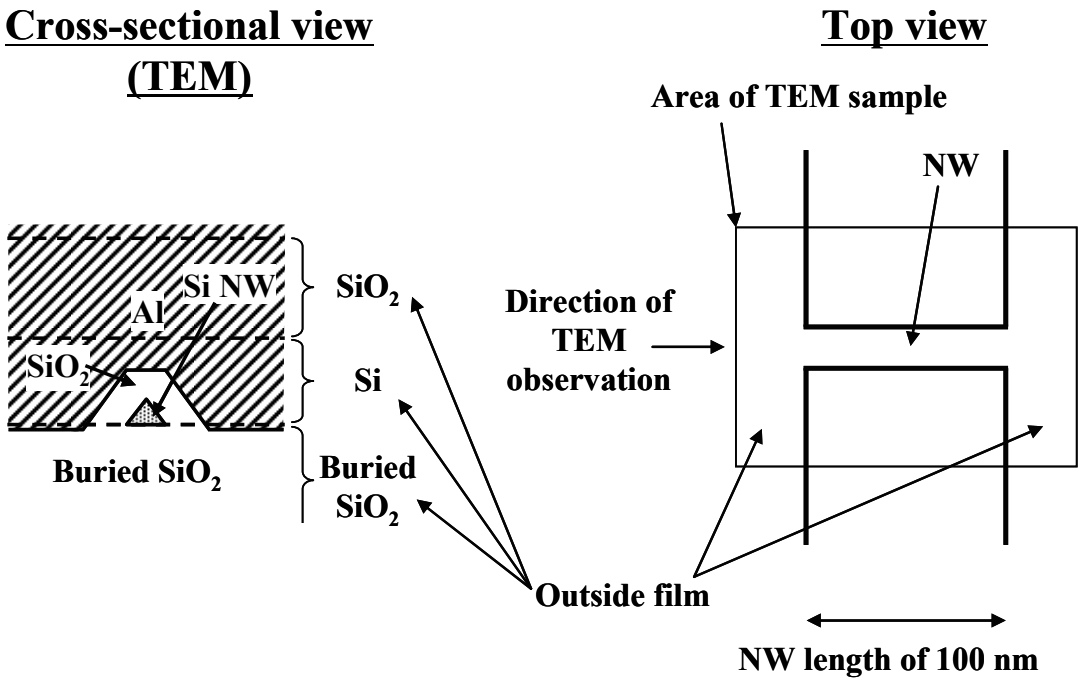

Fig. 2.6 Illustration of the structure of the TEM sample.

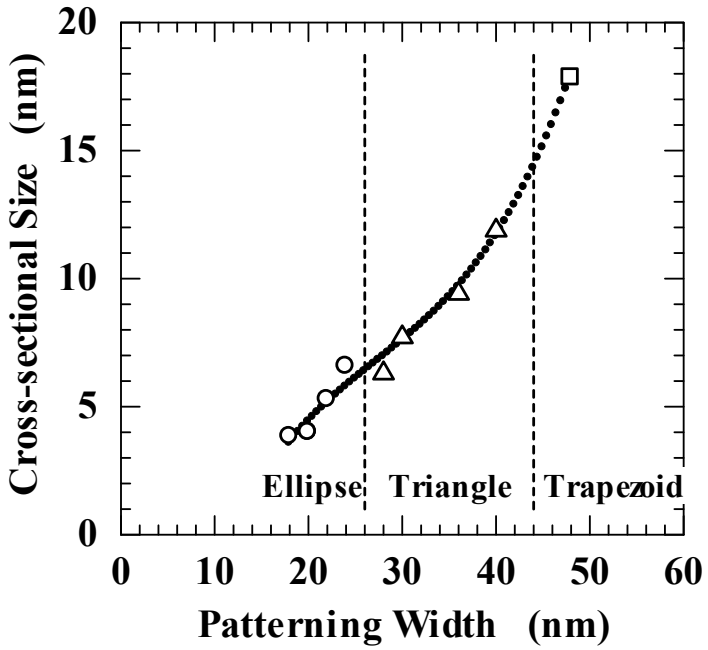

Fig. 2.7 Relation between the NWs' cross-sectional size (square root of area) measured from the TEM image and the patterning width (W_P). The closed symbols show fitting results.

for 28~40 nm, and a trapezoid for 48 nm. The NWs were completely supported by the buried SiO_2. The NW thickness (height) was thinned to a minimum of 2 nm, and the thickness of the outside Si film remained as thick as 15 nm. The cross-sectional size (W) of the NWs is defined as the square root of the cross-sectional area and was plotted as a function of W_P in Fig. 2.7. The W decreased with a decrease in W_P, and formation of an NW with a W as small as 4 nm (height: 2 nm, width: 7 nm) was accomplished by a W_P of 18 nm.

The bottom interface of the Si NWs originates in the interface between the Si and the buried-SiO_2 films of the starting-material SOI and must be unchanged during the fabrication process. Therefore, the bottom interface was clear, smooth, and straight for a W_P wider than about 28 nm. But the bottom interface with a narrow W_P of 20 nm was neither clear nor smooth, and the NW slightly sank in the buried SiO_2. The top or side interface was not also clear because of NW fluctuation, which probably originates in the line-edge roughness or the round parts at the corner characterized by SEM (Section 2.3.1). However, the fluctuation was smaller than 1 nm (Fig. 2.5).

2.4 Discussion

In this sturdy, the author has been aiming for the following: the NW height and width are nearly equivalent, a substrate contains NWs with different W, the W is gradually varied from several tens of nm to well below 10 nm, NWs are supported by buried SiO_2, and the outside Si film remains as thick as several tens of nm.

If NWs with different W are ordinarily formed by changing W_P, the NW height might not be varied by changing the W_P. The NW height is the same as that of the outside Si film, and initial thickness of the Si film must decrease using other substrates to decrease the NW height, as illustrated in Fig. 2.8. To overcome this difficulty, special processing for RIE where the Si film was not completely etched and was left by stopping the etching halfway was adopted. The formation process of the NWs employed in this study is illustrated in Fig. 2.9. By the oxidation following the halfway RIE, the upper part of Si with a narrow W_P was completely oxidized from both sides, and the bottom remained due to no oxidation from the sides. As a result, an Si NW with a thickness thinner than that of the outside Si film is formed at the bottom. On the other hand, for wider W_P, the remaining Si is almost uniformly oxidized from the surface to form trapezoidal NWs. By this method, the W was gradually decreased to 4 nm with decrease in W_P (Fig. 2.7) and maintained similar height and width.

Halfway etching is also important to support NWs on the buried SiO_2. If the etching reaches the buried SiO_2, the buried SiO_2 under the Si NWs is easily etched by the BHF process after the 3rd oxidation. Moreover, control of BHF etching is difficult. Therefore, it is better that a thin Si film remains after the 3rd oxidation, by which the etching of the buried SiO_2 under the Si NWs never

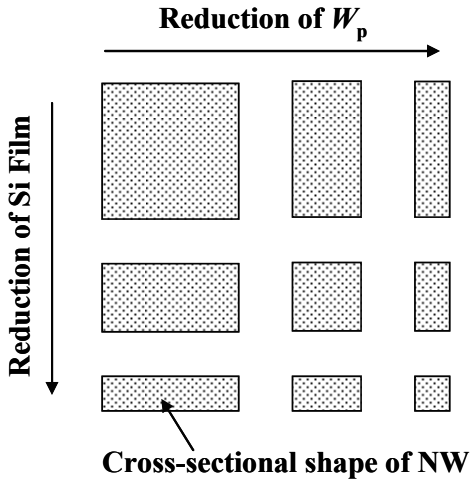

Fig. 2.8 Illustration of dependence of NW shape on patterning width (W_P) and Si-film thickness for conventional fabrication.

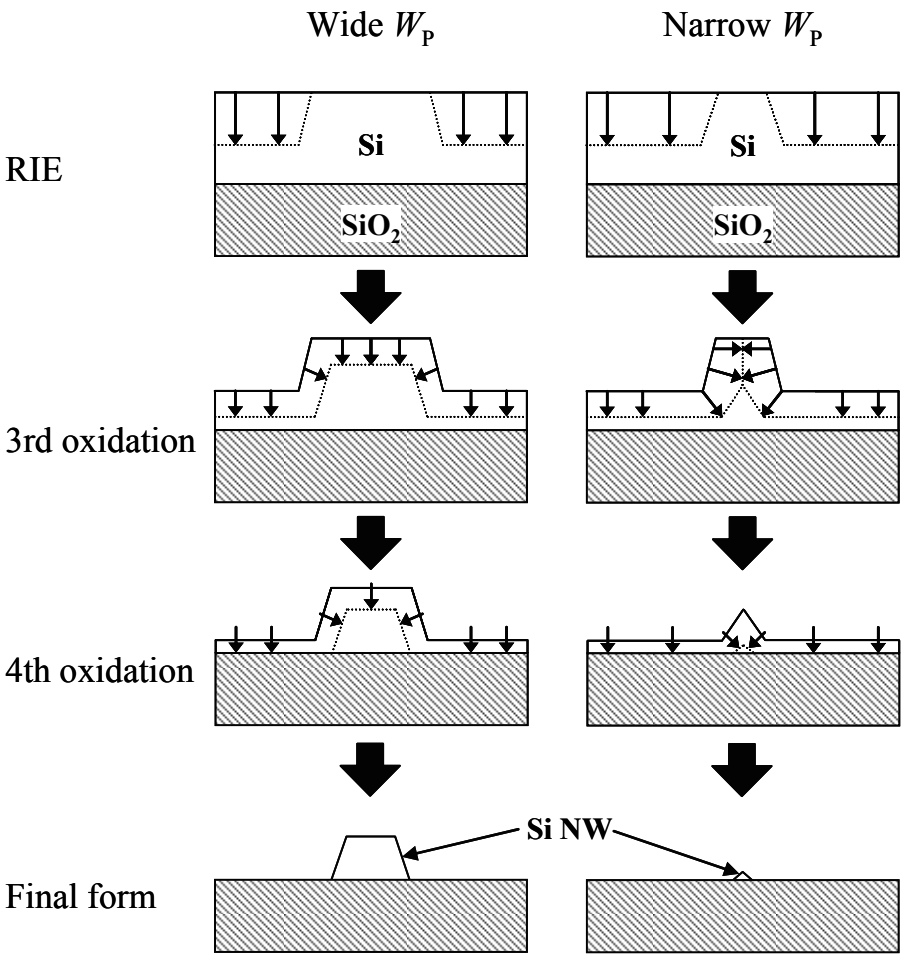

Fig. 2.9 Illustration of formation process of NWs employed in this study. The figures are cross-sectional view of Si NWs, where SiO_2 covering Si NWs is omitted.

occurs. For the process described in Section 2.2, the residual Si film was estimated to be 8-nm thick after RIE, and the 3rd oxidation consumed at least 6-nm-thick Si, and then about 2-nm-thick Si film successfully remained before the BHF process. The TEM images also indicate no under-etching.

2.5 Summary

In this chapter, a fabrication method of Si NWs, the NW shape characterized by SEM and TEM, and the formation mechanism were described.

Si NWs were formed by the top-down method using EB lithography and sacrificial oxidation. By optimizing the EB dose, the patterning length and the width of NWs, and the selectivity ratio and the time of RIE, formation of NWs as narrow as 13 nm was accomplished by EB lithography. After downsizing by sacrificial oxidation, an ellipsoid NW with a minimum cross-sectional size (square root of the area) of 4 nm (height: 2 nm, width: 7 nm) was successfully formed. The cross-sectional size gradually decreased with decrease in the patterning width, maintaining nearly equivalent height and width. The halfway RIE was adopted, by which the NW thickness (height) was thinned to a minimum of 2 nm, while the thickness of the outside Si film remained 15 nm, and the NWs were completely supported by the buried SiO_2.

Si-NW MOSFETs with NWs fabricated and characterized in this chapter were characterized in Chaper3.

References

[1] N. Wang, Y. Cai, R. Q. Zhang, Mater. Sci. & Eng. **R60**, 1 (2008).

[2] V. Schmidt, J. V. Wittemann, S. Senz, and U. Gösele, Adv. Mater. **21**, 2681 (2009).

[3] H. Ye, Z. Gu, T. Yu, and D. H. Gracias, IEEE Trans. Nanotechnology **5**, 62 (2006).

[4] A. A. Tseng, K. Chen, C. D. Chen, and K. J. Ma, IEEE Trans. Electron. Packaging Manufacturing **26**, 141 (2003).

[5] J. Kedzierski and J. Bokor, J. Vac. Sci. Technol. B **17**, 3244 (1999).

[6] N. Singh, A. Agarwal, L. K. Bera, T. Y. Liow, R. Yang, S. C. Rustagi, C. H. Tung, R. Kumar, G. Q. Lo, N. Balasubramanian, and D.-L. Kwong, IEEE Electron Device Lett. **27**, 383 (2006).

[7] V. Pott, K. E. Moselund, D. Bouvet, L. D. Michielis, and A. M. Ionescu, IEEE Trans. Nanotechnology **7**, 733 (2008).

[8] Y. Liu, M. Masahara, K. Ishii, T. Sekigawa, H. Takashima, H. Yamauchi, and E. Suzuki, IEEE Electron Device Lett. **25**, 510 (2004).

[9] T. Tezuka, E. Toyoda, S. Nakaharai, T. Irisawa, N. Hirashita, Y. Moriyama, N. Sugiyama, N. Taoka, Y. Yamashita, O. Kiso, M. Harada, T. Yamamoto, and S. Takagi, *Tech. Dig. of 2007 Int. Electron Devices Meeting* (2007) p. 887.

[10] J. Chen, T. Saraya, K. Miyaji, K. Shimizu, and T. Hiramoto, Jpn. J. Appl. Phys. **48**, 011205 (2009).

Chapter 3

Electron and hole mobility in Si-nanowire MOSFETs

3.1 Introduction

Mobility plays an important role in the performance of MOSFETs, and for CMOS applications, both electron and hole mobility must be high. For nanowire (NW) MOSFETs, such NW structure as shape and crystal orientation greatly influences the mobility, because NWs have unique band structure (effective mass) that depends on the NW structure (Section 1.2.2). Although mobility in Si-NW MOSFETs has already been investigated [1-7], the cross-sectional size of the Si NWs generally ranges from 100 to 10 nm, where mobility is mostly explained by the combination of bulk-MOSFET mobility with different channel faces [1, 2, 6]. The reported values of mobility vary widely, which partly originates in errors of mobility evaluation. To correctly evaluate the mobility of NW MOSFETs, conductance and gate-NW capacitance must be accurately measured by eliminating parasitic capacitance and resistance. Since gate-NW capacitance is very small, many long NWs, for example, 1,000 NWs with a length of 2~4 μm [1, 2], are needed to increase the capacitance to a measurable level. However, to fabricate a NW with a length of a few μms and a cross-sectional size below 10 nm is very difficult.

In this study, 100-nm-long Si-NW MOSFETs with cross-sectional size below 10 nm were characterized to investigate the unique mobility originating in unique band structure. Gate-NW capacitance was correctly calculated from the cross-sectional structure measured by TEM using a two-dimensional device simulator. To get more information about mobility, electron and hole mobilities were compared and characterized in one Si NW using a special device structure.

3.2 Device structure and fabrication

Figure 3.1 illustrates the schematic structure of the Si NW MOSFETs fabricated in this study. The dimensions in the parallel direction to the NW were shown in Fig. 3.1(b): the length of the NW, the low impurity-concentration area, the gate electrode, and the gap between the source and drain electrodes were 0.1, 10, 22, and 30 μm, respectively. The cross-sectional size (W, square root of

cross-sectional area) of the NWs was reduced from 18 to 4 nm (Figs. 2.4 and 2.7) by changing the patterning width (W_P). The sides and top of the Si NW were covered with a 15- to 20-nm-thick gate-insulator SiO_2 and with a gate-electrode Al. The bottom of the Si NW was supported by a 200-nm-thick buried SiO_2. The direction of the NWs, which were formed from a (001) Si-film, was [100] or [110]. The doping concentration in the NW remained low as the starting material of the p-type with a resistivity of 5~50 Ω·cm was used. To evaluate both the electron and hole transport characteristics in one NW, one device contained both n^+ and p^+ regions, and one Si NW. The device included parasitic factors connected to the Si-NW MOSFET in series: Si-film MOSFETs, resistance of n^+/p^+ region, and contact resistance between source/drain electrodes and n^+/ p^+ region.

The fabrication procedure of NWs is described in Chapter 2 in detail. The n^+/ p^+ region was formed by P/B implantation at 17/7 keV with a dose of $1\times10^{14}/4\times10^{14}$ cm^{-2}, and implanted dopants were electrically activated during the 3rd and 4th oxidations (Section 2.2). A 505-nm-thick gate electrode was formed by Al evaporation. Hydrogen-termination treatment at the Si interfaces was carried out in forming gas of N_2 = 0.27 slm and H_2 = 0.03 slm at 450˚C for 10 min. For source and drain electrodes, 478/36-nm-thick Al/Ti was evaporated on n^+ region and 498-nm-thick Al on p^+ region. Contact annealing was carried out in forming gas of N_2 = 0.27 slm and H_2 = 0.03 slm at 350˚C for 10 min.

3.3 Characterization method of mobility and other characteristics

Drain current I_D of the MOSFETs can be expressed as [8]

$$I_D = g_{m,0}\frac{(V_G - V_{th} - V_D/2)}{1+\theta(V_G - V_{th} - V_D/2)}, \tag{3.1}$$

$$g_{m,0} \equiv \frac{\mu_0 C_{OX} V_D}{L}, \tag{3.2}$$

$$\theta \equiv \frac{\mu_0 C_{OX}}{L} r + \theta_\mu, \tag{3.3}$$

by assuming the following: dependence of mobility μ on gate voltage V_G (electric field) as [9-11]

$$\mu = \frac{\mu_0}{1+\theta_\mu(V_G - V_{th} - V_D/2)}, \tag{3.4}$$

parasitic ohmic resistance r connected to the MOSFET in series, the contribution of the Si-film MOSFET being negligible, and $V_G >> V_D$. C_{OX} is the capacitance of the gate-insulator SiO_2 per unit length of NWs, L is the NW length of 100 nm, μ_0 is the low field mobility, θ_μ is the mobility reduction coefficient, and V_{th} is the threshold voltage. Equation (3.1) is transformed to

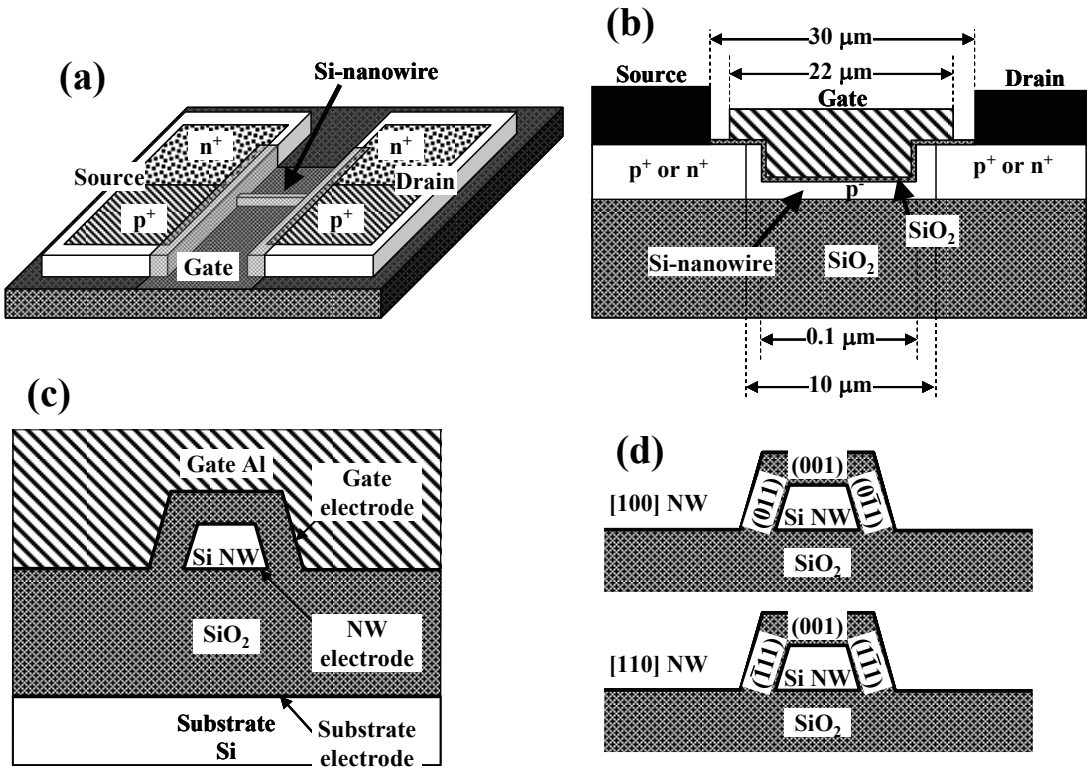

Fig. 3.1 The schematic structure of the fabricated Si-NW MOSFET: (a) the bird's-eye view, (b) the cross-sectional view parallel to the NW, (c) the cross-sectional view perpendicular to the NW, (d) The crystal faces of [110] and [100] NWs. The source/drain electrodes and SiO_2 covering Si NWs are omitted in (a). The setting of the electrodes to calculate C_{OX} and C_{BOX} is shown in (c) as bold lines. The crystal faces of the sides shown in (d) are high symmetry faces close to the actual side faces.

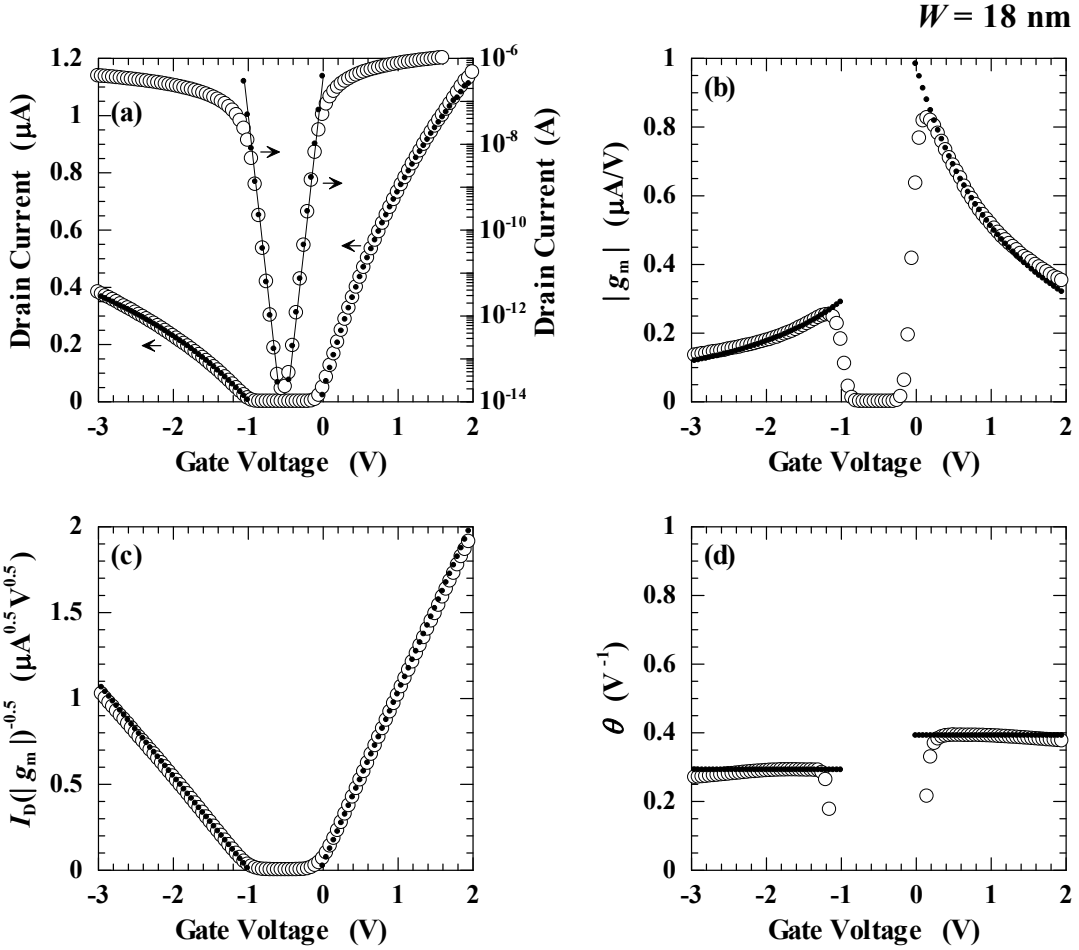

Fig. 3.3 The gate voltage (V_G) dependence of (a) I_D, (b) $|g_m|$, (c) $I_D(|g_m|)^{-0.5}$, and (d) θ of the [100] Si-NW MOSFET with W = 18 nm at V_D = 50 mV. The open circles show values derived from the measured I_D-V_G characteristics, where θ was calculated using $g_{m,0}$ and V_{th}. The closed circles show fitting results calculated using the parameters: $g_{m,0,e}$ = 1.00 μA/V, $g_{m,0,h}$ = 0.29 μA/V, $V_{th,e}$ = −0.05 V, $V_{th,h}$ = −1.01 V, θ_e = 0.39 V^{-1}, θ_h = 0.29 V^{-1}, S_e = 63.5 mV/decade, and S_h = 64.1 mV/decade.

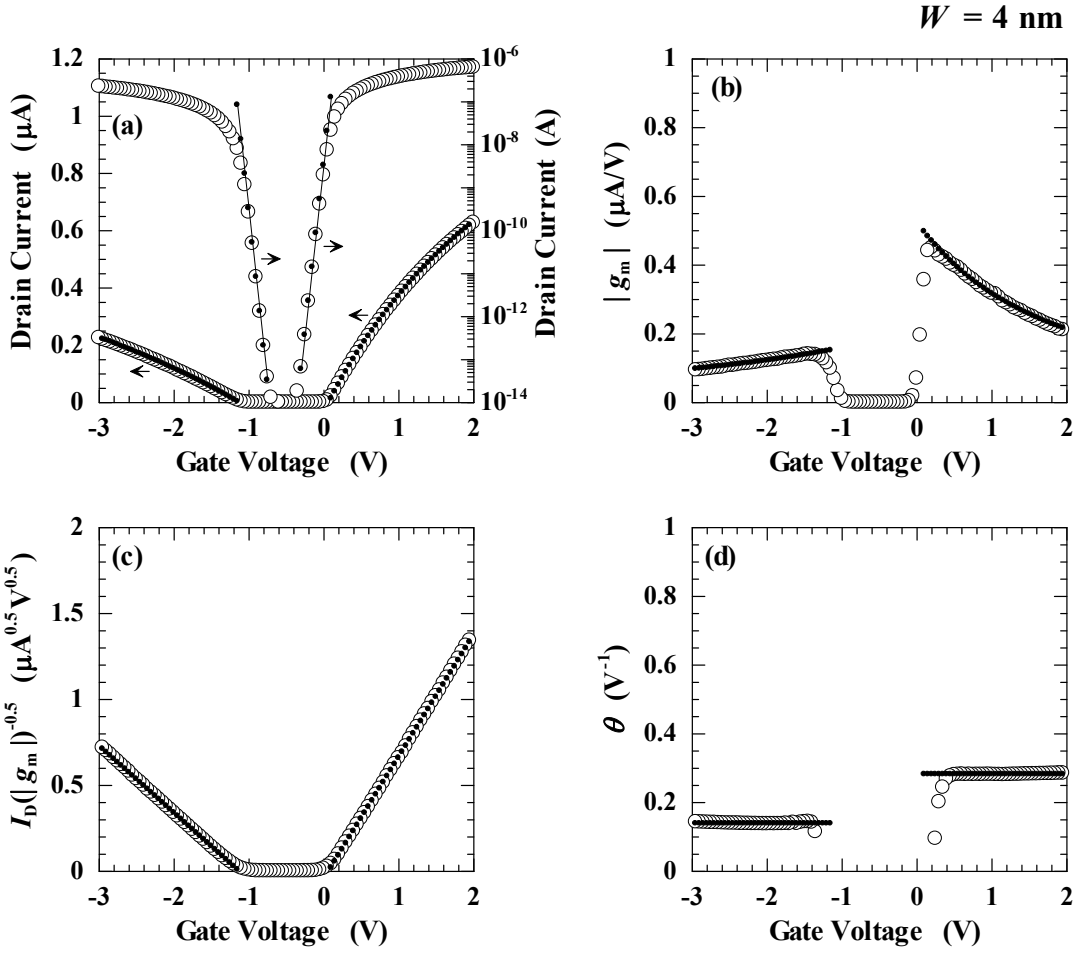

Fig. 3.4 The gate voltage (V_G) dependence of (a) I_D, (b) $|g_m|$, (c) $I_D(|g_m|)^{-0.5}$, and (d) θ of the [100] Si-NW MOSFET with W = 4 nm at V_D = 50 mV. The open circles show values derived from the measured I_D-V_G characteristics, where θ was calculated using $g_{m,0}$ and V_{th}. The closed circles show fitting results calculated using the parameters: $g_{m,0,e}$ = 0.50 μA/V, $g_{m,0,h}$ = 0.15 μA/V, $V_{th,e}$ = 0.05 V, $V_{th,h}$ = −1.15 V, θ_e = 0.28 V^{-1}, θ_h = 0.14 V^{-1}, S_e = 63.1 mV/decade, and S_h = 62.4 mV/decade.

$$\frac{I_D}{\sqrt{g_m}} = \sqrt{g_{m,0}}(V_G - V_{th} - V_D/2), \tag{3.5}$$

where g_m is the transconductance:

$$g_m \equiv \frac{\partial I_D}{\partial V_G} = g_{m,0}\frac{1}{\{1+\theta(V_G - V_{th} - V_D/2)\}^2}. \tag{3.6}$$

Equation (3.1) is also transformed to

$$\theta = \frac{g_{m,0}}{I_D} - \frac{1}{V_G - V_{th} - V_D/2}. \tag{3.7}$$

The $g_{m,0}$ and V_{th} were determined using Eq. (3.5) and the θ was determined using Eq. (3.7) by fitting to the measured results.

W and C_{OX} were calculated based on the structural data measured from the TEM images (Fig. 2.4). W was defined as the square root of the cross-sectional area of the Si NWs. C_{OX} was calculated by a two-dimensional Poisson's equation using a device simulator, where an infinite long NW was assumed and the dielectric constant in SiO_2 was $3.9\varepsilon_0$. The calculation procedure is as follows. Three electrodes were set as shown in Fig. 3.1(c): a gate electrode at the top of the gate-insulator SiO_2, an NW electrode at the interface of the Si NW, and a substrate electrode at the bottom of the buried SiO_2. The gate and substrate electrodes were set at 0 V, and the voltage of the NW electrode was increased to V_{NW}. C_{OX} was calculated from linear relationships between V_{NW} and charge Q_{gate} at the gate electrode, and buried oxide capacitance C_{BOX} was calculated likewise:

$$\begin{aligned} Q_{gate} &= -C_{OX}V_{NW} \\ Q_{sub} &= -C_{BOX}V_{NW} \end{aligned}. \tag{3.8}$$

Calculated C_{OX} and C_{BOX} are simply geometric capacitances of SiO_2, do not include the capacitance inside the Si NW [12-14], and independent of the voltages of the three electrodes following principle of superposition [15].

From the subthreshold characteristics, subthreshold threshold-voltage $V_{th,sub}$ was determined as gate voltage at $I_D = 1\times10^{-11}$ A and subthreshold swing S as

$$S \equiv \ln 10 \frac{\partial V_G}{\partial(\ln I_D)}. \tag{3.9}$$

3.4 Device characterization and discussion

3.4.1 Gate characteristics

Figures 3.3 and 3.4 show the typical V_G dependence of I_D, g_m, $I_D(g_m)^{-0.5}$, and θ for thick (W = 18

nm) and thin (W = 4 nm) [100] NW MOSFETs at room temperature, respectively. The drain voltage V_D was set at 50 mV, and the substrate voltage was fixed at 0 mV. Open circles show the values derived from measured I_D-V_G characteristics, where θ was calculated from Eq. (3.7) using the determined characteristics of $g_{m,0}$ and V_{th}. Closed circles show the fitting results calculated from Eqs. (3.1)-(3.7) using the determined parameters of $g_{m,0}$, V_{th}, and θ. For $V_G > -0.5$ V, the MOSFET works as an n-channel MOSFET, and I_D is carried by electrons. For $V_G < -0.5$ V, the MOSFET works as a p-channel MOSFET, and I_D is carried by holes. The MOSFET characteristics can be expressed by the model described in Section 3.3: experimental $I_D(g_m)^{-0.5}$ was changed linearly with V_G and θ calculated from Eq. 3.7 using measured I_D-V_G characteristics was almost constant with V_G. Subthreshold I_D was well expressed by an exponential function of V_G.

3.4.2 Parasitic resistance and gate-voltage dependence of mobility

Figure 3.5 shows W_P dependence of θ of [100] NW MOSFETs at room temperature. The θ for n-/p-channel conduction is specified by subscript "e"/"h." Average value of θ_e and θ_h for all W_P were 0.33 and 0.31 V^{-1}, respectively, which is similar to θ_μ (= 0.27 V^{-1}) of bulk-Si MOSFETs with a 20-nm-thick gate-SiO_2 [11] and θ_μ (= 0.29 V^{-1}) of Si-NW MOSFETs with a 3.5-nm-thick gate-SiO_2 [16], which indicates that parasitic resistance (r) is negligible and that θ_μ (V_G dependence of mobility) takes a similar value to that of bulk MOSFETs even for small W. The θ_h may decrease with a W_P decrease, but the decrease was within the range of experimental dispersion. To reduce parasitic resistance, thickening of Si film connected to the Si-NW is important, and the thickness was 15 nm (Section 2.3.2).

3.4.3 Gate-insulator capacitance

Figure 3.6(a) shows W_P dependence of C_{OX} and C_{BOX} of [100] NW MOSFETs calculated from the cross-sectional structures (Fig. 2.4). Both C_{OX} and C_{BOX} gradually decreased with a W_P decrease. The C_{BOX} was much smaller than C_{OX}, and the ratio C_{BOX}/C_{OX} is shown in Figure 3.6(b). The ratio C_{BOX}/C_{OX} was about 0.05.

3.4.4 Derivation of cross-sectional size dependence of mobility and threshold voltage

Figures 3.7 and 3.8 show W_P dependence of $g_{m,0}$ and V_{th}, respectively, of [100] NW MOSFETs at room temperature determined from the method described in Section 3.3. The values of the MOSFETs that measured and worked normally (measured devices) are shown as open symbols. Both $g_{m,0}$ and V_{th} gradually changed with a W_P decrease, and the experimental dispersion was small.

To derive W dependence of mobility and threshold voltage, W and C_{OX} are needed. Since the

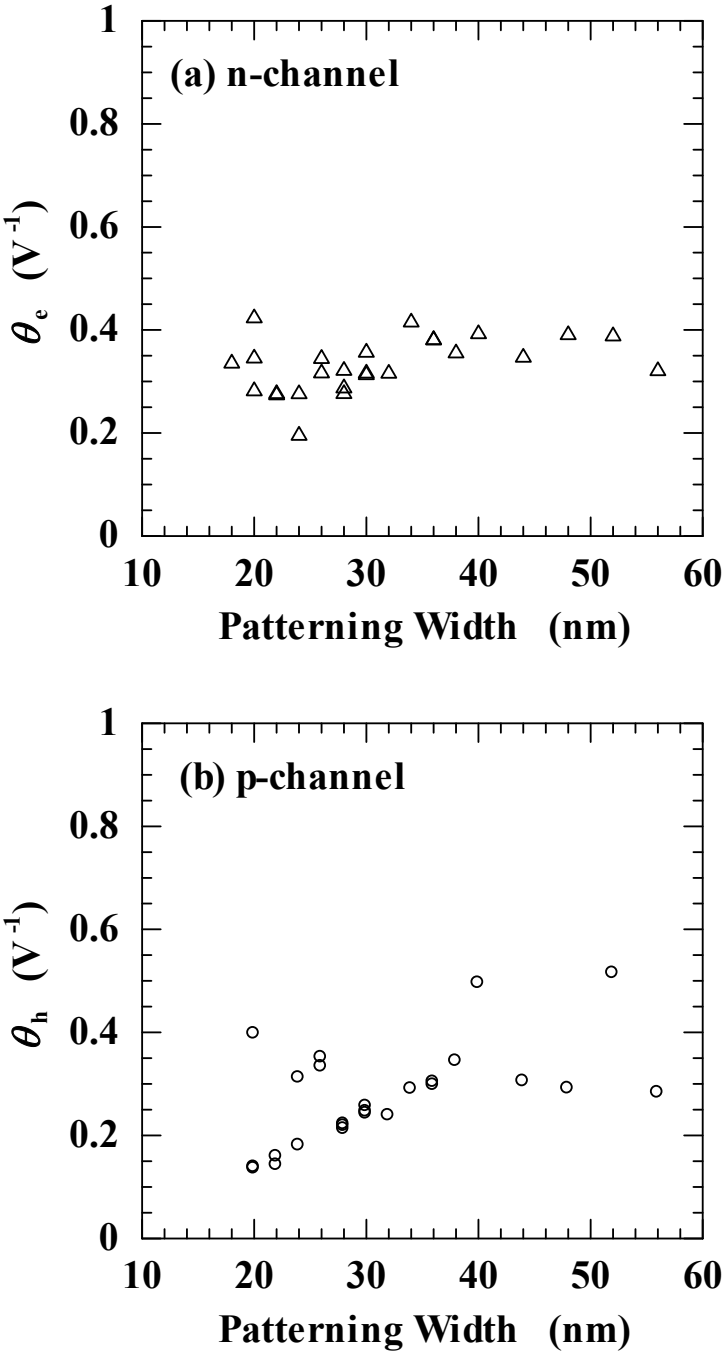

Fig. 3.5 The patterning width (W_P) dependence of the (a) θ_e (n-channel) and (b) θ_h (p-channel) of the [100] Si-NW MOSFETs.

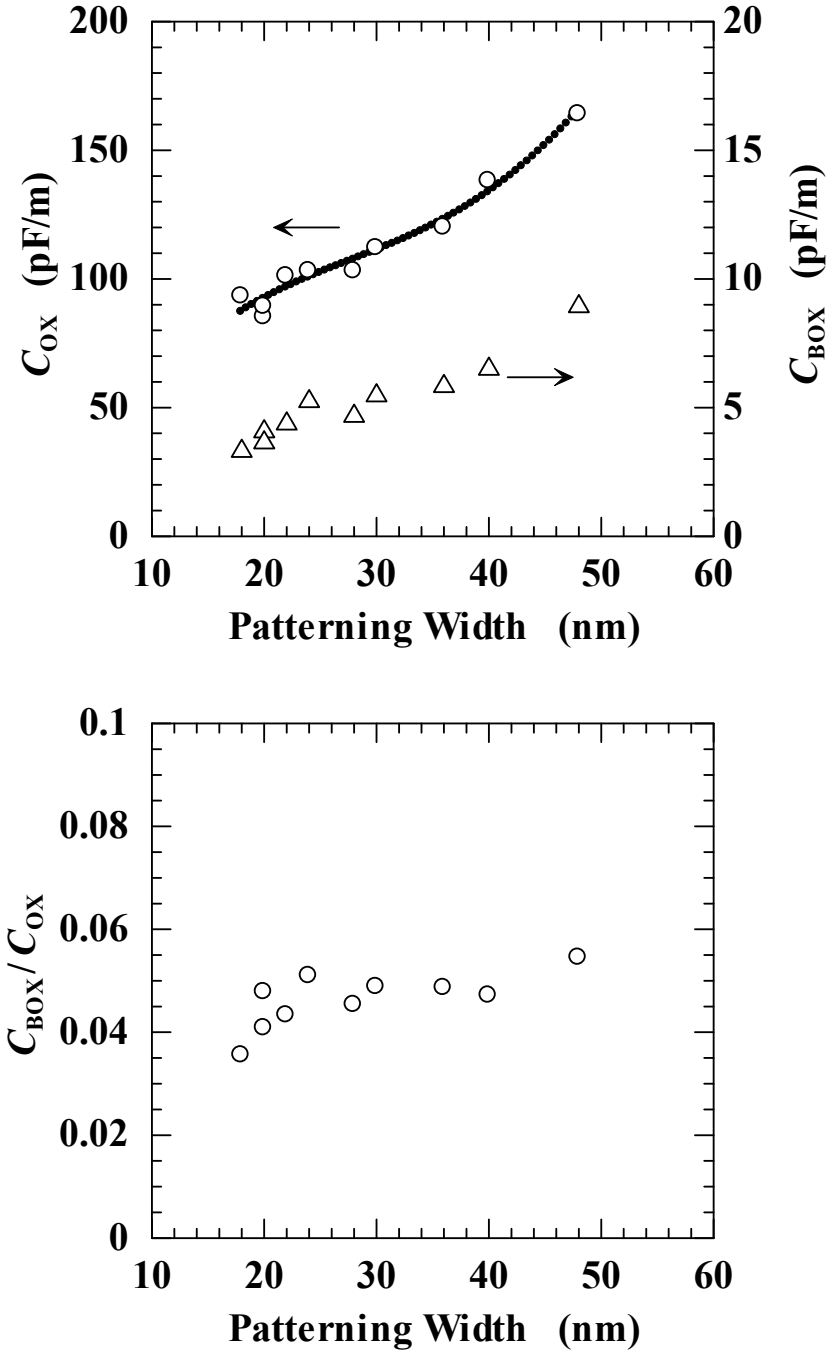

Fig. 3.6 (a) The capacitance C_{OX} and C_{BOX} calculated for the "TEM samples" based on the structural data measured from the TEM images, and (b) The ratio C_{BOX}/C_{OX}. The closed symbols show a fitting result.

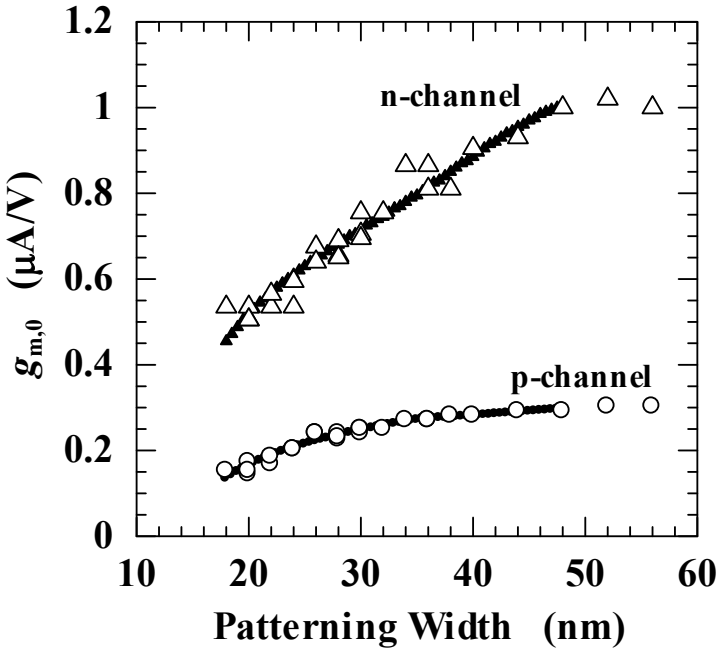

Fig. 3.7 The patterning width (W_P) dependence of the $g_{m,0}$ of the [100] Si-NW MOSFETs ("measured devices"). The closed symbols show fitting results.

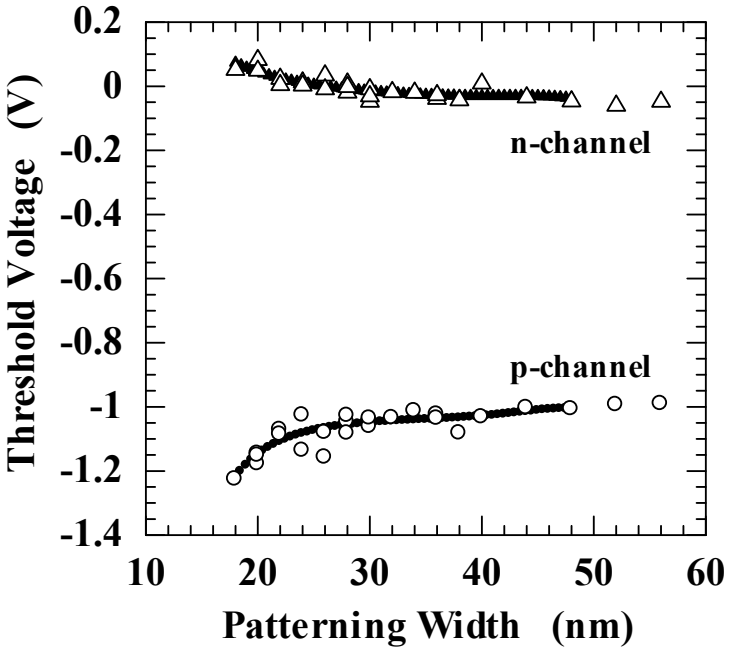

Fig. 3.8 The patterning width (W_P) dependence of the threshold voltage (V_{th}) of the [100] Si-NW MOSFETs ("measured devices"). The closed symbols show fitting results.

structure was measured only for ten NW MOSFETs (TEM samples), W dependence of mobility and threshold voltage can be derived only for TEM samples. Since determining the trend of W dependence from few TEM samples is difficult, additional data was derived as follows. The approximate relations of W-W_P (closed symbols in Fig. 2.7) and C_{OX}-W_P (closed symbols in Fig. 3.6(a)) were determined by fitting them into the results of TEM samples (open symbols). On the other hand, the approximate relations of $g_{m,0}$-W_P (closed symbols in Fig. 3.7) and V_{th}-W_P (closed symbols in Fig. 3.8) were determined by fitting them into the results of measured devices (open symbols). Then the approximate relations of μ_0-W, V_{th}-W, and so on were calculated from the approximate relations of W-W_P, C_{OX}-W_P, $g_{m,0}$-W_P, and V_{th}-W_P and were plotted in Figs 3.10, 3.14, and 3.16 as gray symbols. That is, the gray symbols show the approximate values, not for the TEM samples, but for the measured devices. On the other hand, the W dependence of μ_0, V_{th}, and so on for TEM samples which was derived by using their own W and C_{OX} (open symbols in Figs. 2.7 and 3.6(a)) was plotted in Figs 3.10, 3.14, and 3.16 as open symbols.

3.4.5 Subthreshold swing and threshold voltage shift by quantum confinement effect

Figure 3.9 shows W_P dependence of S of [100] NW MOSFETs at room temperature. The S for n-/p-channel conduction is specified by subscript "e"/"h." S_e and S_h were about 63 mV/decade at 293 K and almost unchanged with a W_P decrease. The value of 63 mV/decade is very close to the minimum value of 58.1 mV/decade (= (ln10)kT/e). The degradation from the minimum value partly originates in a substrate effect. The NW channel is not completely surrounded by the gate electrode, and the bottom part faces the substrate. For a long-channel MOSFET, S, considering the substrate effect, is given by [17, 18]

$$m = 1 + C_{BOX} / C_{OX}, \tag{3.10}$$

where

$$m \equiv S \frac{e}{(\ln 10) kT}. \tag{3.11}$$

The S (m) calculated using Eqs. (3.10) and (3.11) and the capacitance (Fig. 3.6) was about 61 mV/decade (1.05) for all the W. The additional degradation of 2 mV/decade probably originates in the interface traps.

Figure 3.10(a) shows W dependence of V_{th} and $(V_{th,e}+V_{th,h})/2$ of [100] NW MOSFETs at room temperature and Fig. 3.10(b) shows W dependence of $V_{th,e}-V_{th,h}$, where the quantities for n-/p-channel conduction was specified by subscript "e"/"h." The Fermi level E_F in the Si channel near the MOS interface at V_G = 0 should lie slightly below the conduction band minimum E_C ($E_C-E_F \approx 0.1$ eV) in consideration of the work function difference between channel Si and gate Al [19]. The MOSFETs turn on as an n-channel MOSFET when E_F rises to a level slightly below the E_C and turn on as a p-channel MOSFET when E_F falls to a level slightly above the valence band

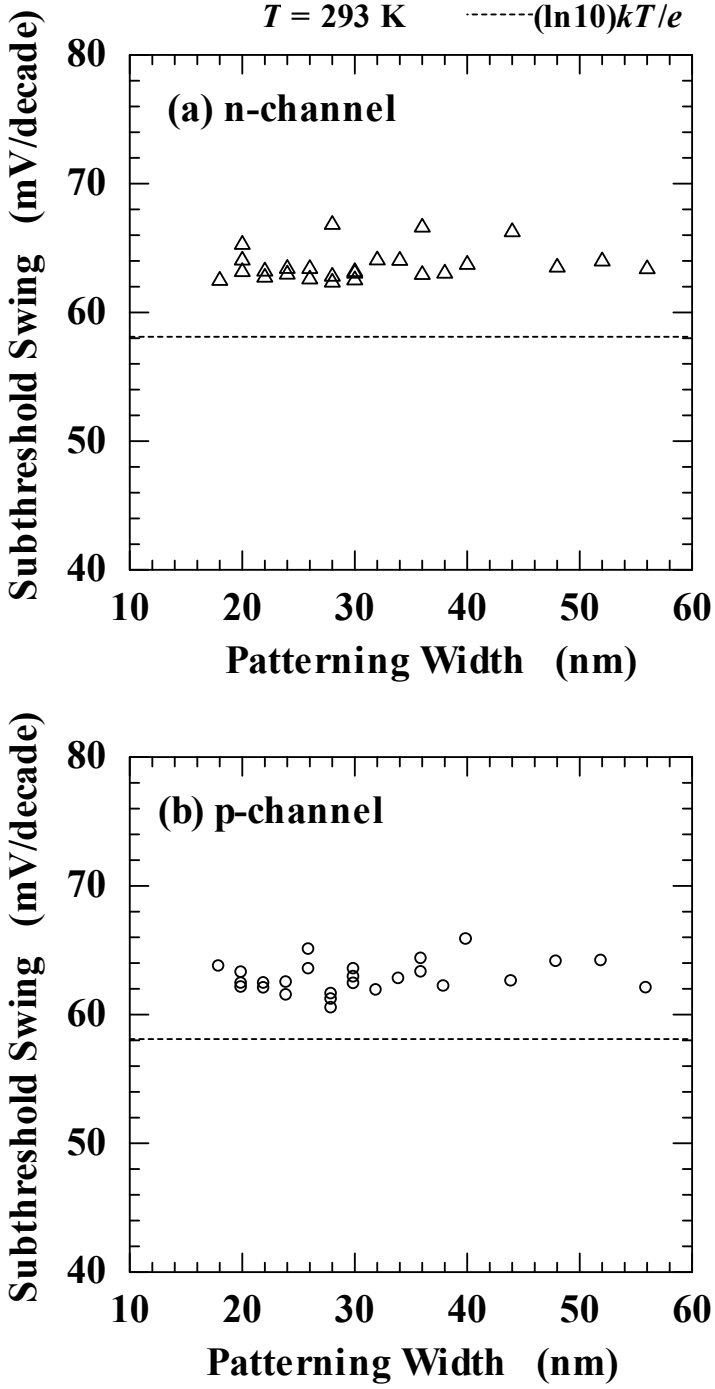

Fig. 3.9 The patterning width (W_P) dependence of the subthreshold swing (a) S_e (n-channel) and (b) S_h (p-channel) of the [100] Si-NW MOSFETs. The minimum value of 58.1 mV/decade (= (ln10)kT/e) is shown as a broken line.

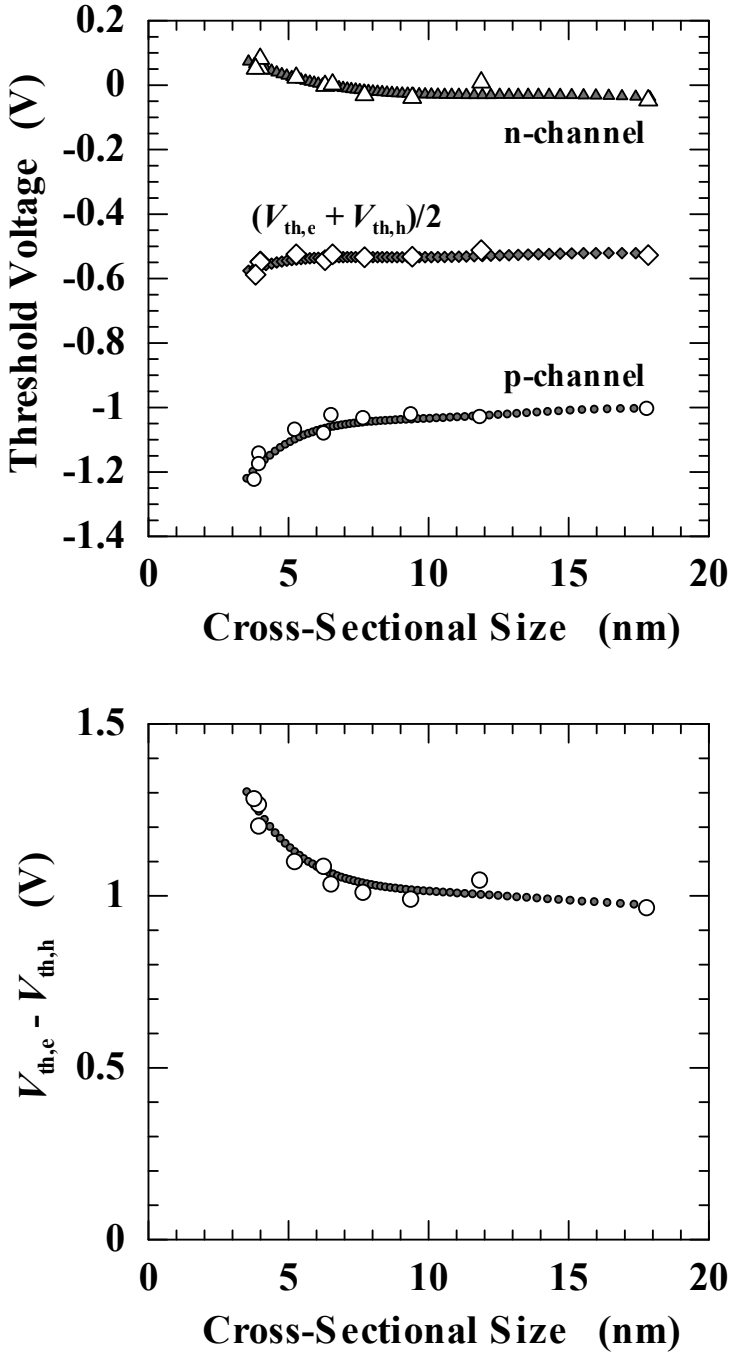

Fig. 3.10 The cross-sectional size (W) dependence of (a) the threshold voltage (V_{th}) and the $(V_{th,e}+V_{th,h})/2$, and (b) the $V_{th,e}-V_{th,h}$ of the [100] Si-NW MOSFETs. The open symbols show the results for the "TEM samples." The gray closed symbols show fitting results for the "measured devices."

maximum. For MOSFETs with large W, with which the electronic states in the Si-NW channel remain bulk states, $V_{th,e}$ and $V_{th,h}$ were −0.05 V and −1.00 V, respectively, as shown in Fig. 3.10(a). Then, $V_{th,e}-V_{th,h}$ is 0.95 V (Fig. 3.10(b)), which is slightly smaller than the bulk band-gap (1.12 eV). The results indicate that the charges in the gate-SiO_2 and/or trapped at the interface are negligible. The $V_{th,e}$ gradually increased with a W decrease, and $V_{th,h}$ decreased. The V_{th} shift undoubtedly results from the band-edge shift by quantum confinement effect [20]. The degree of the $V_{th,e}$ shift was smaller than that of the $V_{th,h}$ shift, which can be grasped from the small decrease of $(V_{th,e} + V_{th,h})/2$ (Fig. 3.10(a)). The result is valid because the electron effective mass in the confinement direction ($0.98m_0$) is larger than that of the holes ($0.53m_0$).

For the subthreshold region, the change of Fermi level ΔE_F in the Si channel is related to the change of gate voltage ΔV_G as [21]

$$m\Delta E_F = e\Delta V_G . \tag{3.12}$$

Then band-gap shift $E_{g,NW} - E_{g,bulk}$ is given by

$$m(E_{g,NW} - E_{g,bulk}) = e(V_{th,e} - V_{th,h})_{NW} - e(V_{th,e} - V_{th,h})_{bulk}, \tag{3.13}$$

and was plotted in Fig. 3.11 as a function of W, where $(V_{th,e}-V_{th,h})_{bulk}$ was set at 0.95 V and m (S) was set at the average values of 1.09 (63 mV/decade) for all MOSFETs. Band-gaps of [100] Si-NWs calculated by tight-binding method [22, 23], density functional theory [24], and effective mass approximation (Section 1.2.2) are also plotted. The band-gap shift derived from the threshold-voltage shift well corresponded to the shifts calculated theoretically. Figure 3.12 illustrates the band structure of Si NWs.

Figure 3.13 shows relationship between V_{th} and $V_{th,sub}$. The V_{th} and $V_{th,sub}$ had a linear relationship, the difference between $V_{th,sub}$ and V_{th} was equivalent among the devices for both n- and p-channel conductions, and the value of the difference was about 0.23 V. Therefore, a equivalent band-gap shift is derived by using $V_{th,sub}$ instead of V_{th}.

3.4.6 Size and temperature dependence of mobility and comparison between electron and hole mobility

Figure 3.14 shows W dependence of $\mu_{0,e}$ and $\mu_{0,h}$ of [100] NW MOSFETs at room temperature, where the mobility of electrons/holes was specified by subscript "e"/"h." The $\mu_{0,e}$ and $\mu_{0,h}$ increased with a W decrease to about 9 nm, but decreased with a W decrease from about 9 to 4 nm. The slow increase for $W > 9$ nm probably originates in an error by ignoring the Si-film MOSFETs. By the error, μ_0 is underestimated and the degree of the underestimation is larger for thicker NWs.

The mobility decrease for $W < 9$ nm probably originates in the increase of the surface-roughness scattering in Si NWs. The temperature dependence of $\mu_{0,e}$ and $\mu_{0,h}$ is shown in Fig. 3.15(a), and the ratios at 200 K and 400 K ($\mu_{0,200K}/\mu_{0,400K}$) are shown in Fig. 3.15(b), where the ratios of bulk MOSFETs are also shown [25]. For both $\mu_{0,e}$ and $\mu_{0,h}$, mobility increased with decrease of temperature and $\mu_{0,200K}/\mu_{0,400K}$ was similar to that of bulk MOSFETs, which indicates that phonon

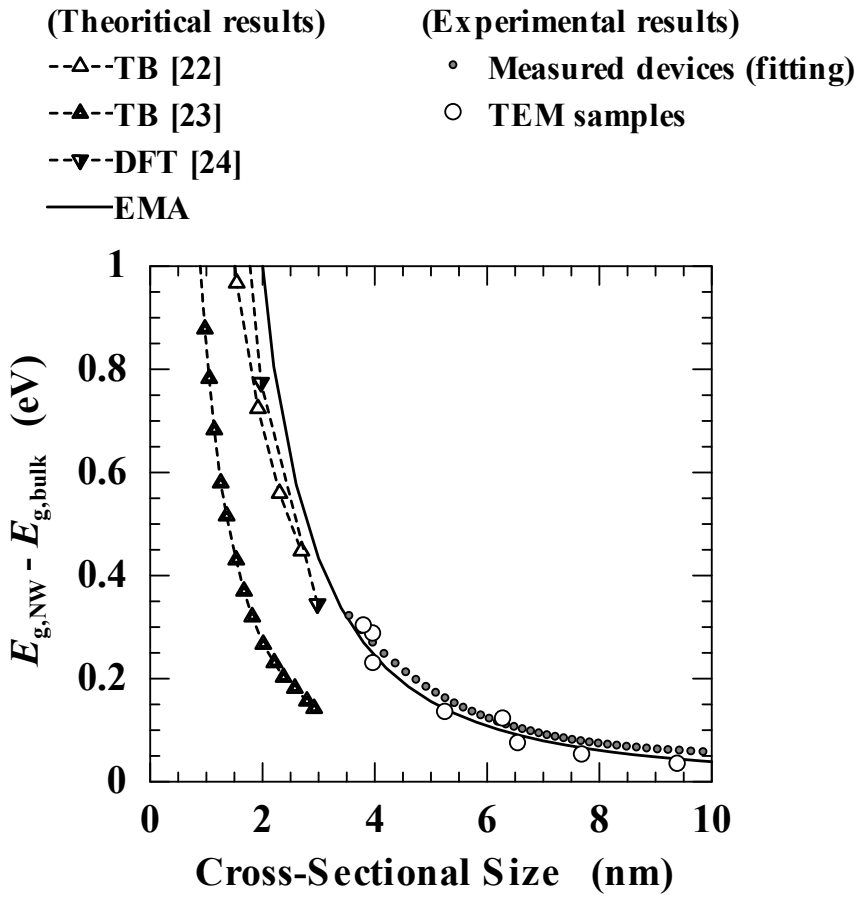

Fig. 3.11 The cross-sectional size (W) dependence of the band-gap of [100] Si-NWs calculated from the threshold-voltage shift of the MOSFETs: the open circles show the results for the "TEM samples" and the gray closed circles show a fitting result for the "measured devices." Band-gaps of [100] Si-NWs calculated by tight-binding method (TB) [22, 23], density functional theory (DFT) [24], and effective mass approximation (EMA) (Section 1.2.2) are also plotted.

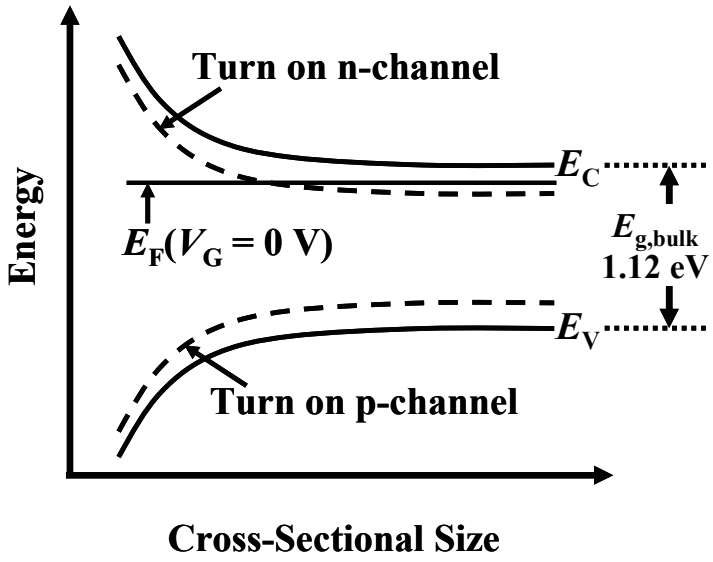

Fig. 3.12 Illustration of the band structure of Si NWs.

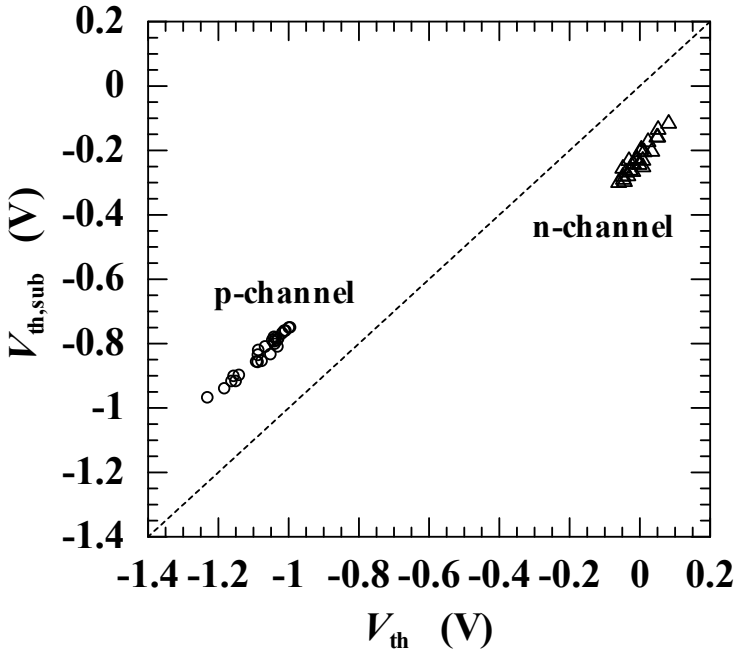

Fig. 3.13 The relationship between the V_{th} and the $V_{th,sub}$ of the [100] Si-NW MOSFETs.

scattering is dominant. The temperature dependence became small with a W decrease to below 9 nm, which can be easily grasped from the decrease of $\mu_{0,200K}/\mu_{0,400K}$. Since the temperature dependence of the mobility becomes small when the surface-roughness scattering becomes strong [26], the decrease of $\mu_{0,200K}/\mu_{0,400K}$ with a W decrease indicates that the surface-roughness scattering becomes strong with a W decrease. The decrease of the $\mu_{0,200K}/\mu_{0,400K}$ of the holes was larger than that of electrons, which indicates that the hole-mobility degradation by the surface-roughness-scattering increase is more severe than that for the electrons.

Figure 3.16 shows W dependence of mobility ratio $\mu_{0,h}/\mu_{0,e}$ at room temperature. By evaluating the ratio, changes not observed in the μ_0 itself were detected. The mobility ratio increased with a W decrease for $W > 7$ nm and decreased with a W decrease for $W < 7$ nm. The change for $W > 7$ nm can almost be explained by the confinement effect by an electric field perpendicular to a channel face, which was induced by gate voltage. The electric-field-confinement effect was observed for bulk MOSFETs as mobility differences depending on channel faces [16, 27]. Fig. 3.17(a) shows bulk-MOSFET mobility on {100}, {110}/<001>, and {111} [27], and Fig. 3.17(b) shows the ratio of electron and hole mobilities calculated from the results in Fig. 3.17(a). The ratios are 0.24 for {100}, 0.33 for {110}/<001>, and 0.35 for {111}, which are the average values for 2×10^{11} cm^{-2} < $N_{inv} < 2\times10^{12}$ cm^{-2}.

The cross-sectional shape of the NW with $W = 18$ nm was a trapezoid, and the channel faces consisted of a top face {100} and side faces. On the other hand, the NW shape with 7 nm < W < 12 nm was a triangle, and the channel faces consisted of only side faces. The crystal faces of the sides are not high symmetry faces but are close to {110} for both trapezoidal and triangular NWs. If the confinement conditions of carriers in the NW MOSFETs are the same as that in bulk MOSFETs, the mobility ratio of each face in NW is the same as that of bulk MOSFET with the same crystal face. That is, the ratio of trapezoidal-NW MOSFETs should be the weighted average of the ratios of bulk MOSFETs on {100} (0.24) and {110} (0.33), and the ratio of triangular-NW MOSFETs should be the ratio of bulk MOSFETs on {110} (0.33). The actual values agree well with the values derived by assuming the same confinement conditions as that in bulk MOSFETs. Therefore, carriers in NW MOSFETs with $W > 7$ nm would be confined to the interface of Si NWs like carriers in bulk MOSFETs. Although the NW remained triangular for 7 nm < W < 12 nm, the ratio slowly increased with a W decrease. The increase probably originates in the effects of the Si-film MOSFETs. Since the channel face of the Si-film MOSFETs is {100}, the ratio of the Si-film MOSFETs is 0.24. Then the ratio of triangular-NW MOSFETs is the weighted average of the ratios on {110} (triangular-NW) and {100} (Si-film). Since the effects of the Si-film MOSFETs decreases with a W increase, the ratio of triangular-NW MOSFETs increases to 0.24 with a W increase, despite keeping the triangular shape.

The ratio decrease for $W < 7$ nm cannot be explained by the ratios of bulk MOSFETs, which indicates a further change of the confinement states of carriers; volume inversion must be embodied, and the decrease may originate in the unique band structure of NWs. Volume inversion means that

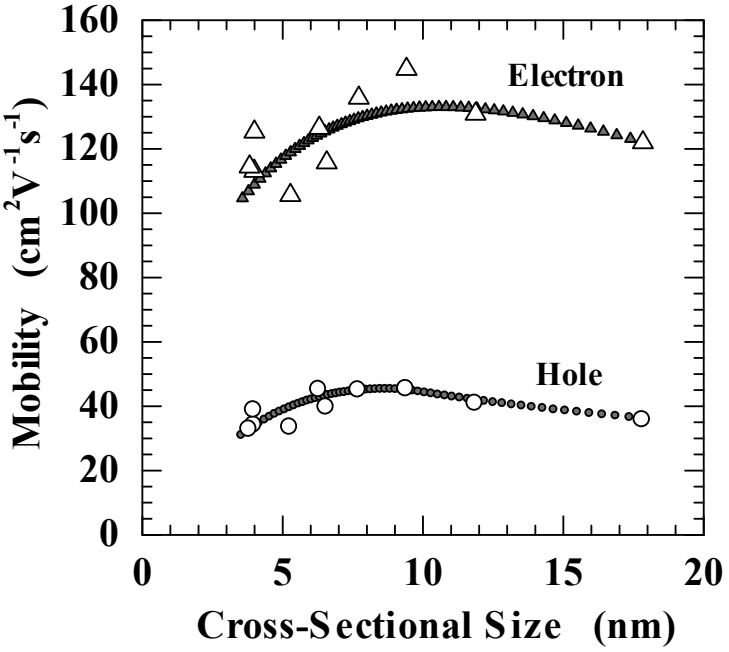

Fig. 3.14 The cross-sectional size (W) dependence of the mobility (μ_0) of the [100] Si-NW MOSFETs. The open symbols show the results for the "TEM samples." The gray closed symbols show fitting results for the "measured devices."

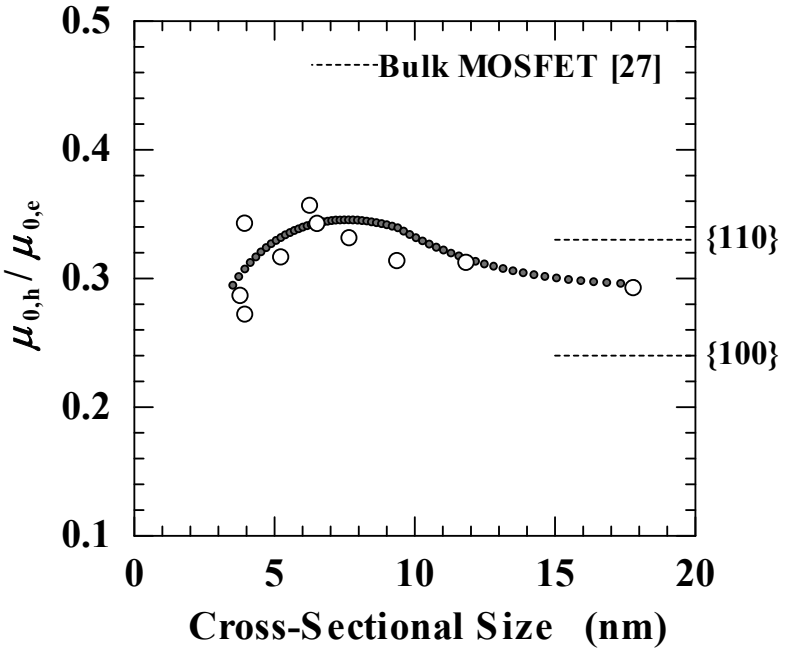

Fig. 3.16 The cross-sectional size (W) dependence of the mobility ratio $\mu_{0,h}/\mu_{0,e}$ of the [100] Si-NW MOSFETs. The open symbols show the results for the "TEM samples," the gray closed symbols show a fitting result for the "measured devices," and broken lines show the ratio of bulk MOSFETs averaged for 2×10^{11} cm^{-2} < N_{inv} < 2×10^{12} cm^{-2} [27].

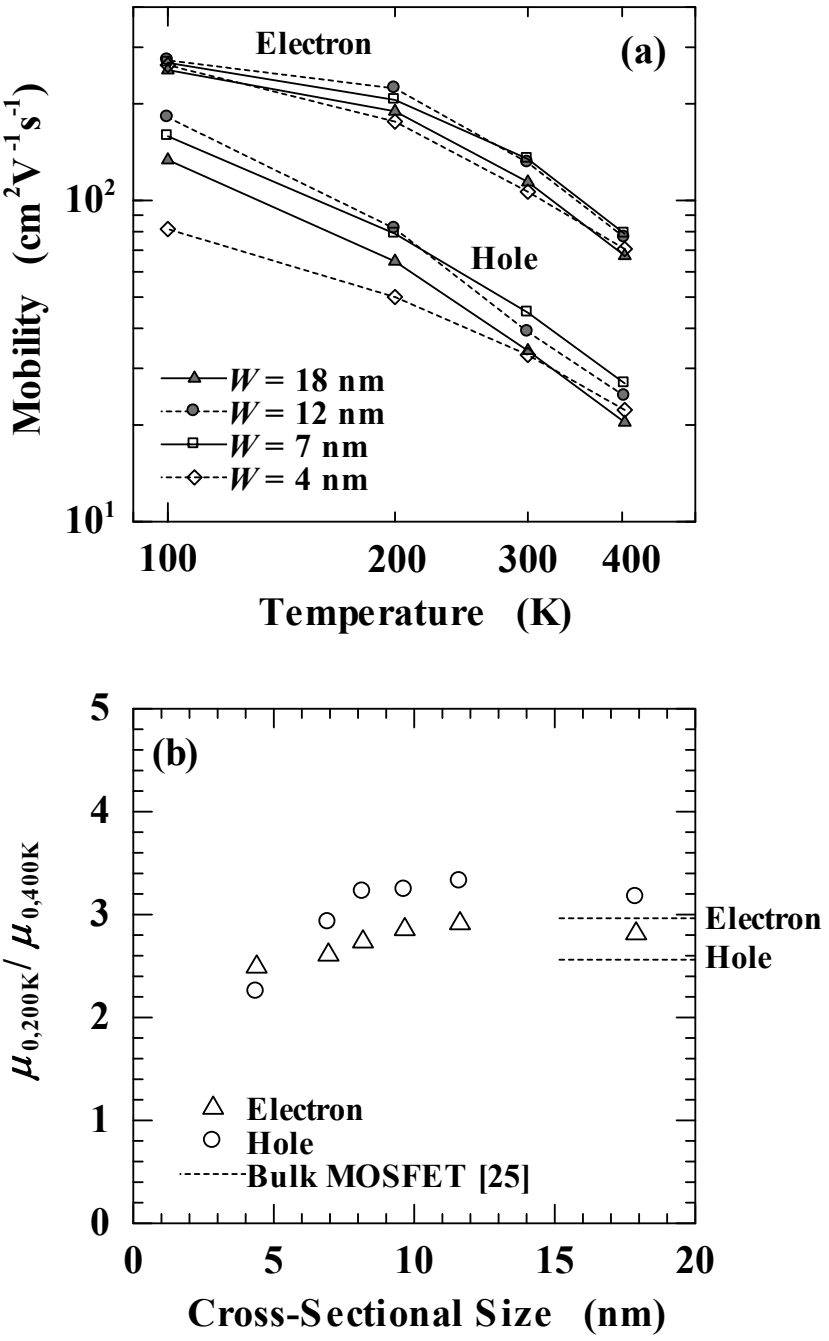

Fig. 3.15 (a) The temperature dependence of the mobility (μ_0) of the [100] Si-NW MOSFETs. (b) The ratio of the μ_0 at 200 K and 400 K as a function of cross-sectional size (W), where broken lines show the ratio of bulk MOSFETs [25].

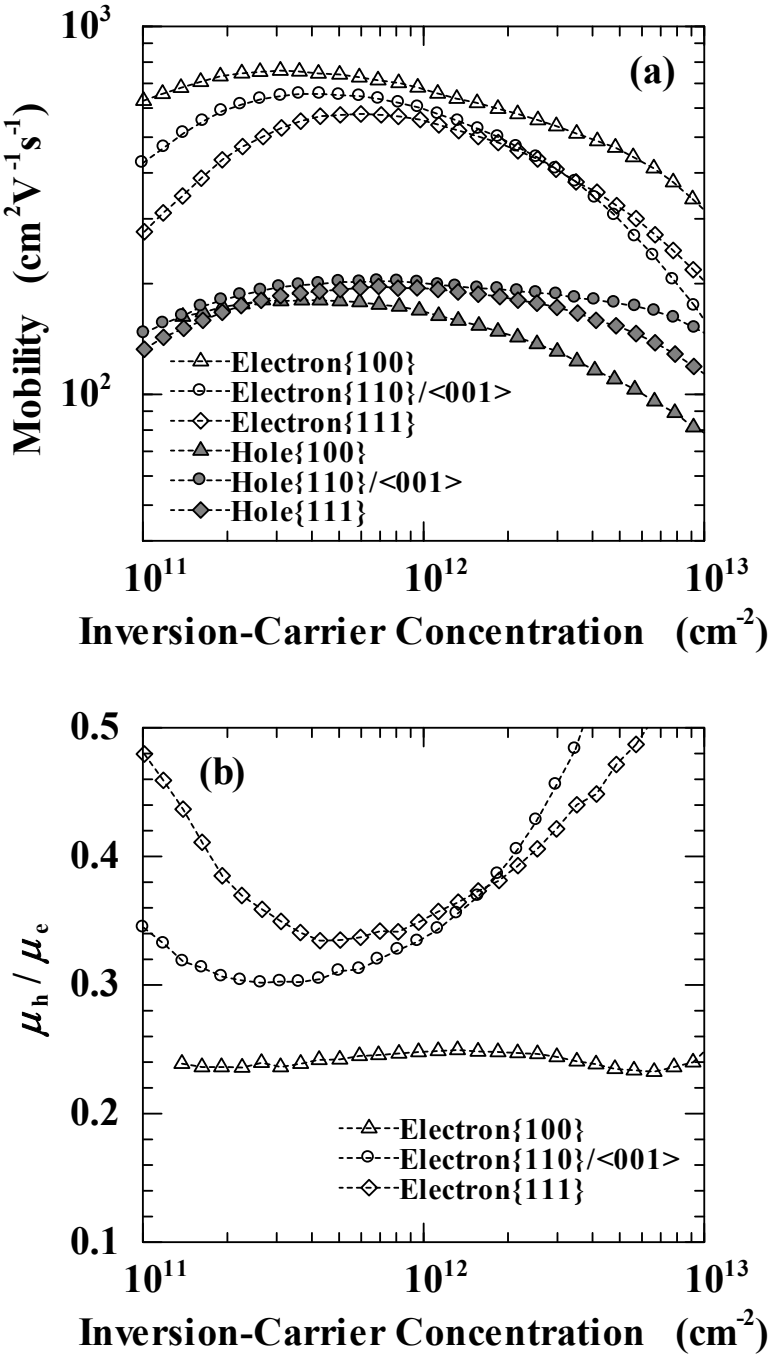

Fig. 3.17 (a) The bulk-MOSFET mobility on {100}, {110}/<001>, and {111} as a function of inversion-carrier concentration (N_{inv}) [27]. (b) The ratio of electron and hole mobility calculated from the results in (a).

the NW size is smaller than the channel thickness, and that carriers are confined not by electric fields but by a SiO_2 potential surrounding the Si NW and are distributed throughout the NW. Figure 3.18 illustrates the carrier-confinement conditions. The size (W = 7 nm) that the mobility ratio $\mu_{0,h}/\mu_{0,e}$ started to decrease was close to the size (W = 9 nm) that the mobility $\mu_{0,e}$ and $\mu_{0,h}$ started to decrease. This result indicates that the carriers under the volume inversion condition are confined nearer to the surface than those under the electric-field-confinement condition and surface-roughness scattering increases, which is opposite result to expectation in Ref. 28. However, the calculation in Ref. 29 shows that volume inversion is realized for $W < 5$~10 nm at $V_G = V_{th}$, which is well consistent with my result.

Carrier concentration (N_{inv}) per channel area was estimated to compare with that in bulk MOSFETs by

$$N_{inv} = \frac{C_{OX}(V_G - V_{th})}{eW_C}, \tag{3.14}$$

where the values of C_{OX} = 100~150 pF/m and W_C = 7~30 nm (channel width) was used. The estimated N_{inv} was 9×10^{11}~3×10^{11} cm^{-2} for $V_G - V_{th}$ = 0.1 V and 2×10^{13}~6×10^{12} cm^{-2} for $V_G - V_{th}$ = 2 V. Therefore, NW MOSFETs were evaluated at similar carrier concentration to bulk MOSFETs.

3.4.7 Comparison between [100]- and [110]-nanowire MOSFETs

Figures 3.19 shows the (a) $g_{m,0}$, (b) $\mu_{0,h}/\mu_{0,e}$, (c) V_{th}, and (d) the $V_{th,e} - V_{th,h}$ of [110]- and [100]-NW MOSFETs at room temperature, where $g_{m,0}$ and W_P were used instead of μ_0 and W because TEM observations were not performed for [110]-NW MOSFETs. All the quantities for the two directions agreed well.

The shapes of the [110] and [100] NW will be the same for the following reason. Only the oxidation process depends on crystal orientations. The crystal faces of [110]- and [100]-NW surfaces are shown in Fig. 3.1(d). The top faces for the [110] and [100] NWs are identical and are oxidized equally. On the other hand, the side faces are different, but they are probably oxidized similarly because the oxidation rates of {110} and {111} are almost the same [1,2,3].

The band gaps of <100> and <110> NWs are predicted as $E_{g,<100>} > E_{g,<110>}$ based on theoretical calculations (Fig. 1.11). $V_{th,e} - V_{th,h}$ for [110] may be slightly smaller than that for [100] around W_P = 22 nm, but the difference was within the range of experimental dispersion. It is reasonable that the $g_{m,0}$ and $\mu_{0,h}/\mu_{0,e}$ of [110]-MOSFETs with a triangular or trapezoidal NW ($W_P > 26$ nm) agrees with that of [100]-MOSFETs with the same NW shape, because the bulk mobility on {110}/<001> and {111} is almost the same for both electrons and holes (Fig. 3.17(a)). Since the anisotropy of the effective mass between [100] and [110] NWs is predicted to be large, especially for holes, based on the theoretical calculations (Fig. 1.12), anisotropy should emerge for $g_{m,0}$ and $\mu_{0,h}/\mu_{0,e}$ for $W_P < 26$ nm (volume inversion condition), which is inconsistent with the actual results.

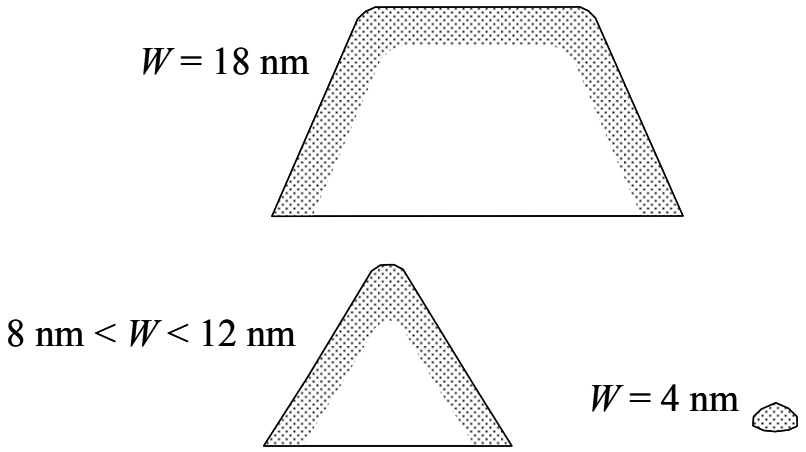

Fig. 3.18 Illustration of the confinement conditions of carriers by the cross-sectional view perpendicular to the NW. The solid line shows the interface of the Si NW. Carriers are distributed in the dot-pattern areas.

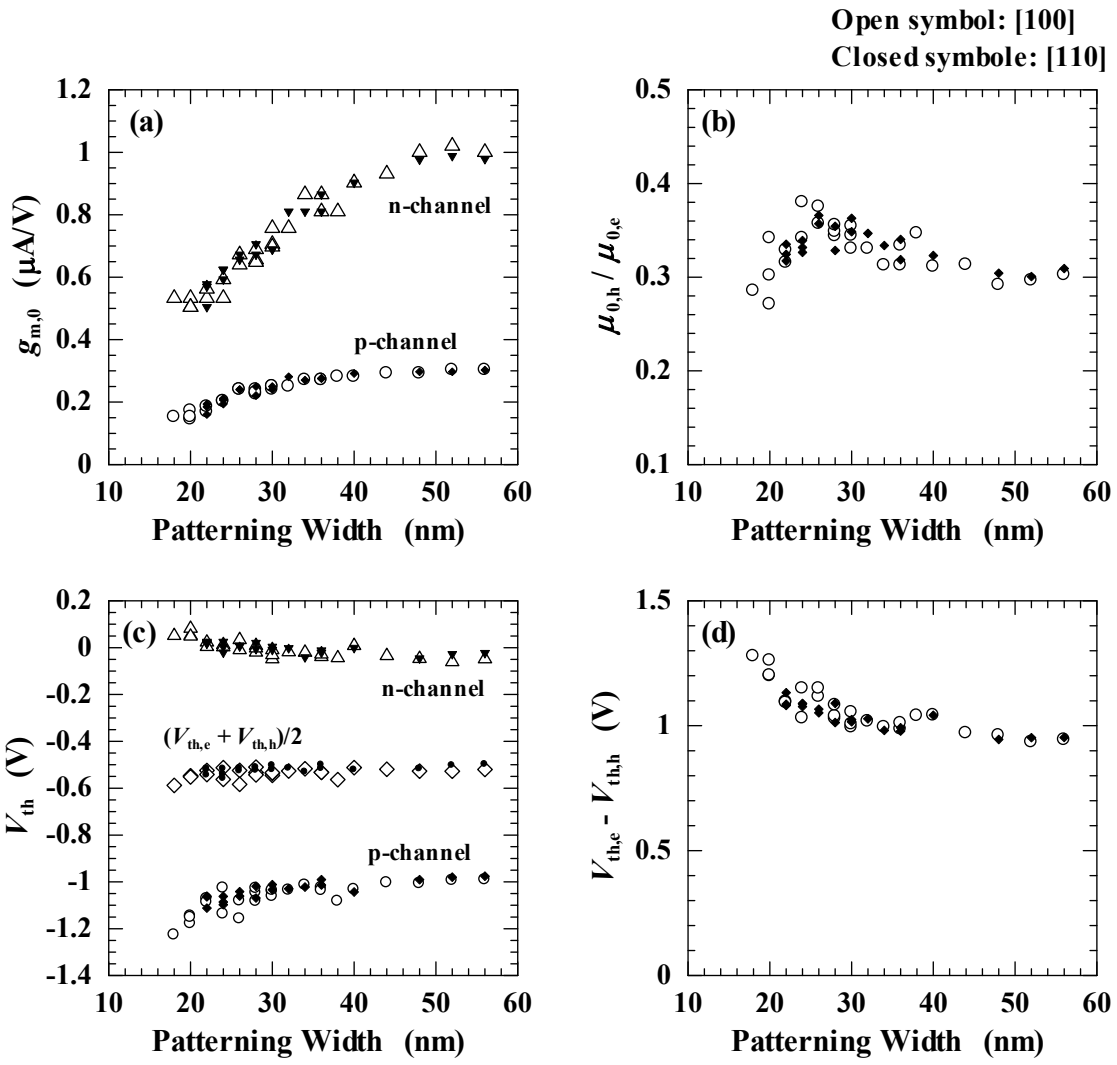

Fig. 3.19 The patterning width (W_P) dependence of (a) the $g_{m,0}$, (b) the $\mu_{0,h}/\mu_{0,e}$, (c) the V_{th}, and (d) the $V_{th,e}-V_{th,h}$ of the [110]- and [100]-NW MOSFETs ("measured devices").

3.5 Summary

Si-NW MOSFETs, whose cross-sectional size (W) of NW was changed from 18 nm to 4 nm, were characterized. Both n- and p-channel MOSFETs showed good gate control with a nearly ideal subthreshold swing of 63mV/decade. Considering threshold voltage (V_{th}) and subthreshold swing (S), the charges in the Gate-SiO_2 and the interface states were negligible. The V_{th} shift was observed and can be explained by the band-edge shift by the quantum confinement effect. Mobility (μ_0) was evaluated from the gate characteristics (I_D-V_G) using gate-insulator capacitance (C_{OX}) calculated from the cross-sectional structure measured by TEM. The W dependence of the ratio of the electron and hole mobility ($\mu_{0,h}/\mu_{0,e}$) indicated two types of carrier conditions: electric-field-confinement and volume-inversion. Under the electric-field-confinement condition (W > 7 nm), the mobility was explained by the combination of bulk-MOSFET mobility with different channel faces. Under the volume-inversion condition (W < 7 nm), μ_0 decreased, and the decrease probably originates in the increase of the surface-roughness scattering. The $\mu_{0,h}/\mu_{0,e}$ ratio decreased remarkably, which may originate in the unique band structure of NW. [100]- and [110]-NW MOSFETs were characterized and no anisotropic characteristics were observed, which is inconsistent with the theoretically-expected large differences of the hole effective mass between [100] and [110] NWs.

References

[1] J. Chen, T. Saraya, and T. Hiramoto, IEEE Electron Device Lett. **30**, 1203 (2009).

[2] J. Chen, T. Saraya, K. Miyaji, K. Shimizu, and T. Hiramoto, *Tech. Dig. of 2008 Symposium on VLSI Technol.* (2008) p. 32.

[3] X. Wu, P. C. H. Chan, S. Zhang, C. Feng, and Mansun Chan, IEEE Trans. Electron Devices **52**, 1998 (2005).

[4] S. M. Koo, A. Fujiwara, J. P. Han, E. M. Vogel, C. A. Richter, and J. E. Bonevich, Nano Lett. **4**, 2197 (2004).

[5] V. Pott, K. E. Moselund, D. Bouvet, L. D. Michielis, and A. M. Ionescu, IEEE Trans. Nanotechnology **7**, 733 (2008).

[6] T. Rudenko, V. Kilchytska, N. Collaert, M. Jurczak, A. Nazarov, and D. Flandre, IEEE Trans Electron Devices **55**, 3532 (2008).

[7] L. Sekaric, O. Gunawan, A. Majumdar, X. H. Liu, D. Weinstein, and J. W. Sleight, Appl. Phys. Lett. **95**, 023113 (2009).

[8] D. K. Schroder, *Semiconductor Material and Device Characterization, 3rd ed.* (Wiley-Interscience, Hoboken, N.J., 2006).

[9] G. Ghibaudo, Electron. Lett. **24**, 543 (1988).

[10] G. Ghibaudo, Microelectron. Eng. **39**, 31 (1997).

[11] K. Y. Fu, IEEE Electron Device Lett. **3**, 292 (1982).

[12] B. Yu, L. Wang, Y. Yuan, P. M. Asbeck, and Y. Taur, IEEE Trans. Electron Devices **55**, 2846 (2008).

[13] S. K. Chin and V. Ligatchev, IEEE Electron Device Lett. **30**, 395 (2009).

[14] S. K. Chin, V. Ligatchev, S. C. Rustagi, H. Zhao, G. S. Samudra, N. Singh, G. Q. Lo, and D. L. Kwong, IEEE Trans. Electron Devices **56**, 2312 (2009).

[15] J. Umoto, *Denjikigaku (Electromagnetism)* (Shokodo, Tokyo, 1975).

[16] L. Choi, B. H. Hong, Y. C. Jung, K. H. Cho, K. H. Yeo, D. W. Kim, G. Y. Jin, K. S. Oh, W. S. Lee, S. H. Song *et al.*, IEEE Electron Device Lett. **30**, 665 (2009).

[17] H. Majima, H. Ishikuro, and T. Hiramoto, IEEE Electron Device Lett. **21**, 396 (2000).

[18] K. Natori, IEEE Trans. Electron Devices **55**, 2877 (2008).

[19] S. M. Sze, *Semiconductor Devices: Physics and Technology* (John Wiley, New York, 2002).

[20] H. Majima, H. Ishikuro, and T. Hiramoto, IEEE Electron Device Lett. **21**, 396 (2000).

[21] M. S. Lundstrom and J. Guo, *Nanoscale Transistors: Device Physics, Modeling and Simulation* (New York, Springer, 2006).

[22] Y. Zheng, C. Rivas, R. Lake, K. Alam, T. B. Boykin, and G. Klimeck, IEEE Trans. Electron devices **52**, 1097 (2005).

[23] Y. M. Niquet, A. Lherbier, N. H. Quang, M. V. Fernández-Serra, X. Blase, and C. Delerue, Phys. Rev. B **73**, 165319 (2006).

[24] T. Vo, A. J. Williamson, and G. Galli, Phys. Rev. B **74**, 045116 (2006).

[25] S. Takagi, A. Toriumi, M. Iwase, and H. Tango, IEEE Trans. Electron Devices **41**, 2357 (1994).

[26] K. Uchida and S. Takagi, Appl. Phys. Lett. **82**, 2916 (2003).

[27] H. Irie, K. Kita, K. Kyuno and A. Toriumi, *Tech. Dig. of 2004 Int. Electron Devices Meeting* (2004) p. 225.

[28] J.-P. Colinge ed., *FinFETs and Other Multi-Gate Transistors* (Springer, New York, 2008).

[29] J.-P. Colinge, Solid-State Electron. **51**, 1153 (2007).

Chapter 4

Mobility oscillation in Si-nanowire MOSFETs

4.1 Introduction

In the nanowires (NWs), the carriers are confined in the perpendicular direction to the electrical conduction by the electric potential, and one-dimensional electronic transport is expected. The conduction and valence bands are divided into subbands, and the density of states (DOS) consists of superposition of each subband's DOS, which is proportional to $E^{-0.5}$. The DOS, therefore, shows oscillation with change of the electron energy [1, 2]. By the subband splitting, the decrease of the conductivity effective mass or intervalley scattering, both of which result in the increase of the mobility, is expected [3]. To fully utilize these effects, it is important to clarify the subband structure: band-edge energy and effective mass of each subband.

Oscillation in the drain current with the gate voltage at low drain voltage (V_{DS} = 0.2 mV) below 28 K for trigate MOSFETs with the fin width and height of 45 nm and 82 nm, respectively, has been reported [1, 4]. Similar oscillation has been also reported at higher drain voltage (V_{DS} = 50 mV) and higher temperature (≤ 137 K) for about 7 nm triangular gate-all-around MOSFETs [2]. It has been explained that the dip of the drain current is due to inter-subband scattering and to the limited increase of the electron concentration with the gate voltage, when the first subband is almost filled but the second subband is still empty. However, a quantitative analysis has not been made, and the origin of the oscillation has not been revealed yet.

In this chapter, drain-current oscillation in fabricated Si-NW MOSFETs has been characterized, and the one-dimensional carrier-transport in the Si NW has been analyzed assuming that the one-dimensional electronic states and the acoustic phonon scattering.

4.2 Experimental evidence of oscillation up to room temperature characterized by transconductance

Figure 4.1 shows the drain current (I_{DS}) versus gate voltage (V_{GS}) characteristics, and Fig. 4.2

shows the transconductance (g_m) versus gate voltage (V_{GS}) characteristics. Both figures show characteristics for the p-channel [100] Si-NW MOSFET that showed clear transconductance oscillation, where the cross-sectional shape of the NW was nearly rectangular with cross-sectional size (W, square root of cross-sectional area) of W = 6 nm (18-nm-width and 3-nm-height). The MOSFET structure and fabrication process are equivalent to that described in Chapter 3. The substrate voltage was fixed at 0 V for all the electrical measurements. In Fig. 4.2(a), temperature was changed from 101 K to 396 K, and the drain voltage was fixed at −50 mV. Figure 4.2(b) shows the normalized transconductance ($-g_m/V_{DS}$) at 101 K, where the drain voltage was changed from −10 mV to −1 V.

At the high gate voltage, the drain current increased with decrease of the temperature, indicating that the phonon scattering is dominant. Although oscillation was not clear for drain current, significant oscillation was observed for transconductance. Although the magnitude of the oscillation became smaller with increasing temperature or drain voltage, clear oscillation can be seen up to 309 K at −50 mV. The gate voltages of local maxima/minima for the transconductance showed very little change with temperature or drain-voltage change.

Figure 4.3 shows the g_m of various p-channel and n-channel Si-NW MOSFETs at 100 K and $|V_{DS}|$ = 50 mV, where two types of devices of "A" and "B" with slightly different structures and fabrication processes are shown. For the devices A, the fabrication process was not refined in comparison with that of devices B and had larger fluctuation of Si NW, which would result in the increase of surface-roughness scattering and small transconductance. Oscillation is clear for W = 4~6 nm but unclear for W = 7 nm; oscillation appears for W < about 6 nm at 100 K. Although oscillation feature varied with device, three features can be grasped. The first peak of g_m (right after turning on channel) was relatively large especially for n-channel MOSFETs. The oscillation was unclear for large gate voltage. The g_m of p-channel MOSFETs showed more oscillations than that of n-channel MOSFETs, which may originate in complex valence band structure.

The kinks of the drain current at 101 K are similar to those reported in Ref. 2, where the cross-sectional size of the NW is similar. The oscillation observed in this study may be, therefore, the same phenomenon as that in Ref. 2. It is not clear in Ref. 2 whether the oscillational characteristics were observed at room temperature because the transconductance is not shown. The oscillational characteristics may be very small at room temperature and can be only observed in the transconductance. Measurements under reduced-noise condition have enabled to observe oscillational characteristics even at room temperature.

4.3 Model of carrier transport in Si nanowires having one-dimensional density of states

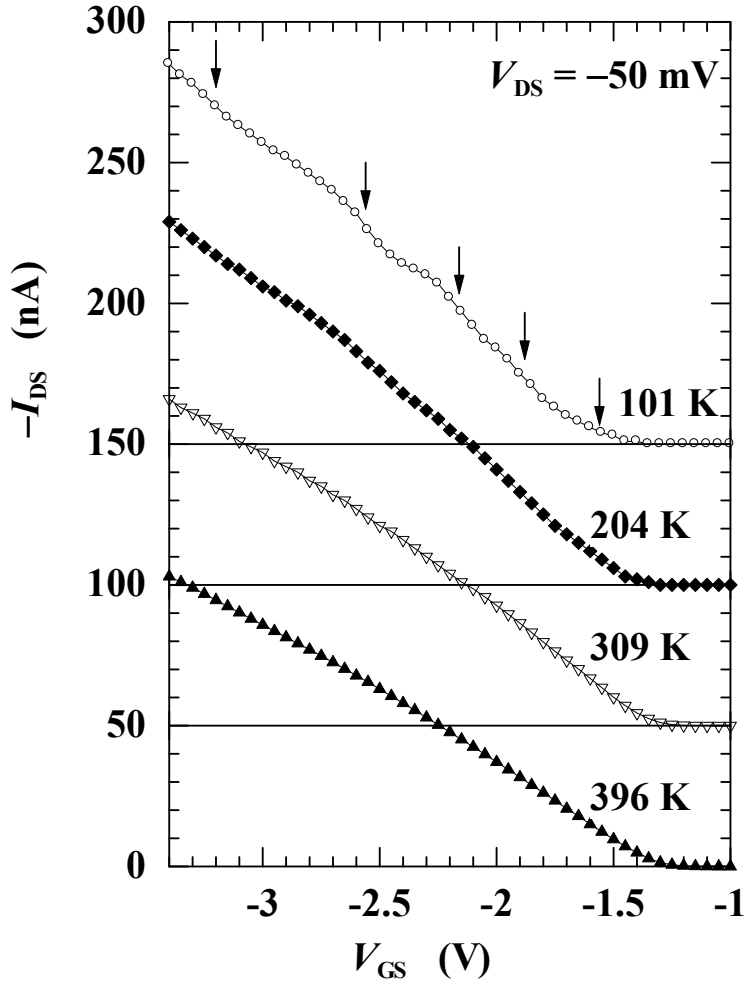

Fig. 4.1 Gate characteristics of the Si-NW MOSFET with W = 6 nm that showed clear transconductance-oscillation. The temperature was changed from 101 K to 396 K, and the drain voltage was fixed at −50 mV. The drain currents are shift by 50 nA for every measured temperature. The arrows show peaks of the slope.

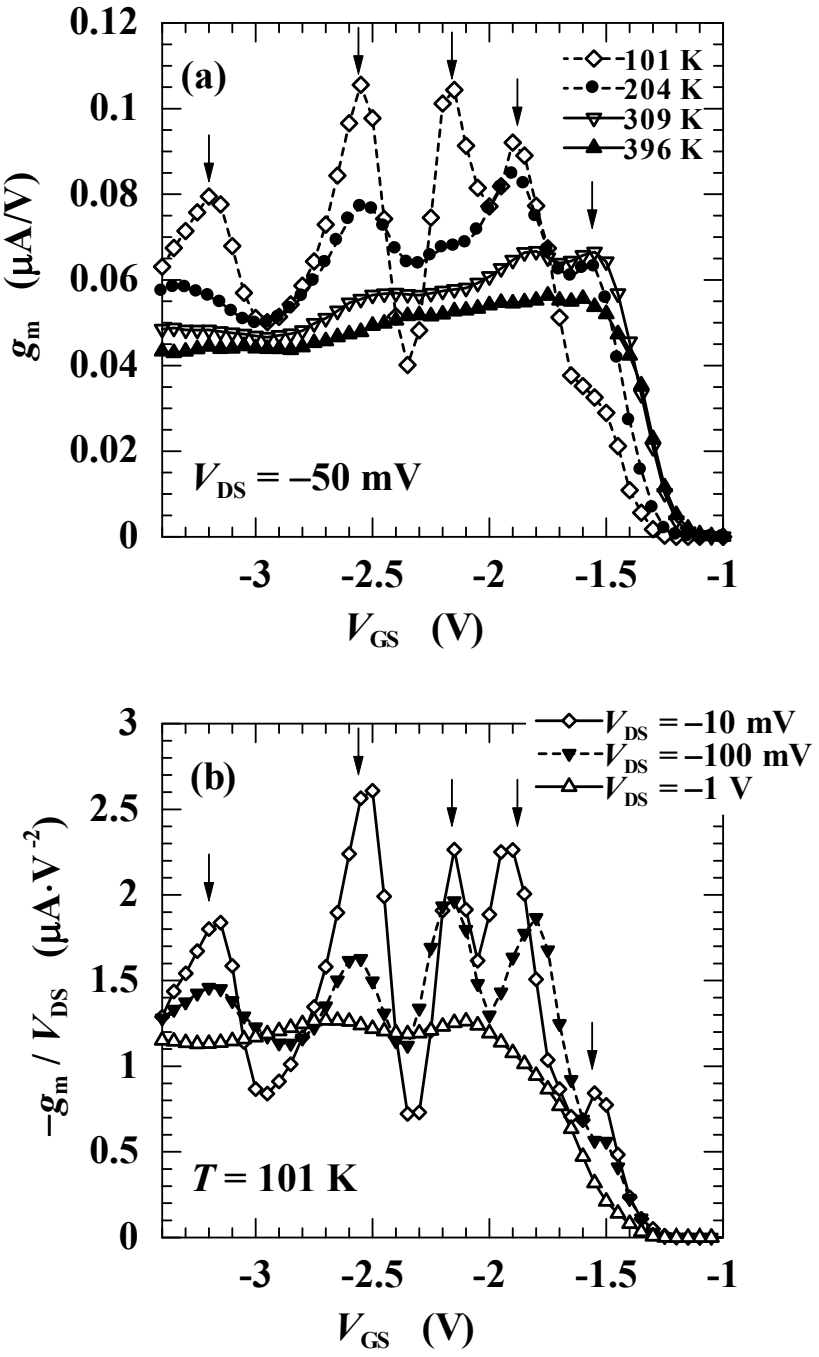

Fig. 4.2 (a) Gate voltage dependence of transconductance g_m of the same Si-NW MOSFET as shown in Fig. 4.1, where the temperature was changed from 101 K to 396 K, and the drain voltage was fixed at −50 mV. The arrows show peaks of oscillation. (b) Gate voltage dependence of normalized transconductance g_m at 101 K. The drain voltage was changed from −10 mV to −1 V.

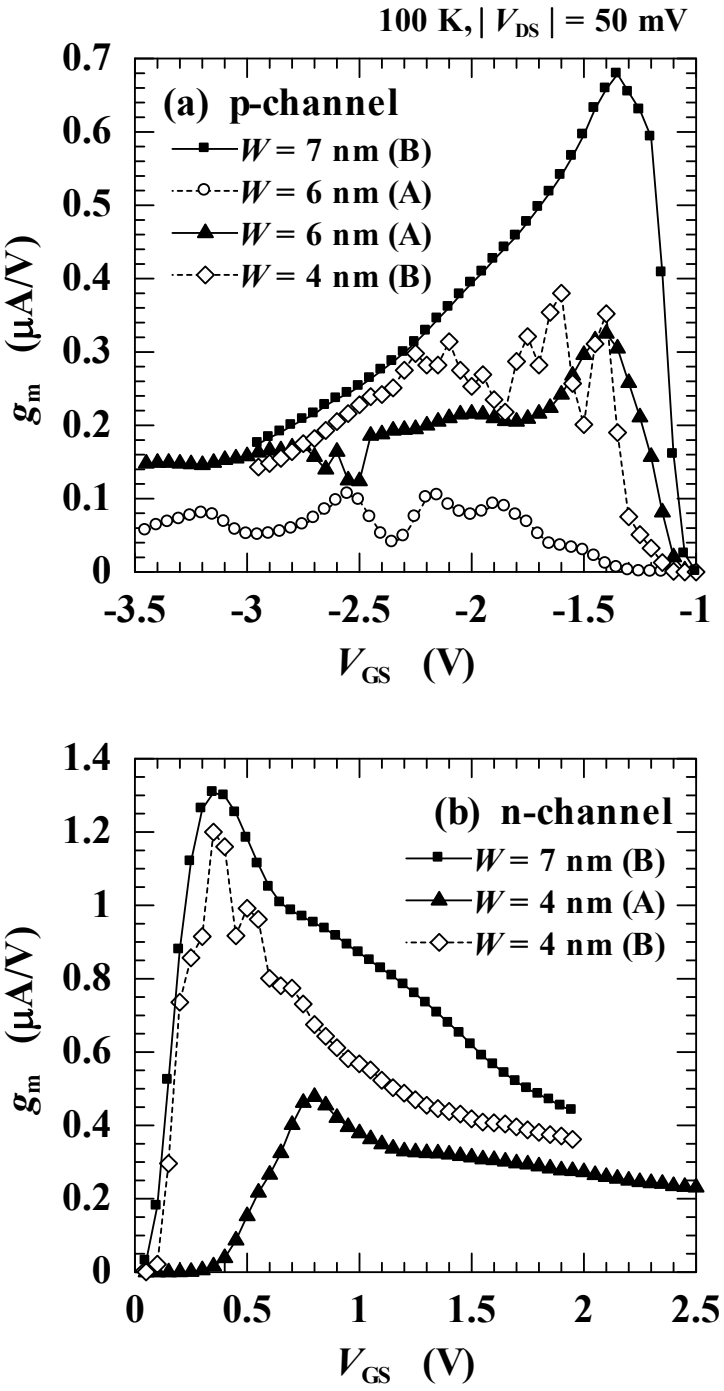

Fig. 4.3 Gate voltage dependence of transconductance g_m of various (a) p-channel and (b) n-channel Si-NW MOSFETs at 100 K and $|V_{DS}|$ = 50 mV, where two types of devices of "A" and "B" with slightly different structures and fabrication processes are shown.

4.3.1 Detail of the model

To explain the oscillation of the drain current or transconductance, a theoretical model for the carrier transport in the Si-NW MOSFETs is proposed in this section. The mobility is determined by carrier scattering, assuming the carriers to be confined in a one-dimensional NW. Then to obtain the transconductance, the dependence of the carrier concentration and mobility on the gate voltage is calculated. Although the model about hole transport is presented to compare with clear oscillation observed for p-channel MOSFETs, the model can also be applied to the electron transport.

For simplicity, the mobility determined by the longitudinal acoustic phonon scattering is considered, and it is assumed that the phonon states in the NW are the same as those in bulk [5]. The displacement of atoms at the position $\boldsymbol{r}$ is given by [6]

$$\boldsymbol{u} = \sum_{\boldsymbol{\beta}} \sqrt{\frac{\hbar}{2\rho\Omega\omega_{\boldsymbol{\beta}}}}\boldsymbol{e}_{\boldsymbol{\beta}}\left(a_{\boldsymbol{\beta}} \exp(i\boldsymbol{\beta}\cdot\boldsymbol{r}) + a_{\boldsymbol{\beta}}{}^{\dagger} \exp(-i\boldsymbol{\beta}\cdot\boldsymbol{r})\right) \tag{4.1}$$

and the scattering potential by [7]

$$U = D_{\mathrm{A}} \frac{\partial}{\partial \boldsymbol{r}} \cdot \boldsymbol{u}\,, \tag{4.2}$$

where ρ (2.33×10^3 kg/m^3) is the mass density of Si lattice, Ω is the bulk volume, $\boldsymbol{\beta}$ is the wave number vector of phonons, $\omega_{\boldsymbol{\beta}}$ is the angular frequency of phonons, $\boldsymbol{e}_{\boldsymbol{\beta}}$ is the unit vector which is parallel to $\boldsymbol{u}$, $a_{\boldsymbol{\beta}}$ and $a_{\boldsymbol{\beta}}{}^{\dagger}$ are the creation and annihilation operators of phonons, respectively, and D_{A} (5.0 eV for holes) is the acoustic deformation potential [8].

It is assumed that the NW is rectangular in the cross section. The crystalline orientations and the coordinate axes are set as shown in Fig. 4.4. The Schrödinger equation with the effective mass approximation is used to describe the wave function in the NW. The infinite quantum well of width W_y and W_z in the y- and z-directions, respectively, and infinitely large width W_x in the x-direction are assumed. For the holes, two valence-band-maxima, whose constant energy surfaces in the momentum space are approximated as the spheres with the heavy-hole effective mass m^*_{H} (0.49 m_0) and with the light-hole effective mass m^*_{L} (0.16 m_0), are considered (m_0 is the electron mass). For simplicity, the scattering between the heavy-hole and light-hole bands is ignored. The solution of the Schrödinger equation is given by

$$\psi_{\boldsymbol{k}} = \frac{1}{\sqrt{W_x}}\exp(ik_x x)\sqrt{\frac{2}{W_y}}\sin(k_y y)\sqrt{\frac{2}{W_z}}\sin(k_z z)\,, \tag{4.3}$$

$$E_{\boldsymbol{k}} = E_{k_x} + E_{k_y} + E_{k_z}\,, \tag{4.4}$$

where

$$E_{k_l} \equiv -\frac{\hbar^2 {k_l}^2}{2m^*_l}\,, \tag{4.5}$$

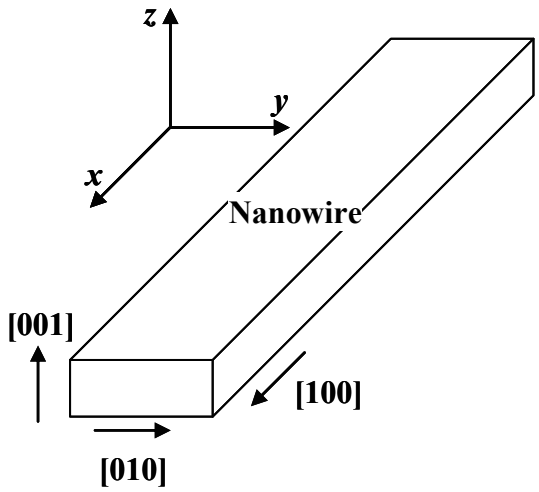

Fig. 4.4 Shape and crystalline orientations of the NW and the coordinate axes for calculation. The NW is rectangular in cross section.

$$k_x = \frac{2\pi n_x}{W_x} \ (n_x = 0, \pm 1, \pm 2, ...), \tag{4.6}$$

$$k_j = \frac{\pi n_j}{W_j} \ (n_j = 1, 2, ...), \tag{4.7}$$

for $l = x, y, z$ and $j = y, z$, where m^*_l is the effective mass and the energy of the valence-band maxima of bulk is fixed at zero. The DOS is given by

$$g(E) = \sum_{k_y, k_z} g_{k_y, k_z}(E) \tag{4.8}$$

as the sum of the one-dimensional DOSs of subbands labeled k_y, k_z

$$g_{k_y, k_z}(E) = \frac{1}{W_y W_z} \frac{1}{\pi\hbar} \sqrt{\frac{2m^*_x}{-E + E_{k_y} + E_{k_z}}}. \tag{4.9}$$

The none-zero matrix elements of the scattering potential between the states $\boldsymbol{k}$' and $\boldsymbol{k}$ are obtained from Eq. (4.2) and (4.3) by [7]

$$M(\boldsymbol{k}', \boldsymbol{k}, \pm \boldsymbol{\beta}) \equiv \left\langle \boldsymbol{k}'; N_{\boldsymbol{\beta}_1}, N_{\boldsymbol{\beta}_2}, ..., N_{\boldsymbol{\beta}} \mp 1, ... \middle| U \middle| \boldsymbol{k}; N_{\boldsymbol{\beta}_1}, N_{\boldsymbol{\beta}_2}, ..., N_{\boldsymbol{\beta}}, ... \right\rangle$$

$$= \sqrt{\frac{\hbar}{2\rho\Omega\omega_{\boldsymbol{\beta}}}} D_{\mathrm{A}}(\pm|\boldsymbol{\beta}|i) \sqrt{N_{\boldsymbol{\beta}} + 1/2 \mp 1/2} \, I_{k_y', k_y}(\beta_y) I_{k_z', k_z}(\beta_z), \tag{4.10}$$

where

$$k_x' = k_x \pm \beta_x \ \text{(momentum conservation)}, \tag{4.11}$$

$$I_{k_j', k_j}(\beta_j) \equiv \int_0^{W_j} \frac{2}{W_j} \sin(k_j' j) \sin(k_j j) \exp(\pm i\beta_j j) dj \tag{4.12}$$

for j=y, z. Here, the upper/lower of the double sign corresponds to absorption/emission of one phonon of the state $\boldsymbol{\beta}$, and $N_{\boldsymbol{\beta}}$ is the number of phonons of the state $\boldsymbol{\beta}$. The transition rate from the state $\boldsymbol{k}$ to $\boldsymbol{k}$' by the absorption/emission of the phonon $\boldsymbol{\beta}$ is given from the Fermi's Golden Rule and Eq. (4.10) [7]:

$$S(\boldsymbol{k}', \boldsymbol{k}, \pm \boldsymbol{\beta}) = \frac{2\pi}{\hbar} \left| M(\boldsymbol{k}', \boldsymbol{k}, \pm \boldsymbol{\beta}) \right|^2 \delta(E_{\boldsymbol{k}'} - E_{\boldsymbol{k}} \mp \hbar\omega_{\boldsymbol{\beta}}). \tag{4.13}$$

The inverse of the relaxation time of the state $\boldsymbol{k}$ is given by summing the transition rate over all the final states, using the relaxation time approximation assuming that the phonon scattering is elastic and isotropic [7]:

$$1/\tau(\boldsymbol{k}) = \sum_{\boldsymbol{k}', //} \sum_{\pm} \sum_{\beta_y, \beta_z} S(\boldsymbol{k}', \boldsymbol{k}, \pm \boldsymbol{\beta}), \tag{4.14}$$

where the summation over "±" represents the sum of the absorption and emission, and "$\boldsymbol{k}$', //" represents the sum over the states $\boldsymbol{k}$' whose spin is parallel to that of the initial state $\boldsymbol{k}$. Furthermore, the following approximations were used to work out Eq. (4.14).

$$N_{\boldsymbol{\beta}} + 1/2 \mp 1/2 = \frac{1}{\exp\left(\hbar\omega_{\beta} / kT\right) - 1} + 1/2 \mp 1/2 \approx \frac{kT}{\hbar\omega_{\boldsymbol{\beta}}}, \tag{4.15}$$

$$E_{\boldsymbol{k}'} - E_{\boldsymbol{k}} \mp \hbar\omega_{\boldsymbol{\beta}} \approx E_{\boldsymbol{k}'} - E_{\boldsymbol{k}}, \tag{4.16}$$

$$\omega_{\boldsymbol{\beta}} \approx v_{\mathrm{P}}\beta, \tag{4.17}$$

where v_{P} is the velocity of the longitudinal acoustic phonon (9.04×10^3 m/s [7, 8]). Equation (4.14) then results in [7]

$$1/\tau(\boldsymbol{k}) = C \sum_{k_y', k_z'} g_{k_y', k_z'}(E)(1 + 1/2\delta_{k_y', k_y})(1 + 1/2\delta_{k_z', k_z}), \tag{4.18}$$

where

$$C \equiv \frac{\pi D_{\mathrm{A}}{}^2 kT}{\hbar v_{\mathrm{P}}{}^2 \rho}. \tag{4.19}$$

To determine $1/\tau(\boldsymbol{k})$ as a function of the energy E, we assumed the Kronecker's δ to be unity in Eq. (4.18). Then, Eq. (4.18) can be simplified to

$$1/\tau(\boldsymbol{k}) \approx 1/\tau(E) \equiv C \sum_{k_y', k_z'} g_{k_y', k_z'}(E) \cdot \frac{9}{4}. \tag{4.20}$$

Although this approximation overestimates the contribution to $1/\tau(\boldsymbol{k})$ by the inter-subband scattering, it may by reasonable for small NWs, in which the subband splitting is so large that the DOSs of the subbands hardly overlap with each other.

The carrier concentration in the NW is given by

$$p(E_{\mathrm{F}}) = \frac{1}{W_x W_y W_z} \sum_{\boldsymbol{k}} f = \int_{-\infty}^{0} g(E) f dE, \tag{4.21}$$

as a function of the Fermi level E_{F}, where f is the Fermi distribution function expressed by

$$f = \frac{1}{1 + e^{(-E + E_{\mathrm{F}})/kT}}. \tag{4.22}$$

The average relaxation time for the energy E is given from the Boltzmann's transport equation as [7]

$$< \tau > (E_{\mathrm{F}}) = \frac{\sum_{\boldsymbol{k}} \frac{2E_{k_x}}{kT} \tau(E) f(1 - f)}{\sum_{\boldsymbol{k}} f}$$

$$= \frac{\sum_{k_y, k_z} \int_{-\infty}^{0} g_{k_y, k_z}(E) \frac{2(-E + E_{k_y} + E_{k_z})}{kT} \tau(E) f(1 - f) dE}{p(E_{\mathrm{F}})}, \tag{4.23}$$

and the mobility can be calculated by

$$\mu(E_{\mathrm{F}}) = \frac{e < \tau > (E_{\mathrm{F}})}{m^*_x}. \tag{4.24}$$

After determining $p(E_{\mathrm{F}})$ and $\mu(E_{\mathrm{F}})$ of the each band-maximum as a function of E_{F}, the total carrier concentration and the average mobility are obtained as follows:

$$p = \sum_m p_m \,, \tag{4.25}$$

$$\mu = \frac{1}{p}\sum_m p_m \mu_m \,, \tag{4.26}$$

where the index m labels the heavy-hole and light-hole bands.

On the other hand, the gate voltage is given by [9]

$$V_{GS} - V_{FB} = V_{OX} + \frac{1}{e}\left(E_F - E_{F0}\right), \tag{4.27}$$

where V_{FB} is the flatband voltage, E_{F0} is the Fermi level in the NW at $V_{GS} - V_{FB} = 0$, and

$$V_{OX} = -\frac{epW_yW_z}{C_{OX}} \,. \tag{4.28}$$

The gate SiO_2 capacitance C_{OX} per unit length of the NW was calculated as described in Section 3.3. In the calculation for any size of NWs in this chapter, C_{OX} was fixed at 100 pF/m. Equation (4.27) is transformed into

$$V_{GS}'(E_F) \equiv V_{GS} - V_{FB} + \frac{1}{e}E_{F0} = V_{OX} + \frac{1}{e}E_F \,. \tag{4.29}$$

Thus, $V_{GS}'(E_F)$ can be determined as a function of E_F, and the carrier concentration p and mobility μ, therefore, can be determined as a function of V_{GS}' through E_F.

4.3.2 Calculation of carrier mobility and concentration

The hole transport characteristics of the Si-NW with cross-sectional size of W = 5 nm (W_y = 9 nm and W_z = 3 nm) at 100 K were calculated using the model. Figure 4.5 shows the calculated (a) DOS $g(E)$ versus E, and (b) relaxation time $\tau(E)$ versus E and average relaxation time $\langle\tau\rangle(E_F)$ versus E_F. The relaxation time is in inverse proportion to $g(E)$ according to Eq. (4.20), and $\langle\tau\rangle(E_F)$ is almost the average of $\tau(E)$ at around $E = E_F$. The average relaxation time, then, oscillates because of the oscillation of DOS. For instance, the decrease of $\langle\tau\rangle(E_F)$ near −0.12 eV originates from the increase of DOS by the second subband, namely from the increase of both inter-subband scattering from the first to second subband and intra-subband scattering from the second to second.

Figure 4.6 shows the calculated carrier concentration p and mobility μ versus (a) E_F and (b) V_{GS}' with W = 5 nm at 100 K. Figure 4.7 shows relation between E_F and V_{GS}'. The p and V_{GS}' do not change linearly and slightly oscillate with E_F. But the p change linearly with V_{GS}', which is reasonable because slight oscillation of p-E_F relation is canceled by slight oscillation of V_{GS}'-E_F relation and p changes with V_{GS}' obeying an approximated equation

$$dV_{GS}'(E_F) \approx -\frac{eW_yW_z}{C_{OX}}dp \tag{4.30}$$

at high concentration and high temperature. On the other hand, the mobility, which is in proportion to $\langle\tau\rangle(E_F)$, shows clear oscillation with change of E_F or V_{GS}'.

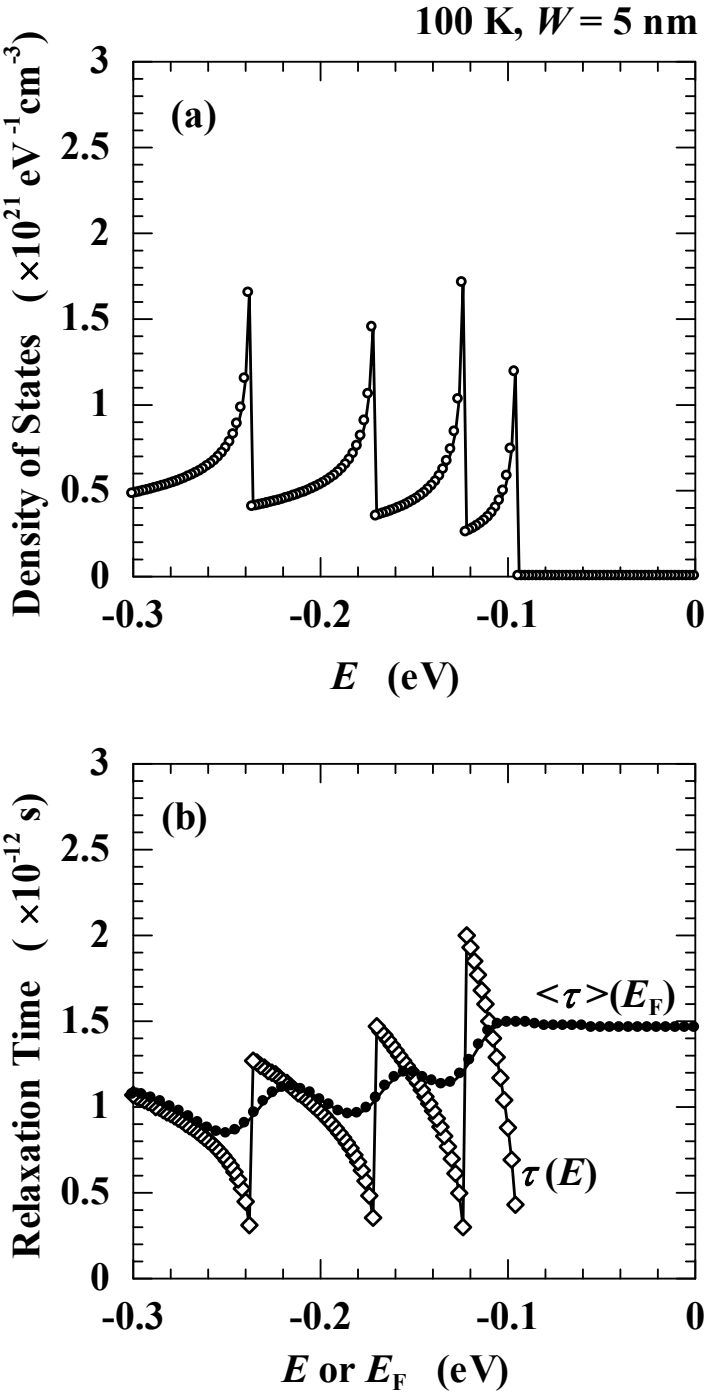

Fig. 4.5 (a) Calculated density of states $g(E)$ and (b) relaxation time $\tau(E)$ versus E and average relaxation time $<\tau>(E_F)$ versus E_F with $W = 5$ nm at 100 K.

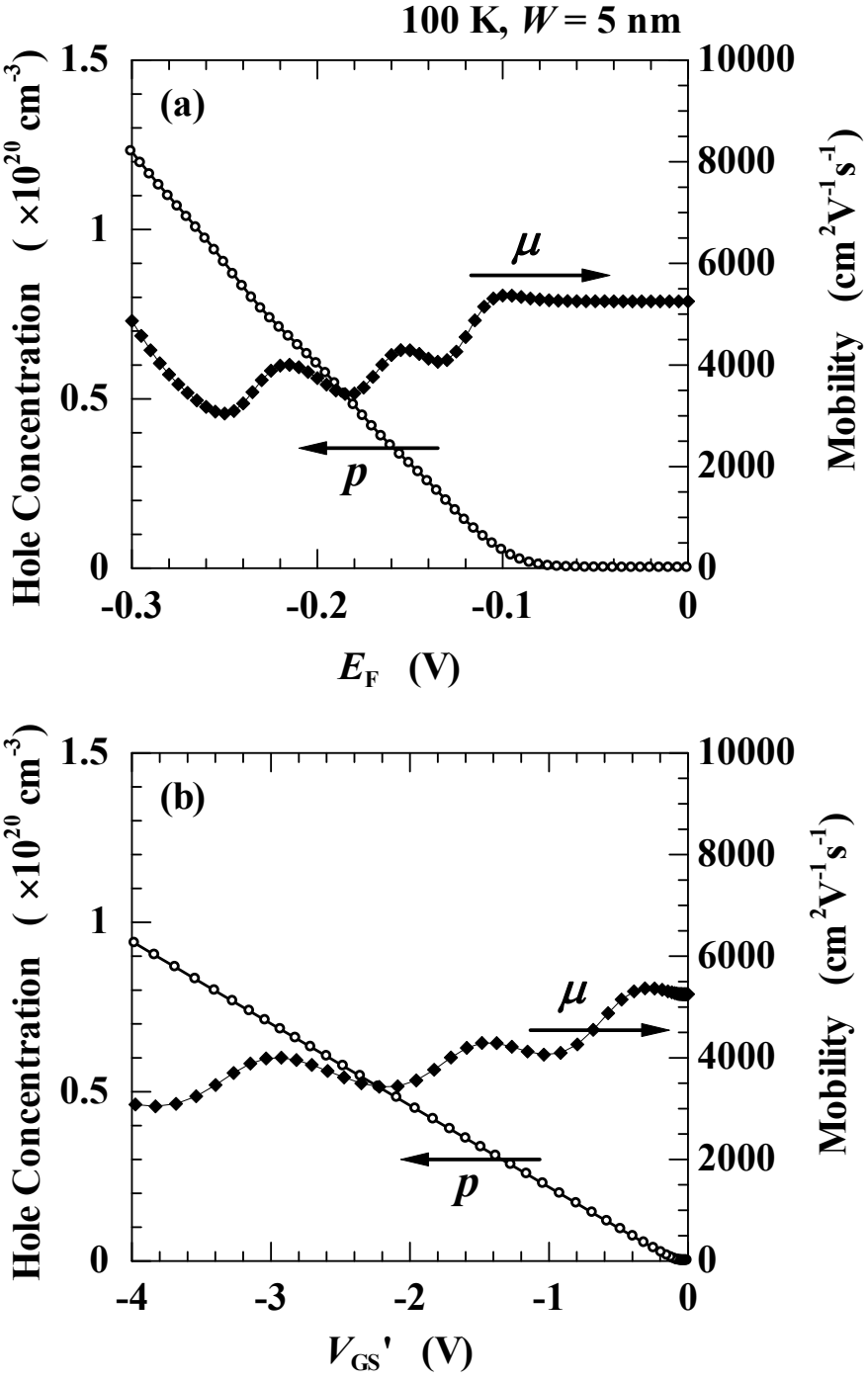

Fig. 4.6 Calculated carrier concentration p and mobility μ versus (a) E_F and (b) V_{GS}' with W = 5 nm at 100 K.

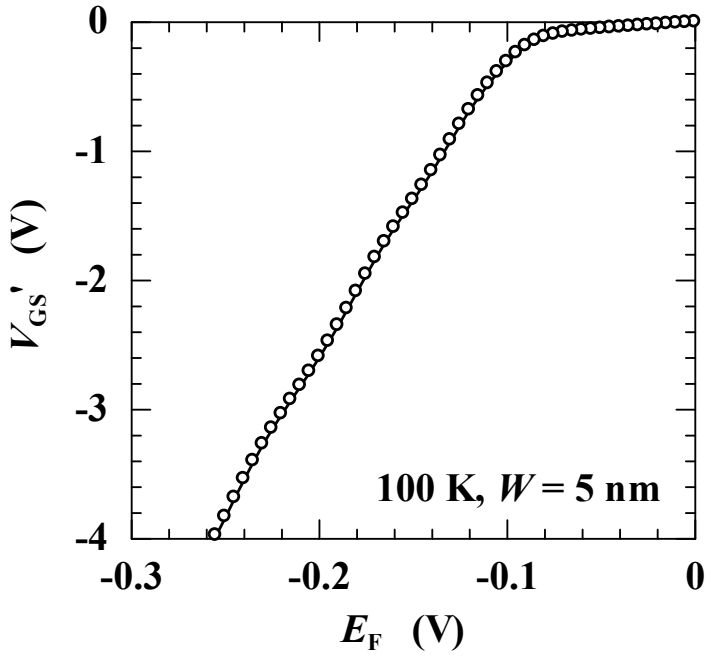

Fig. 4.7 The relation between E_F and V_{GS}' with W = 5 nm at 100 K.

Figure 4.8 shows (a) the cross-sectional size (W) and (b) the temperature dependence of the calculated transconductance (g_m) plotted as a function of V_{GS}'. The magnitude of the oscillation increases with a decrease of temperature or cross-sectional size. Oscillation at 100 K is clear for W = 5 nm but unclear for W = 7 nm; oscillation appears for W < about 6 nm at 100 K. The peak positions of the oscillation are unchanged with temperature change.

The model shows that the transconductance oscillation originates from the periodic variations in the mobility (scattering rate) caused by one-dimensional DOS ($\propto E^{-0.5}$), and one set of peak and valley of the oscillation corresponds to one subband.

4.4 Comparison of oscillation feature between theoretical and experimental results

The calculation result that transconductance (g_m) at 100 K shows the oscillation for W < about 6 nm, agrees well with the experimental result, which indicates that the model is reasonable. The period of the oscillation in the experiment (0.2~0.4 V) at 100 K is smaller than that in the calculation (about 1.2 V). The assumption of the infinite quantum well overestimates the energy of the subband splitting, and the simplified symmetrical band structure underestimates the number of subbands. These factors may be the reason why the experimental period of the oscillation is smaller than the calculated period. Maximum/minimum ratio of the oscillation in the experiment (about 2 for W = 4~6 nm) is similar to that in the calculation (about 3 for W = 5 nm).

The absolute value of g_m in the calculation is about 100 times larger than that in the calculation, probably because the model assumes only longitudinal acoustic phonon scattering, which is a part of actual carrier scattering. However, equivalent oscillational feature will be reproduced if the carrier scattering is elastic and isotropic.

4.5 Summary

Si-NW p-channel MOSFETs, in which the cross section of the NW was a rectangular shape with W = 6 nm (height: 3 nm, width: 18 nm), showed clear transconductance-oscillation up to 309 K. The magnitude of the oscillation became larger with decreasing temperature or drain voltage. To reveal the physical origin of the oscillation, a theoretical model for the carrier transport in the Si-NW MOSFETs, assuming one-dimensional electronic states and phonon scattering, was proposed. The calculation showed that transconductance at 100 K shows the oscillation for W < about 6 nm, which

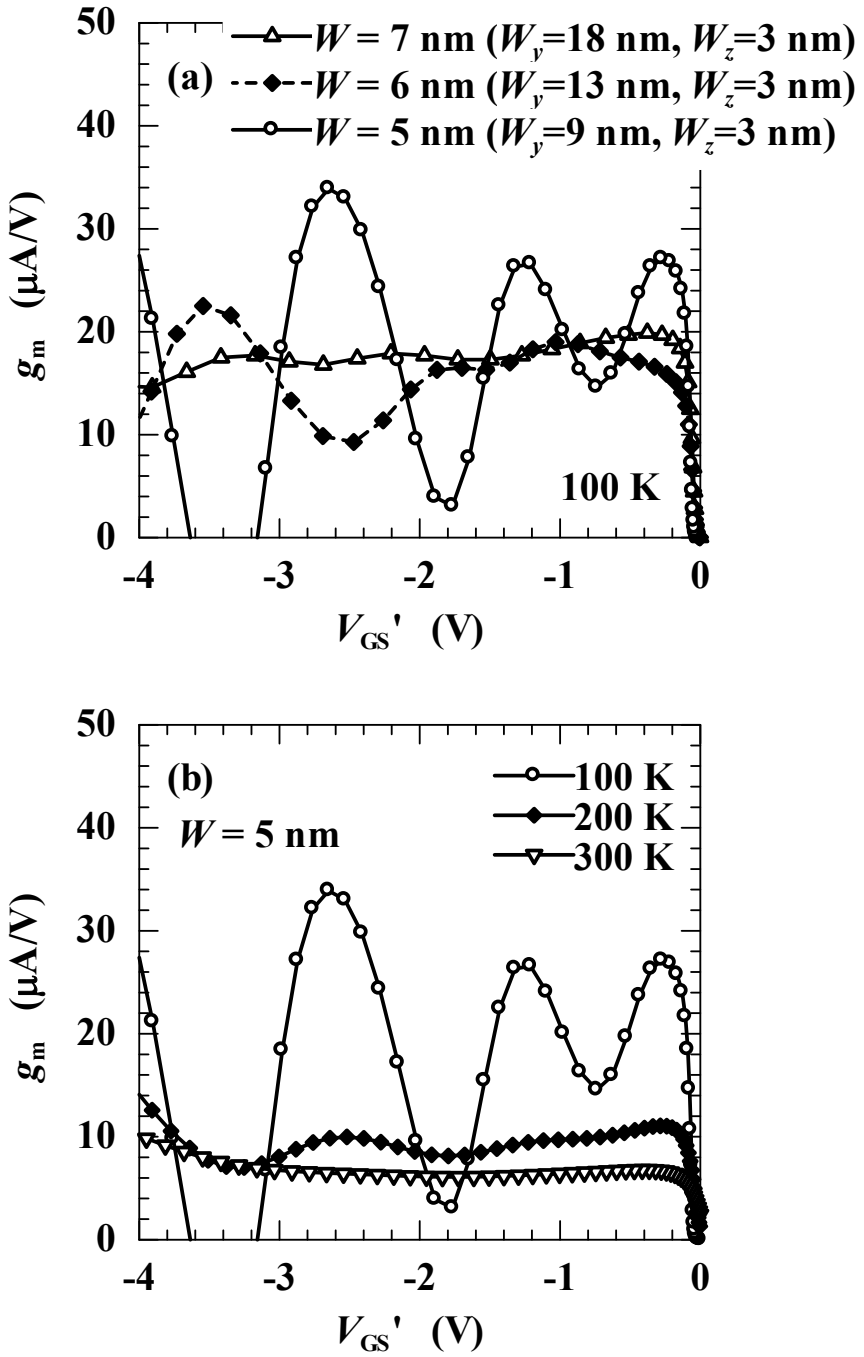

Fig. 4.8 Calculated transconductance g_m versus V_{GS}' for MOSFETs, (a) with different NW sizes at 100 K, and (b) with NW size of W = 5 nm at different temperatures.

agrees well with the experimental result. From the theoretical model, it is indicated that the oscillation originates from the periodic variations in the mobility (scattering rate) caused by one-dimensional DOS ($\propto E^{-0.5}$).

References

[1] J.-P. Colinge, A. J. Quinn, L. Floyd, G. Redmond, J. C. Alderman, W. Xiong, C. R. Cleavelin, T. Schulz, K. Schruefer, G. Knoblinger, and P. Patruno, IEEE Electron Device Lett. **27**, 120 (2006).

[2] S. C. Rustagi, N. Singh, Y. F. Lim, G. Zhang, S. Wang, G. Q. Lo, N. Balasubramanian, and D.-L. Kwong, IEEE Electron Device Lett. **28**, 909 (2007).

[3] S. Oda and D. Ferry, *Silicon Nanoelectronics* (Taylor & Francis, Boca Raton, 2006).

[4] J.-P. Colinge, Solid-State Electron. **51**, 1153 (2007).

[5] A. K. Buin, A. Verma, A. Svizhenko, and M. P. Anantram, Nano Lett. **8**, 760 (2008).

[6] C. Kittel and P. McEuen, *Introduction to Solid State Physics, 8th ed.* (J. Wiley, Hoboken, N.J., 2005).

[7] M. Lundstrom, *Fundamentals of Carrier Transport, 2nd ed.* (Cambridge University, Cambridge, 2000).

[8] J. Bardeen and W. Shockley, Phys. Rev. **80**, 72 (1950).

[9] M. S. Lundstrom and J. Guo, *Nanoscale Transistors: Device Physics, Modeling and Simulation* (Springer, New York, 2006).

Chapter 5

Electronic states and optical properties in Si-nanowires calculated by density functional theory

5.1 Introduction

Si-based light emitters have been in strong demand to merge photonics into Si-based electronics [1, 2]. Si nanostructures are promising candidates because improvement in luminous efficiency by quantum confinement effects is expected [3, 4]. However, the actual external-quantum-efficiency of the nanostructures ($\leq 10^{-2}$ [5]) remains as low as the bulk's efficiency [6, 7]. Since the factors dominating the efficiency are not only band-to-band radiative recombination but also nonradiative recombination such as transitions related to interfacial states, the nonradiative transitions may degrade the luminous efficiency in the Si nanostructures. However, it is necessary to reveal the band-to-band transition rate in the Si nanostructures.

Si nanowires (NWs) are one of the Si nanostructures and would have the unique anisotropy of luminescence. By folding the bulk Si band on the axes parallel to the wire directions, the energy bands of <100> and <111> Si wires turn to direct and indirect bandgap, respectively. This view roughly corresponds to the results of theoretical calculations for NWs with 1~2 nm diameter [8, 9]. Thus, the <100> NWs are promising for efficient light emission. However, it was predicted that the dipole matrix element of the first direct transition at the Γ point of a 2-nm-diameter <100> Si-NW is 10^{-5}~10^{-4} times smaller than that of bulk GaAs [10]. It should be noted that the band-to-band transition rate is proportional to both the dipole matrix element and the density of states (DOS). Since the band-edge DOS of one-dimensional structures ($\propto E^{-0.5}$) may be much larger than that of three-dimensional structures ($\propto E^{0.5}$), both the dipole matrix element and the DOS need to be calculated. The optical properties such as the imaginary part of the dielectric function (ε_i) or absorption coefficient (α) have also been calculated for Si NWs [11-14]. In these studies, the optical properties near the bandgap energy (E_g) are almost zero but are not revealed quantitatively.

In this study, the optical properties near the E_g of <100> and <111> Si-NWs and their dependence on NW cross-sectional size have been calculated by density functional theory.

5.2 Calculation method

The band structure, DOS, and optical properties of Si NWs oriented along either [100] or [111] were calculated by using the CASTEP code [15, 16] that employs the density functional theory (DFT), where the gradient corrected exchange-correlation functional of the Perdew-Burke-Ernzerhof functional (PBE) [17] and the norm-conserving pseudopotentials were adopted. A supercell approach, by which NWs are periodically repeated, was adopted. The cutoff energy of the plane wave was set at 200 eV.

The CASTEP code calculates the imaginary part of the dielectric function (ε_i), which is given by [18]

$$\varepsilon_i(\hbar\omega) = \frac{2e^2\pi}{\Omega\varepsilon_0}\sum_{\boldsymbol{k},v,c}\left|\left\langle\psi_{\boldsymbol{k}}^c\left|\boldsymbol{e}\cdot\boldsymbol{r}\right|\psi_{\boldsymbol{k}}^v\right\rangle\right|^2\delta(E_{\boldsymbol{k}}^c - E_{\boldsymbol{k}}^v - \hbar\omega), \tag{5.1}$$

where $\boldsymbol{r}$ is the position, $\psi_{\boldsymbol{k}}^c/\psi_{\boldsymbol{k}}^v$ and $E_{\boldsymbol{k}}^c/E_{\boldsymbol{k}}^v$ are the wave function and the energy, respectively, of a state $\boldsymbol{k}$ in the conduction/valence band, $\boldsymbol{e}$ is the unit vector defining the polarization of the incident electric field, ω is the angular frequency of the incident light, and Ω is the volume. Phonon-related transitions are not included in this calculation. The Kramers-Kronig transform is used to obtain the real part of the dielectric function (ε_r).

Since calculated structures include a different size of vacuum space between the NWs, DOS ($g(E)$) and dielectric function (ε_r, ε_i) are calculated for NWs with vacuum space. Calculated structures also include H atoms, and the number of H atoms differs with the NW size. (The Si NWs are terminated by the H atoms as discussed later.) To compare properties of these NWs, effective volume (V_{eff}) of the NWs in the unit cell is defined so that the number of electrons per unit volume in the NWs is the same as that in bulk:

$$V_{\text{eff}} \equiv \frac{N_e a^3}{32}, \tag{5.2}$$

$$N_e \equiv 4N_{\text{Si}} + N_{\text{H}}, \tag{5.3}$$

where N_e, N_{Si}, and N_{H} are the number of electrons, Si atoms, and H atoms in the unit cell, respectively, and a is the lattice constant of bulk Si. The effective DOS ($g_{\text{eff}}(E)$) and real and imaginary part of the effective dielectric function ($\varepsilon_{r,\text{eff}}$, $\varepsilon_{i,\text{eff}}$), for the NWs being densely packed, are defined as

$$g_{\text{eff}}(E) \equiv \frac{V}{V_{\text{eff}}}g(E), \tag{5.4}$$

$$\begin{aligned}\varepsilon_{r,\text{eff}} - 1 &\equiv \frac{V}{V_{\text{eff}}}(\varepsilon_r - 1)\\ \varepsilon_{i,\text{eff}} &\equiv \frac{V}{V_{\text{eff}}}\varepsilon_i\end{aligned}, \tag{5.5}$$

where V is the volume of the unit cell. The effective absorption coefficient (α_{eff}) is defined from $\varepsilon_{r,\text{eff}}$

and $\varepsilon_{i,eff}$,

$$\alpha_{eff} = \frac{\omega \varepsilon_{i,eff}}{c n_{eff}}, \tag{5.6}$$

$$n_{eff} = \sqrt{\frac{\varepsilon_{r,eff} + \sqrt{\varepsilon_{r,eff}^{\ 2} + \varepsilon_{i,eff}^{\ 2}}}{2}}. \tag{5.7}$$

The cross-sectional size of NWs (W), taking account of a square cross section and volume of one electron being $a^3/32$, is defined as

$$W = \begin{cases} \sqrt{N_e \cdot \frac{a^3}{32} \cdot \frac{1}{a}} & ([100]\,\text{nanowires}) \\ \sqrt{N_e \cdot \frac{a^3}{32} \cdot \frac{1}{\sqrt{3}a}} & ([111]\,\text{nanowires}) \end{cases}. \tag{5.8}$$

As a result of geometrical optimization, the lattice constant (a) of the bulk Si was 0.538 nm. For NWs, Si bond angles (Si-Si-Si) and distances (Si-Si) were fixed to those of the optimized geometry of the bulk Si. All dangling bonds on the surface were terminated by H atoms while maintaining the tetrahedral bond angles and the distance of Si-H bonding being 0.154 nm. Neighboring NWs were separated by at least 0.5 nm. Figure 5.1 (a) and (b) shows one of the structures of [100] and [111] Si NWs, respectively. The W of [100] and [111] Si NWs was 1.3~3.0 nm and 1.0~2.0 nm, respectively. The maximum size is limited by computer capability. The maximum size of [111] Si NWs is smaller than that of [100] Si NWs because [111] Si NWs have more atoms per unit length of NWs than [100] Si NWs with the same cross-sectional size. The cross-sectional shapes of NWs with different size are similar to those shown in Fig. 5.1. The structural properties are summarized in Table 5.1.

5.3 Results and discussion

5.3.1 Band structure

Figure 5.2 shows the bandgap energy (E_g) as a function of W, where the calculated bandgap energy for the bulk Si is also shown. The bandgap energy increases with a W decrease as a result of quantum confinement effects. This trend and the value of the bandgap are well consistent with results reported earlier [9, 13]. The bandgap energy of the [100] and [111] NWs are almost equivalent to each other.

Figures 5.3 and 5.4 show the band structures of [100] and [111] Si NWs with different sizes, respectively, where the energy of the valence-band maximum (VBM) is set at zero. The band structures of the bulk Si folded on the NW axes are also shown only for the VBM and conduction-band minimum (CBM) in Figs 5.3(d) and 5.4(d). As shown in Fig. 5.3, the [100] NWs

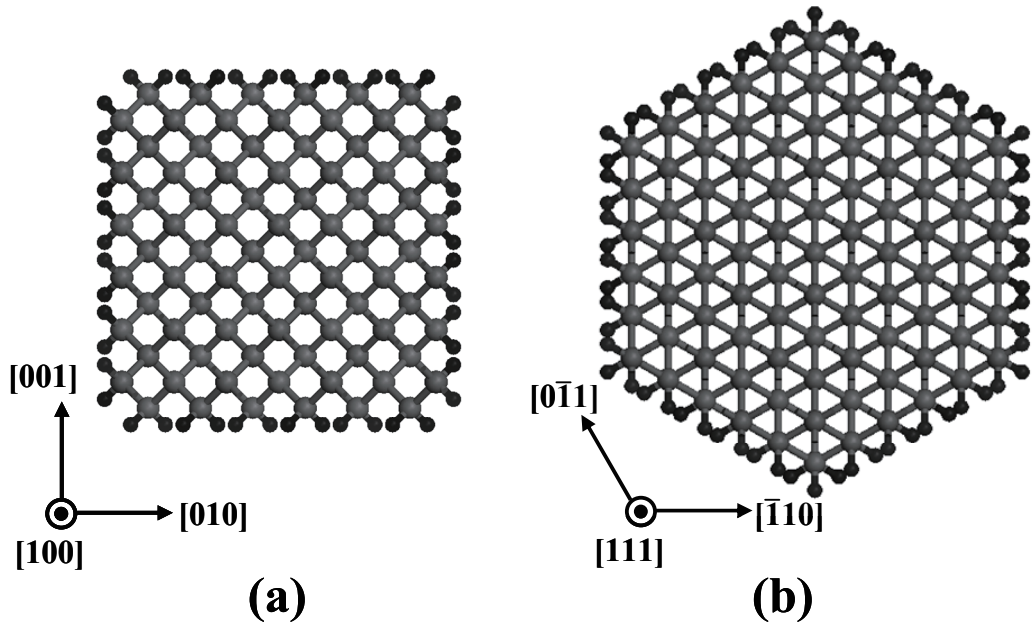

Fig. 5.1 The structure of (a) [100]-1.9nm and (b) [111]-2.0nm NW. The large and small balls stand for Si and H atoms, respectively.

Table 5.1 The cross-sectional size (W), the number of Si and H atoms, lattice vectors parallel (//) and perpendicular (⊥) to the NWs.

Label	W (nm)	Si	H	Lattice vector (//)	Lattice vectors (supercell) (⊥)
[100]-1.3nm	1.3	40	32	a[100]	4a[010], 4a[001]
[100]-1.9nm	1.9	84	48	a[100]	5a[010], 5a[001]
[100]-3.0nm	3.0	220	80	a[100]	7a[010], 7a[001]
[111]-1.0nm	1.0	38	30	a[111]	2a[$\bar{1}$10], 2a[0$\bar{1}$1]
[111]-1.3nm	1.3	74	42	a[111]	2.5a[$\bar{1}$10], 2.5a[0$\bar{1}$1]
[111]-2.0nm	2.0	182	66	a[111]	3.5a[$\bar{1}$10], 3.5a[0$\bar{1}$1]

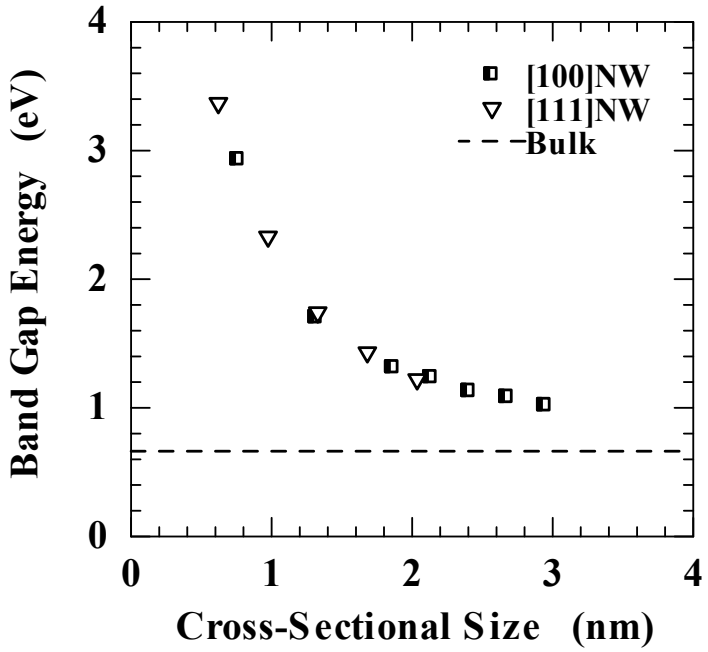

Fig. 5.2 Bandgap energy (E_g) of [100] and [111] Si NWs as a function of cross-sectional size (W). Calculated bandgap of bulk Si is also shown.

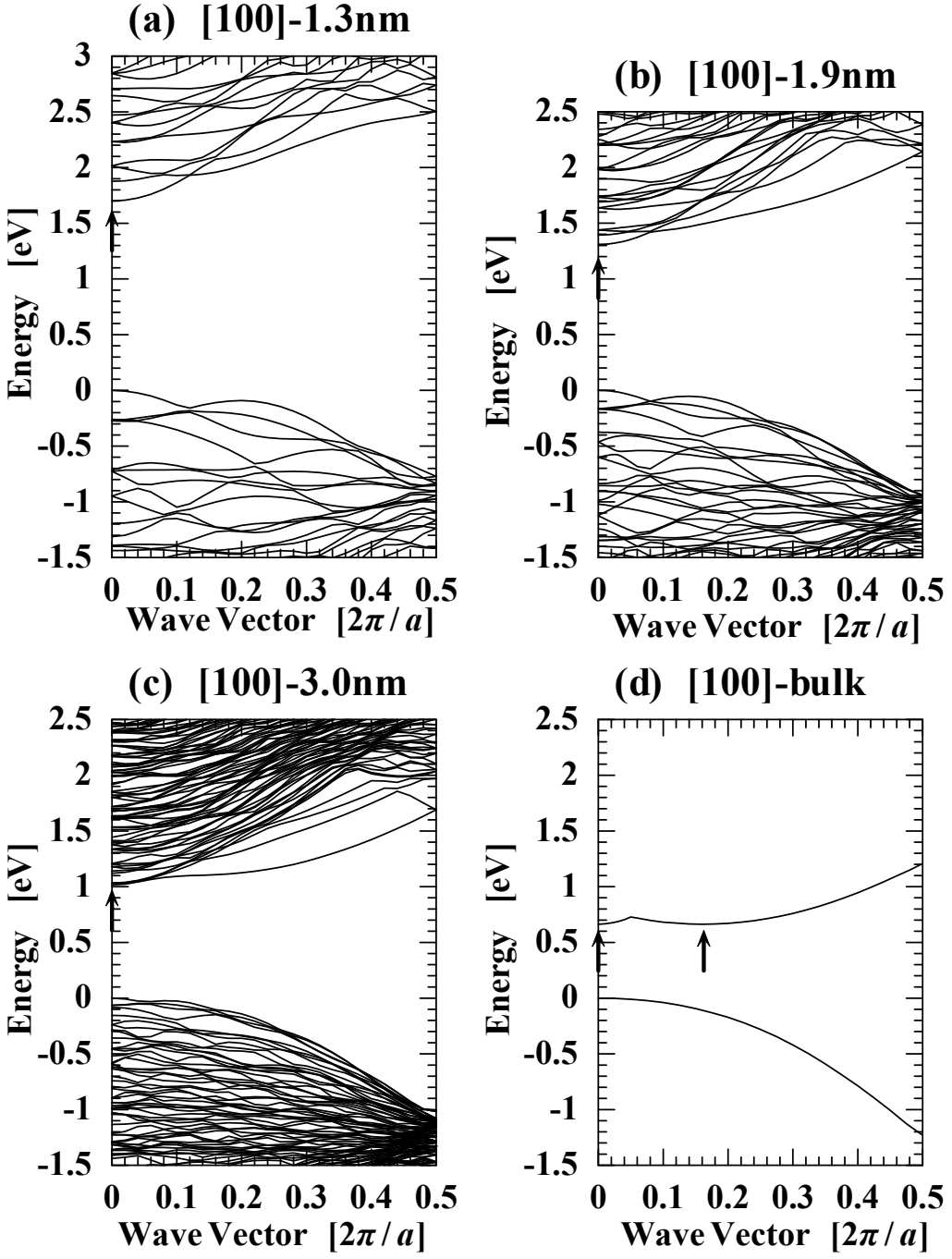

Fig. 5.3 (a)-(c) Band structures [100] Si NWs with different sizes, where the energy of the VBM is set at zero. The direction of the wave vector is parallel to the NW axis. (d) The band structures of the bulk folded on the NW axis, where only the CBM and VBM are shown. The arrows show the minimum points of conduction-band.

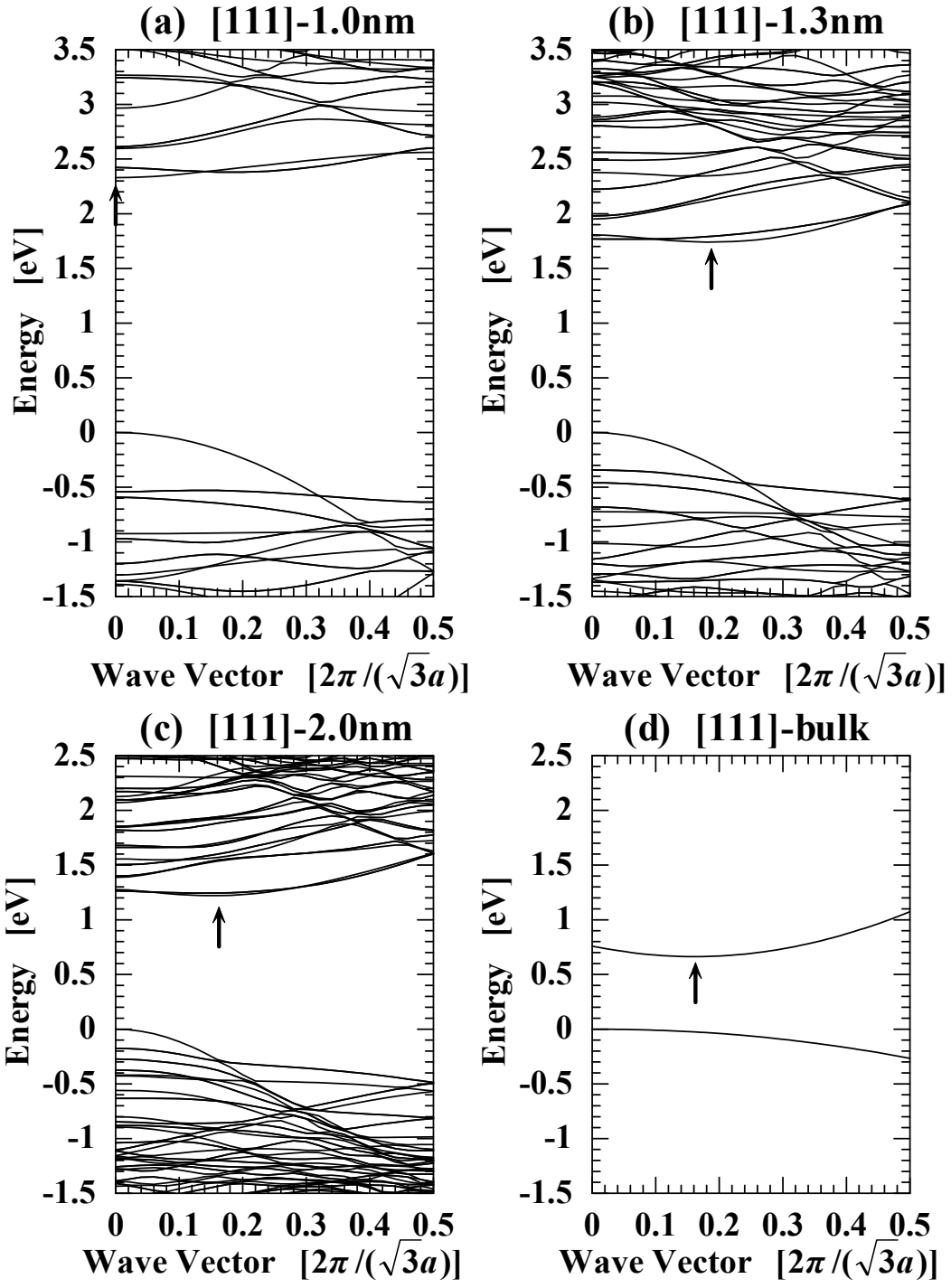

Fig. 5.4 (a)-(c) Band structures of [111] Si NWs with different sizes, where the energy of the VBM is set at zero. The direction of the wave vector is parallel to the NW axis. (d) The band structures of the bulk folded on the NW axis, where only the CVM and VBM are shown. The arrows show the minimum points of conduction-band.

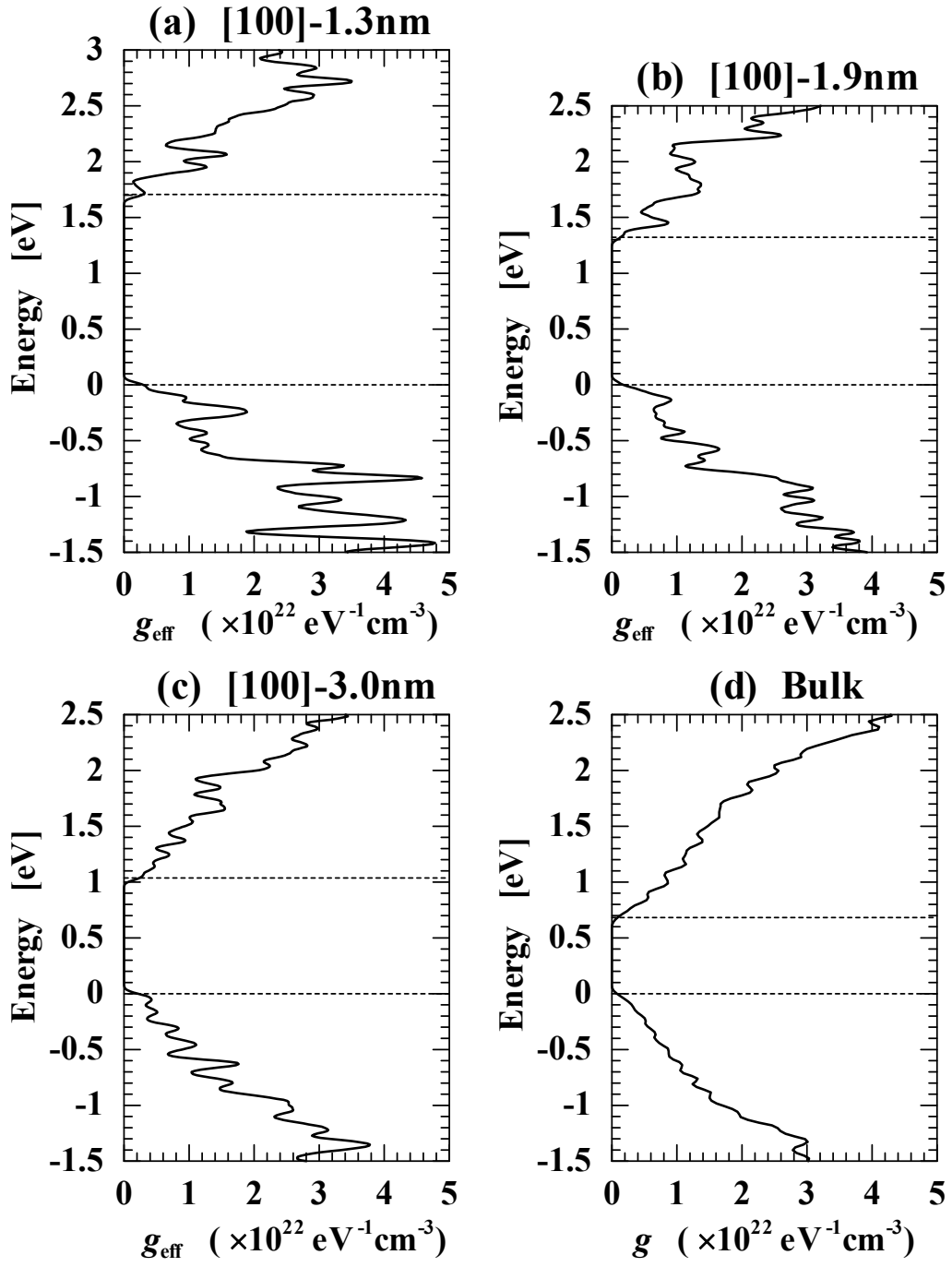

Fig. 5.5 (a)-(c) Effective DOS (g_{eff}) of [100] Si NWs with different sizes, and (d) the DOS (g) of bulk Si, where the CBM and VBM are shown as broken lines. The Gaussian broadening with 0.025 eV width was used for smearing.

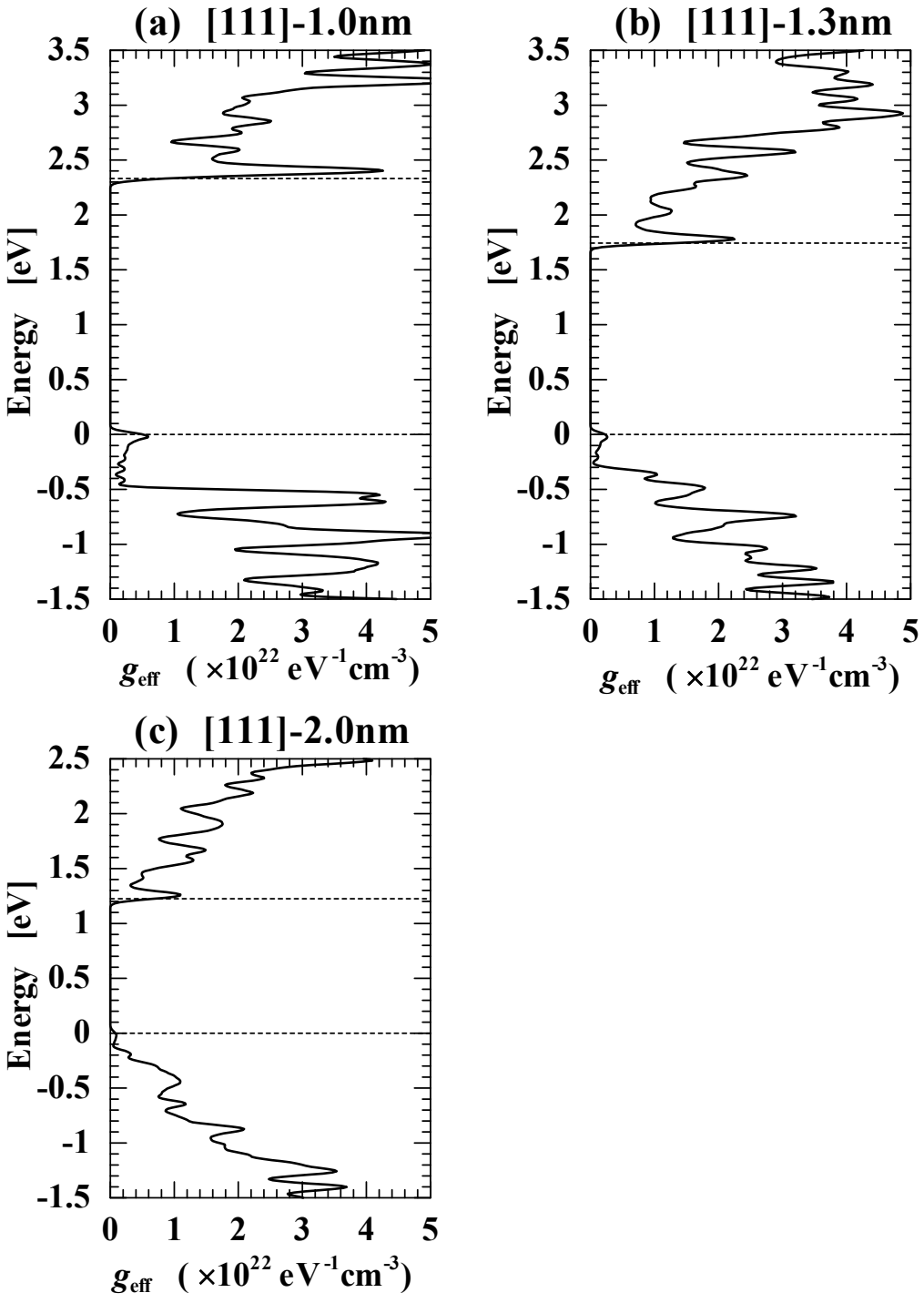

Fig. 5.6 Effective DOS (g_{eff}) of [111] Si NWs with different sizes, where the CBM and VBM are shown as broken lines. The Gaussian broadening with 0.025 eV width was used for smearing.

have the direct band structure. The [100]-bulk has two CBMs (0($2\pi/a$) and 0.15($2\pi/a$)), while the [100]-NWs has a CVM at 0($2\pi/a$). This result can be explained by effective mass approximation (Section 1.2.2) and similar result is shown in Fig. 1.9. On the other hand, the large [111] NWs ([111]-1.3nm and [111]-2.0nm) have the indirect band structure with the CBM being close to the CBM of the folded band of the bulk ($0.15\cdot 2\pi/(\sqrt{3}a)$). The [111]-1.0nm has the direct band structure, where the electronic states of the NW are much different from that of bulk. As the NW size increases, the band structures of both [100] and [111] NWs approach the folded band structures of the bulk, which means that electronic states of NWs approach that of bulk.

5.3.2 Density of states

Figures 5.5 and 5.6 show the effective DOS (g_{eff}) of [100] and [111] Si NWs, respectively, and the DOS (g) of the bulk Si is shown in Fig. 5.5(d). The Gaussian broadening with 0.025 eV width was used for smearing. The DOS of a subband in one-dimensional structures follows the one-dimensional DOS [19],

$$g(E) = \frac{1}{A}\frac{1}{\pi\hbar}\sqrt{\frac{2m^*}{E}}, \tag{5.9}$$

where m^* is the effective mass of the subband. Equation (5.9) tells that subband DOSs are in inverse proportion to the cross-sectional area. This trend is well observed for both CB and VB edges of [111] NWs, while it is not clear for the [100] NWs because of the change of subband overlap. The subbands of [100] NWs separate from each other with a W decrease. For example, the 1st to 4th bands from the CBM are located at 1.016 eV to 1.033 eV at the Γ point for [100]-3.0nm, while they are at 1.700 eV to 2.016 eV for [100]-1.3nm. The DOS of the CBM of the [111] NWs is relatively large because of the large effective mass. The DOSs of the order of 10^{21} $\text{eV}^{-1}\text{cm}^{-3}$ near the band edge are consistent with results calculated by using the one-dimensional DOS for a 5 nm×5 nm NW [20] or 3 nm×9 nm NW (Fig. 4.5(a)).

5.3.3 Absorption coefficient by band edge transition

Figures 5.7 and 5.8 show effective absorption coefficients (α_{eff}) of [100] and [111] Si NWs, respectively, and the absorption coefficient (α) of bulk Si is shown in Fig. 5.7(d). The α and α_{eff} were calculated for plane-polarized light. As long as the polarization direction is perpendicular to NW, the α_{eff} is isotropic. Then, only the two results, in which the polarization direction is parallel or perpendicular to the NW, are shown. For the bulk, the α is isotropic and one result is shown in Fig. 5.7(d). The measured α for the bulk Si [21-25] is also shown in Fig. 5.7(d). Regarding the experimental data of the bulk, the absorption starts to increase at E_g, which originates from the phonon-related indirect transitions. On the other hand, in our calculated result of the bulk, the absorption starts to increase at the gap energy at the Γ-point because the calculation does not

include phonon-related transitions. In a large energy range (E–E_g > 3.2 eV), the calculated result shows good agreement with the experimental result.

As for the [100] NWs, the α_{eff} for the parallel polarization has a peak at E_g, which originates from direct transition at the Γ point, and the peak value decreases with increase in W. The decrease in the α_{eff} peak while keeping the direct bandgap is reasonable, and this peak must vanish for infinitely large wire because the CBM at the Γ point for the infinitely large wire is only projection of the CBMs of the bulk. That is, [100] Si NWs with large cross-sectional size have much indirect nature of bulk Si, and matrix elements of direct transition are not completely zero but approach zero. Even for the thin NW of [100]-1.3nm, absorption coefficient at band edge (~10^3 cm^{-1}) is small in comparison with that of bulk GaAs (~10^4 cm^{-1}, Fig. 1.7), which indicates that indirect nature of bulk Si still remains in the NW.

The α_{eff} value near E_g for [100]-1.9nm is larger than that of the experimental results of the bulk, while the α_{eff} for [100]-3.0nm is comparable to the bulk. Therefore, it is expected that the luminous efficiency of [100] NWs for $W \leq 1.9$ nm is improved compared with that of the bulk and increases remarkably with decrease in NW size.

Concerning the [111] NWs, the α_{eff} for the parallel polarization starts to increase at E_g for [111]-1.0nm and at the energy slightly higher than E_g for the NWs with the indirect bandgap ([111]-1.3nm and [111]-2.0nm). These increases originate from direct transition at the Γ point and the α_{eff} value decrease with increase in W. The [111] NWs have smaller α_{eff} value than the [100] NWs at a given W. For example, the α_{eff} of [111]-1.3nm is about ten times smaller than that of [100]-1.3nm in spite of close W. In consideration of the indirect nature and the small α_{eff} value, [111] NWs are less attractive than [100] NWs from the standpoint of luminous efficiency.

Absorption coefficient oscillates with energy and the magnitude of the oscillation becomes larger with a W decrease, which originates in oscillational DOS.

5.3.4 Forbidden transition

The absorption edge for the perpendicular polarization of [100]-1.3nm, [100]-1.9nm, and [111]-1.0nm clearly shifts to the higher energy side than the bandgap energy as shown in Figs. 5.7 and 5.8.

The space group of calculated [100] and [111] NWs was No. 95 (D_4^7, $P4_322$) and No. 164 (D_{3d}^3, $P\bar{3}m1$), respectively. The symmetry operations, character tables, and direct product tables of the space group No. 95 and No. 164 are summarized in Table 5.2, 5.3, and 5.4, respectively. The allowed transitions at the Γ point for [100] and [111] NWs for plane-polarized light with the polarization direction being parallel (//) and perpendicular (⊥) to the NW derived from Tables 5.3-5.4 are summarized in Table 5.5. From Table 5.5, the transitions between singly degenerate states are the forbidden transitions at the Γ point for the perpendicular polarization for both the

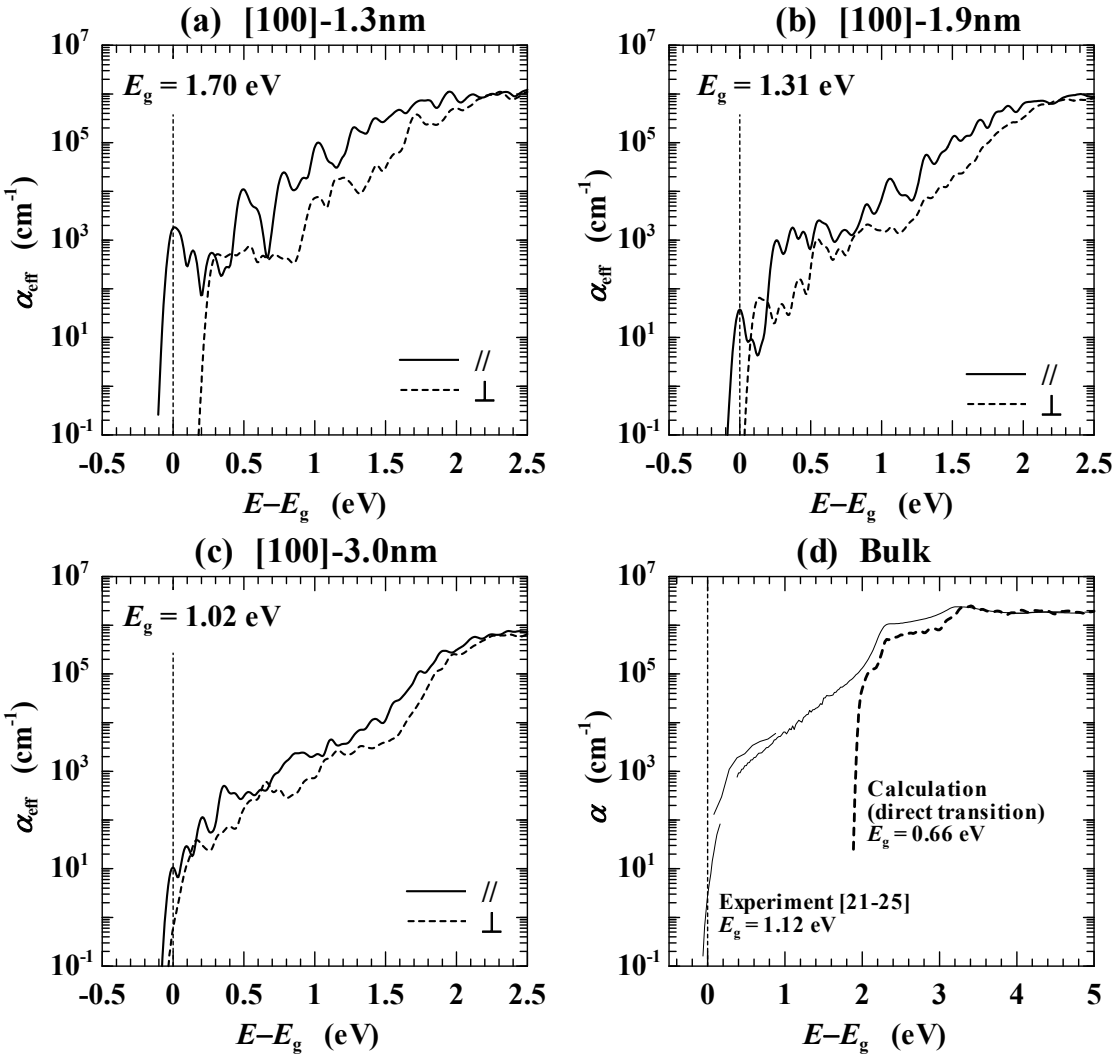

Fig. 5.7 (a)-(c) Effective absorption coefficients (α_{eff}) of [100] Si NWs with different sizes, and (d) absorption coefficient (α) of bulk Si. The Gaussian broadening with 0.025 eV width was used for smearing. In the horizontal axes, the bandgap energy (E_g) is set at zero. In Fig. (d), the experimental results of bulk Si are also plotted [21-25]. In Figs. (a)-(c), solid and broken lines show absorption coefficients for plane-polarized light with the polarization direction being parallel (//) and perpendicular (⊥) to the NW, respectively.

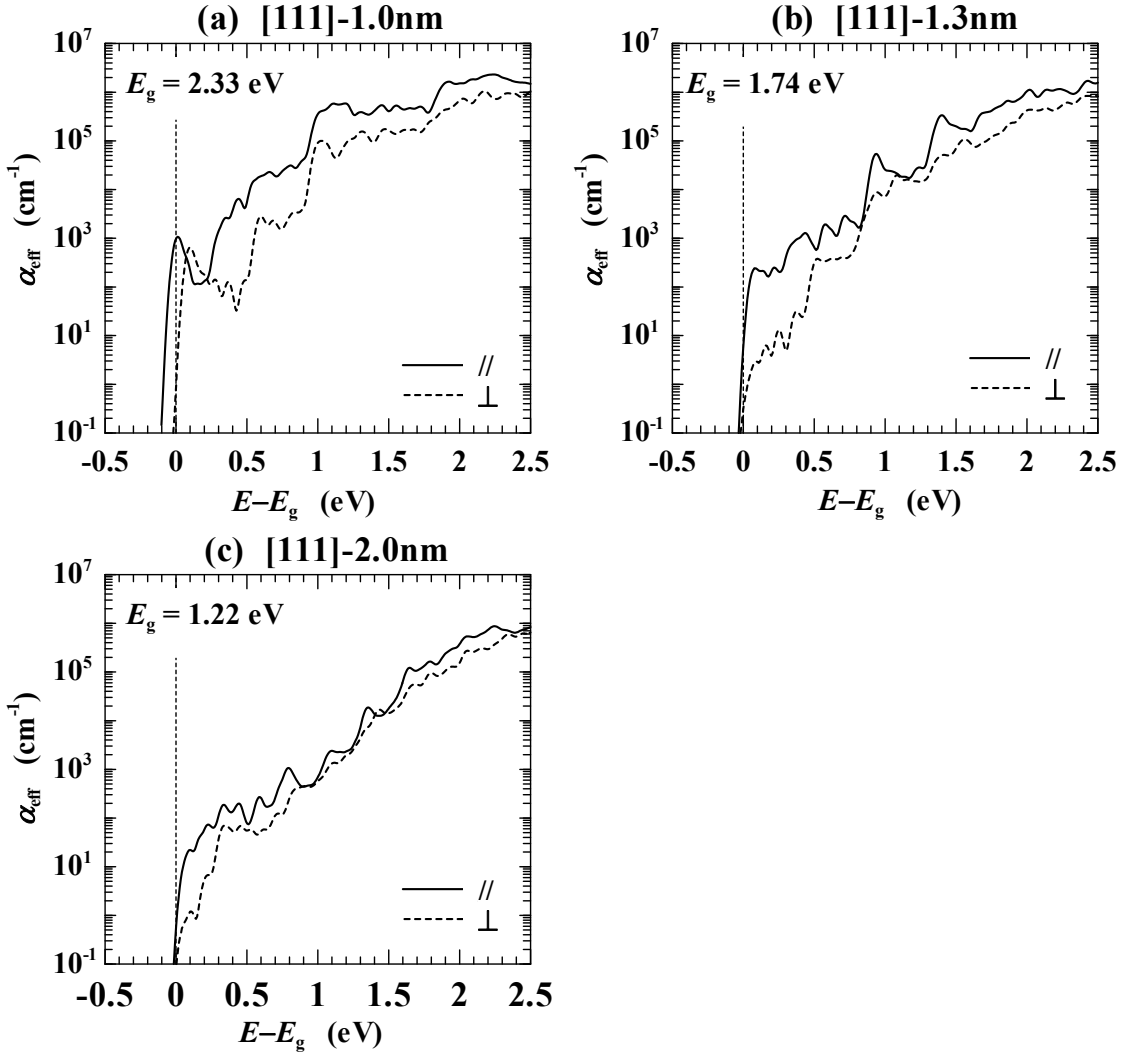

Fig. 5.8 Effective absorption coefficients (α_{eff}) of [111] Si NWs with different sizes. The Gaussian broadening with 0.025 eV width was used for smearing. In the horizontal axes, the bandgap energy (E_g) is set at zero. Solid and broken lines show absorption coefficients for plane-polarized light with the polarization direction being parallel (//) and perpendicular (⊥) to the NW, respectively.

Table 5.2 Symmetry operations of the space group No. 95 and No. 164, where the NW direction is *z*.

No. 95	x→	y→	z→
(1)	x	y	z
(2)	-x	-y	z+1/2
(3)	-y	x	z+3/4
(4)	y	-x	z+1/4
(5)	-x	y	-z
(6)	x	-y	-z+1/2
(7)	y	x	-z+1/4
(8)	-y	-x	-z+3/4

No. 164	x→	y→	z→
(1)	x	y	z
(2)	-y	x-y	z
(3)	-x+y	-x	z
(4)	y	x	-z
(5)	x-y	-y	-z
(6)	-x	-x+y	-z
(7)	-x	-y	-z
(8)	y	-x+y	-z
(9)	x-y	x	-z
(10)	-y	-x	z
(11)	-x+y	y	z
(12)	x	x-y	z

Table 5.3 Character tables of the space group No. 95 and No. 164, where the NW direction is *z*.

No. 95	(1)	(3,4)	(2)	(5,6)	(7,8)
A1	1	1	1	1	1
B1	1	-1	1	-1	1
B2	1	-1	1	1	-1
A2 (z)	1	1	1	-1	-1
E (x,y)	2	0	-2	0	0

No.164	(1)	(2,3)	(4,5,6)	(7)	(8,9)	(10,11,12)
A1g	1	1	1	1	1	1
A2g	1	1	-1	1	1	-1
Eg	2	-1	0	2	-1	0
A1u	1	1	1	-1	-1	-1
A2u (z)	1	1	-1	-1	-1	1
Eu (x,y)	2	-1	0	-2	1	0

Table 5.4 Direct product tables of the space group No. 95 and No. 164.

No. 95	A1	B1	B2	A2	E
A1	A1	B1	B2	A2	E
B1		A1	A2	B2	E
B2			A1	B1	E
A2				A1	E
E					A1+B1+B2+A2

No.164	A1g	A2g	Eg	A1u	A2u	Eu
A1g	A1g	A2g	Eg	A1u	A2u	Eu
A2g		A1g	Eg	A2u	A1u	Eu
Eg			A1g+A2g+Eg	Eu	Eu	A1u+A2u+Eu
A1u				A1g	A2g	Eg
A2u					A1g	Eg
Eu						A1g+A2g+Eg

Table 5.5 The allowed transitions at the Γ point for the [100] and [111] NWs for plane-polarized light with the polarization direction being parallel (//) and perpendicular (⊥) to the NW. The "Singly"/"Doubly" stands for singly/doubly degenerate state at the Γ point.

[100]NW	Singly ↔ Singly	Singly ↔ Doubly	Doubly ↔ Doubly
(//)	A1 ↔ A2 B1 ↔ B2		E ↔ E
(⊥)		A1 ↔ E A2 ↔ E B1 ↔ E B2 ↔ E	

[111]NW	Singly ↔ Singly	Singly ↔ Doubly	Doubly ↔ Doubly
(//)	A2g ↔ A1u A1g ↔ A2u		Eg ↔ Eu
(⊥)		A1g ↔ Eu A2g ↔ Eu A1u ↔ Eg A2u ↔ Eg	Eg ↔ Eu

[100] and [111] NWs. For the [100]-1.3nm, [100]-1.9nm, and [111]-1.0nm, both the CBM and VBM at the Γ point are singly degenerate states. Therefore, the transition between the CBM and VBM at the Γ point is forbidden for the perpendicular polarization. For [100]-3.0nm, [111]-1.3nm, and [111]-2.0nm, the energy shift of the absorption does not appear because singly and doubly degenerate states near the CBM at the Γ point are very close to each other.

5.4 Summary

Band structure, DOS, and absorption coefficient of <100> and <111> Si NWs were calculated by the density functional theory. The <100> NWs have direct band structure, while the band structure of the <111> NWs changes from indirect to direct with decrease in NW size. The DOS of the NWs has peaks corresponding to the one-dimensional DOS ($\propto E^{-0.5}$). The luminous efficiency of <100> NWs with a cross-sectional size below about 2 nm can be significantly higher than that of the bulk and may increase remarkably with decrease in NW size. In consideration of the indirect nature and the small absorption coefficient, <111> NWs are less attractive than <100> NWs. The absorption edge for the perpendicular polarization shifts to the higher energy side than the bandgap energy because of the forbidden transitions.

References

[1] R. A. Soref, Proc. IEEE **81**, 1687 (1993).
[2] B. Jalali and S. Fathpour, J. Lightwave Technol. **24**, 4600 (2006).
[3] F. Buda and J. Konanoff, Prog. Quantum Electron. **18**, 201 (1994).
[4] D. J. Lockwood, J. Mater. Sci.: Mater. Electron. **20**, S235 (2009).
[5] B. Gelloz and N. Koshida, J. Appl. Phys. **88**, 4319 (2000).
[6] W. L. Ng, M. A. Lourenco, R. M. Gwilliam, S. Ledain, G. Shao, and K. P. Homewood, Nature (London) **410**, 192 (2001).
[7] M. A. Green, J. Zhao, A. Wang, P. J. Reece, and M. Gal, Nature (London) **412**, 805 (2001).
[8] C. Harris and E. P. O'Reilly, Physica E **32**, 341 (2006).
[9] T. Vo, A. J. Williamson, and G. Galli, Phys. Rev. B **74**, 045116 (2006).
[10] D. B. Migas, J. Appl. Phys. **98**, 054310 (2005).
[11] G. D. Sanders and Y.-C. Chang, Phys. Rev. B **45**, 9202 (1992).
[12] F. Buda, J. Kohanoff, and M. Parrinello, Phys. Rev. Lett. **69**, 1272 (1992).
[13] X. Zhao, C. M. Wei, L. Yang, and M. Y. Chou, Phys. Rev. Lett. **92**, 236805 (2004).

[14] J. Li and A. J. Freeman, Phys. Rev. B **74**, 075333 (2006).

[15] M. D. Segall, P. J. D. Lindan, M. J. Probert, C. J. Pickard, P. J. Hasnip, S. J. Clark, and M. C. Payne, J. Phys.: Condens. Matter **14**, 2717 (2002).

[16] S. J. Clark, M. D. Segall, C. J. Pickard, P. J. Hasnip, M. J. Probert, K. Refson, and M. C. Payne, Z. Kristallogr. **220**, 567 (2005).

[17] J. P. Perdew, K. Burke, and M. Ernzerhof, Phys. Rev. Lett. **77**, 3865 (1996).

[18] P. Y. Yu, M. Cardona, *Fundamentals of Semiconductors: Physics and Materials Properties, 3rd ed.* (Springer Verlag, Berlin, 2001).

[19] J. H. Davies, *The Physics of Low-Dimensional Semiconductors* (Cambridge University Press, Cambridge, 1998).

[20] J.-P. Colinge, Solid-State Electron. **51**, 1153 (2007).

[21] E. D. Palik, *Handbook of Optical Constants of Solids* (Academic Press, Boston, 1985).

[22] D. E. Aspnes and J. B. Theeten, J. Electrochem. Soc. **127**, 1359 (1980).

[23] R. Hulthén, Phys. Scr. **12**, 342 (1975).

[24] G. G. Mcfarlane and V. Roberts, Phys. Rev. **98**, 1865 (1955).

[25] H. R. Philipp, J. Appl. Phys. **43**, 2835 (1972).

Chapter 6

Electroluminescence of Si-nanowire pn-diodes

6.1 Introduction

Si-based light emitters are in strong demand to combine photonics with Si-based electronics [1-3]. Although bulk Si is not suitable for light-emitting devices because of its indirect band structure, Si nanostructures are anticipated as light-emitting devices because the uncertainty of the crystal momentum increases by the quantum confinement effect and no-phonon radiative recombination may increase [4-7], which was confirmed quantitatively in Chapter 5.

Light-emitting diodes with such Si nanostructures as dots [8, 9], porous Si [10-12], nanowires [13], and nanofilms [14] have been previously proposed. Among Si nanostructures, the dots show the strongest quantum confinement, but carrier injection into them is difficult because their surfaces are usually covered with SiO_2. Nanowires (NWs) are more suitable for Si-based light-emitting devices due to easy carrier injection and strong quantum confinement. The luminous efficiency in Si NWs may be improved by utilizing the anisotropy of nanowires, as shown in Chapter 5. The anisotropy of luminescence may aid the understanding of the luminescence mechanism.

The external-quantum-efficiency of bulk Si light-emitting-diodes has reached up to 10^{-2} by introducing into the devices, for example, dislocation [15] or a pyramidal surface [16], whereas the external-quantum-efficiency of the Si nanostructures has reached up to 10^{-2} by porous Si [12]. The mechanism of light emission in Si nanostructure remains unclarified. It is reported that the interfacial layer between the Si nanostructure and the SiO_2 surrounding the Si nanostructure plays an important role in light emission [17]. That is, it remains unclear whether the emission from the Si nanostructure is real emission by band-edge transition from the Si nanostructures or not. Concerning Si NWs, Si-NW diodes with a NW cross-sectional diameter below 10 nm and a NW length of 400~600 nm have been reported [13]. Electroluminescence at 650 nm was observed, but the origin of the luminescence is not clear.

Understanding the mechanism of light emission is crucial to increase the luminous efficiency. In this study, the author investigated light emission by band-edge transition from Si NWs using Si-NW pn-diodes, and observed the increase of emission energy with a decrease in NW cross-sectional size from the emission energy of the band-edge transition of bulk Si to higher energy.

6.2 Device structure and fabrication

Figure 6.1 illustrates the schematic structure of the Si-NW pn-diodes fabricated in this study. The lengths of the low-impurity-concentration area in the Si NWs, the distance between electrodes, and the Si-NW length were 0.5, 5, and 15 μm, respectively. The NW cross-sectional height (thickness) was 17 nm, and the patterning width (W_P) of the NWs was changed from 500 to 40 nm. About 300~2,000 NWs were distributed within a 200-μm-wide area and were connected in parallel to increase the total luminescence intensity. The surface of the Si NWs was passivated with a 49-nm-thick SiO_2. Si NWs were formed from a (001) Si-film, and the NW direction was [100]. The [100] NWs is expected to have direct band structure and efficient luminescence as shown in Chapter 5. The low impurity-concentration area remained as the starting material of the p-type with a resistivity of 5~50 Ω·cm. The electrodes were directly contacted to the Si NWs to eliminate luminescence from a Si film. If the NWs are connected to electrodes through Si films like the NW MOSFETs in Chapter 3, luminescence from the Si films will hinder the detection of the luminescence from the Si NWs.

The fabrication procedure of NWs was similar to that described in Section 2.2, but oxidation at 1,000˚C was carried out once in place of the 3rd and 4th oxidations, by which 49-nm-thick SiO_2 passivation was formed. The formation of n^+/ p^+ Si, the forming annealing, and the formation of electrode contacts were carried out in the same way as described in Section 3.2.

NWs as long as 5 μm (distance between electrodes) were adopted for pn-diodes to increase the recombination amount in NWs. As a result, the minimum cross-sectional size of NWs was relatively large, about 9 nm. Figure 6.2 shows the top view of the NWs with a minimum W_P of 40 nm by SEM just after the resist removal that followed reactive ion etching. Since observation of the cross-sectional shape by TEM was not performed, the cross-sectional area (A) of one Si NW was estimated from W_P, the Si film thickness, and the Si decrease by oxidation. Cross-sectional size W (the square root of A) and total cross-sectional area (A_T) (A multiplied by number of NWs) were calculated using A. Figure 6.3 shows the W_P dependence of the estimated A, A_T, and W. The estimated W of the NWs changed from 88 to 9 nm by changing W_P from 500 to 40 nm.

6.3 Measurement method of electroluminescence

Electroluminescence (EL) was measured using spectroscopy system (C9913GC by Hamamatsu Photonics) with 70 μm × 500 μm entrance slit. Luminescence was taken in by an optical fiber with a diameter of 600 μm, numerical aperture of 0.22, length of 1.5 m, and loss less than 0.015 dB/m. The

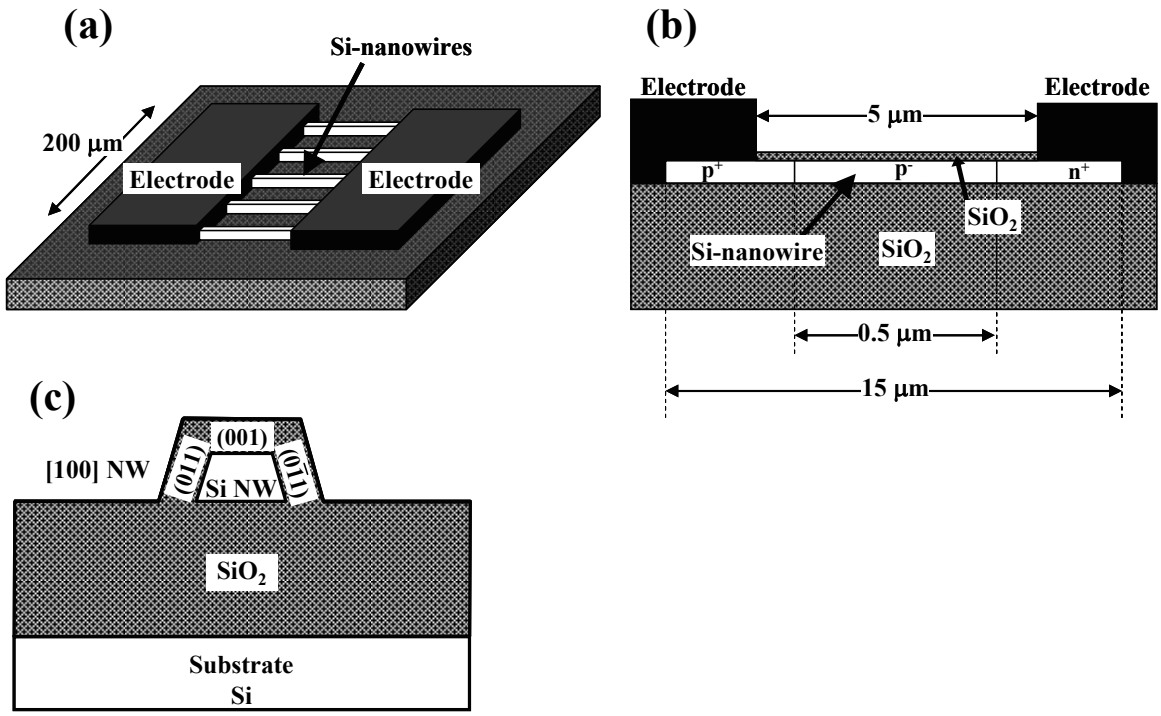

Fig. 6.1 The schematic structure of the fabricated Si-NW pn-diodes: (a) the bird's-eye view, (b) the cross-sectional view parallel to the NW, (c) the cross-sectional view perpendicular to the NW. The crystal faces of the sides shown in (c) are high-symmetry faces close to the actual side faces.

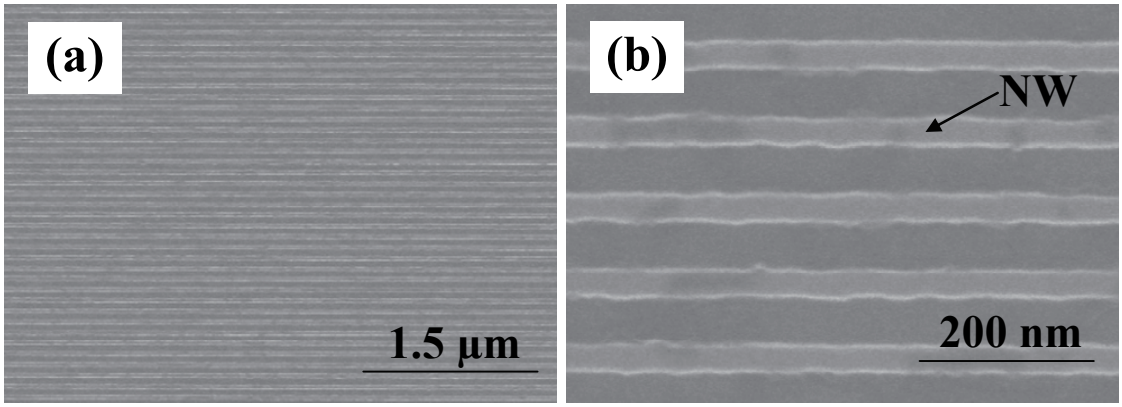

Fig. 6.2 Top-view SEM images of NWs with a minimum W_P of 40 nm just after the resist removal following RIE: (a) low magnification and (b) high magnification. The acceleration voltage was 25 keV.

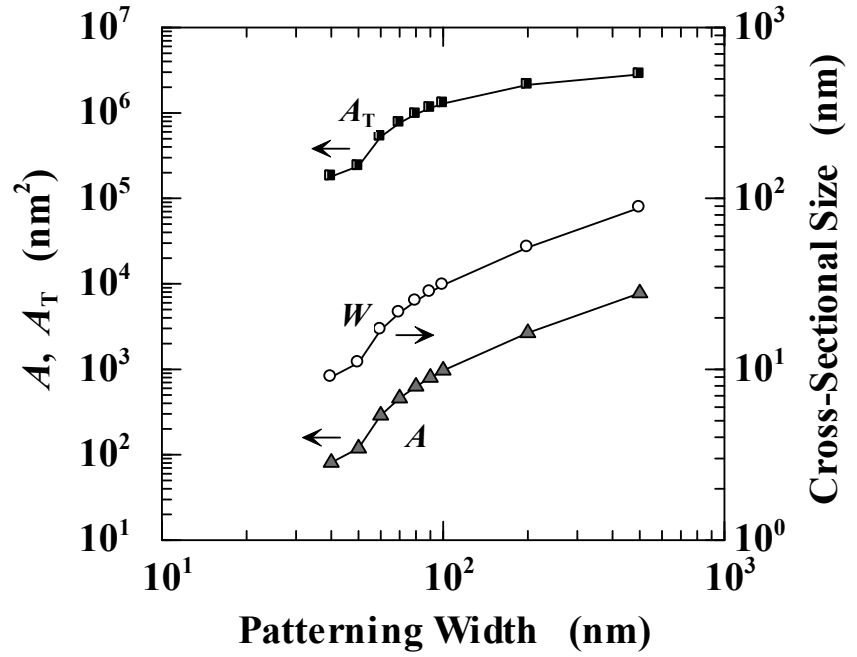

Fig. 6.3 Patterning width (W_P) dependence of the estimated cross-sectional area (A), total cross-sectional area (A_T), and cross-sectional size (W).

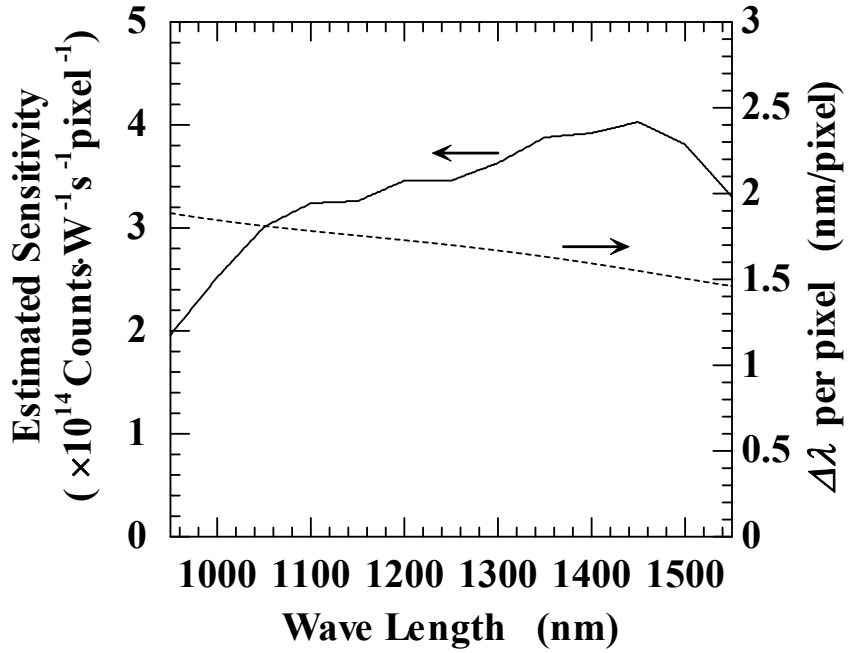

Fig. 6.4 (left axis) The estimated sensitivity (S) of the spectroscopy system to the light entering the slit presented by the manufacturer. (right axis) The wavelength width per pixel ($\Delta\lambda$).

fiber was set over a chip including diodes with a distance slightly less than 1.33 mm in consideration of numerical aperture of the fiber. Measured count ($C(\lambda)$) was converted to normalized EL intensity ($I(E)$) by

$$I(E) = \frac{\lambda^3}{tSc^2h^2I\Delta\lambda} C(\lambda), \tag{6.1}$$

and

$$E = \frac{ch}{\lambda}, \tag{6.2}$$

where λ is the wave length of photons, t is the integration time, S is the estimated sensitivity of the spectroscopy system to the light entering the slit presented by the manufacturer (Fig. 6.4), I is the current passing a diode, and $\Delta\lambda$ is the wavelength width per pixel (Fig. 6.4). That is, the $I(E)$ is the number of photons entering the slit per photon energy, integration time, and current.

6.4 Device characterization and discussion

6.4.1 Current-voltage characteristics

Figure 6.5(a) shows the current-voltage characteristics of the Si-NW pn-diodes, and Fig. 6.5(b) shows the W_P dependence of the current density at ±1 V. The diodes showed normal rectification for all W_Ps. Forward current density (I_F/A_T) decreased with a W decrease, while reverse current density (I_R/A_T) increased. That is, rectification was degraded with a W decrease. Although hysteresis was observed in the forward bias, the origin is not clear at present. The ideality factor η defined as [18]

$$1/\eta = \frac{kT}{e}\frac{d(\ln I)}{dV}, \tag{6.3}$$

is shown in Fig. 6.6. For W = 88 nm, η was between 1 and 2, which agrees with the bulk-Si pn-diode [19], but η increased to about 3 with a W decrease. The hysteresis of I_F/A_T and the increase of η probably originate in the increase of the contact resistance between the metal electrodes and n^+/p^+ Si. To directly form ohmic contacts on Si NWs was more difficult than on bulk Si. The increase in leakage current density I_R/A_T probably originates in the increase of the generation-center concentration by the increase of the Si-NW interface area relative to the Si-NW volume.

6.4.2 Electroluminescence

Figure 6.7 shows the EL spectra of Si-NW pn-diodes at room temperature. For W = 88 nm, a single peak at 1.092 eV was observed. Although the peak energy of 1.092 eV was slightly larger than that of bulk reported so far (1.08~1.09 eV) [15, 16, 20], the peak undoubtedly originates in the

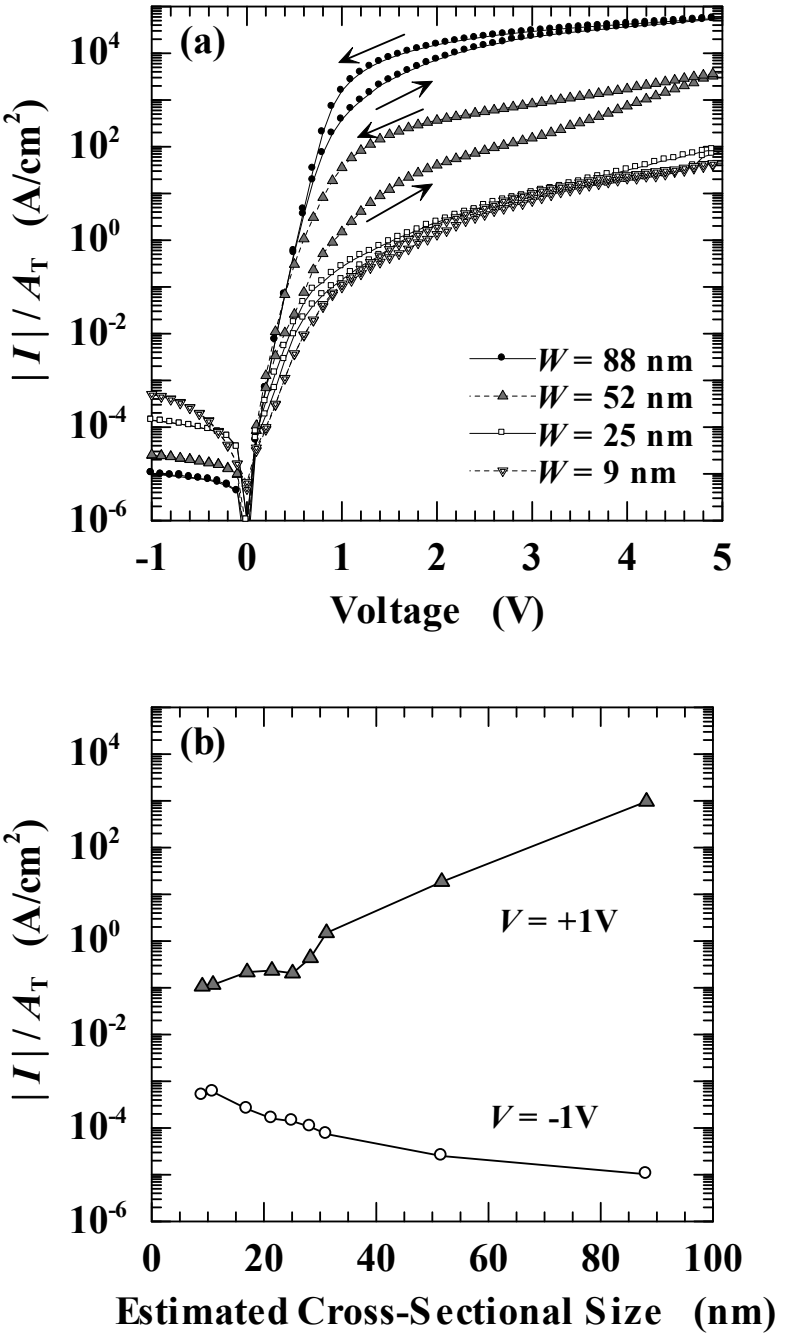

Fig. 6.5 (a) Current density of Si-NW pn-diodes as a function of voltage. (b) The estimated cross-sectional size (W) dependence of current density at ±1 V.

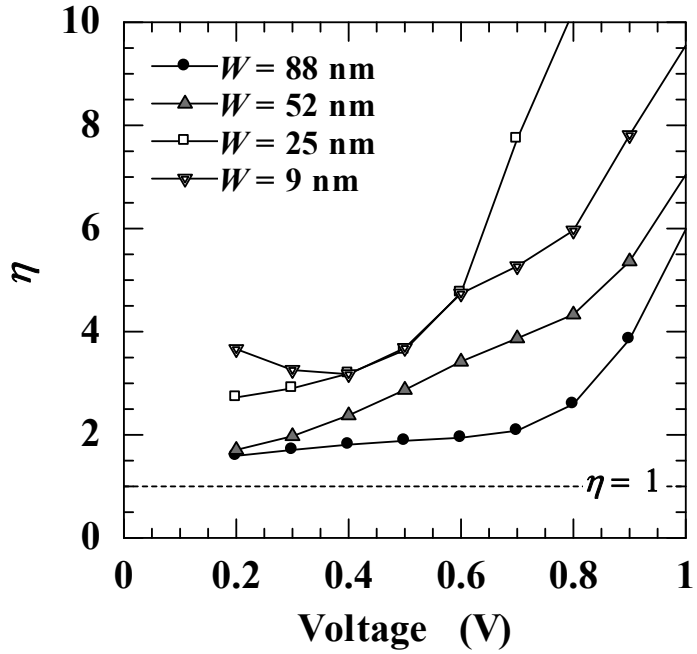

Fig. 6.6 Ideality factor (η) of Si-NW pn-diodes as a function of voltage, which is obtained from forward current when voltage sweeps down shown (Fig. 6.5(a)).

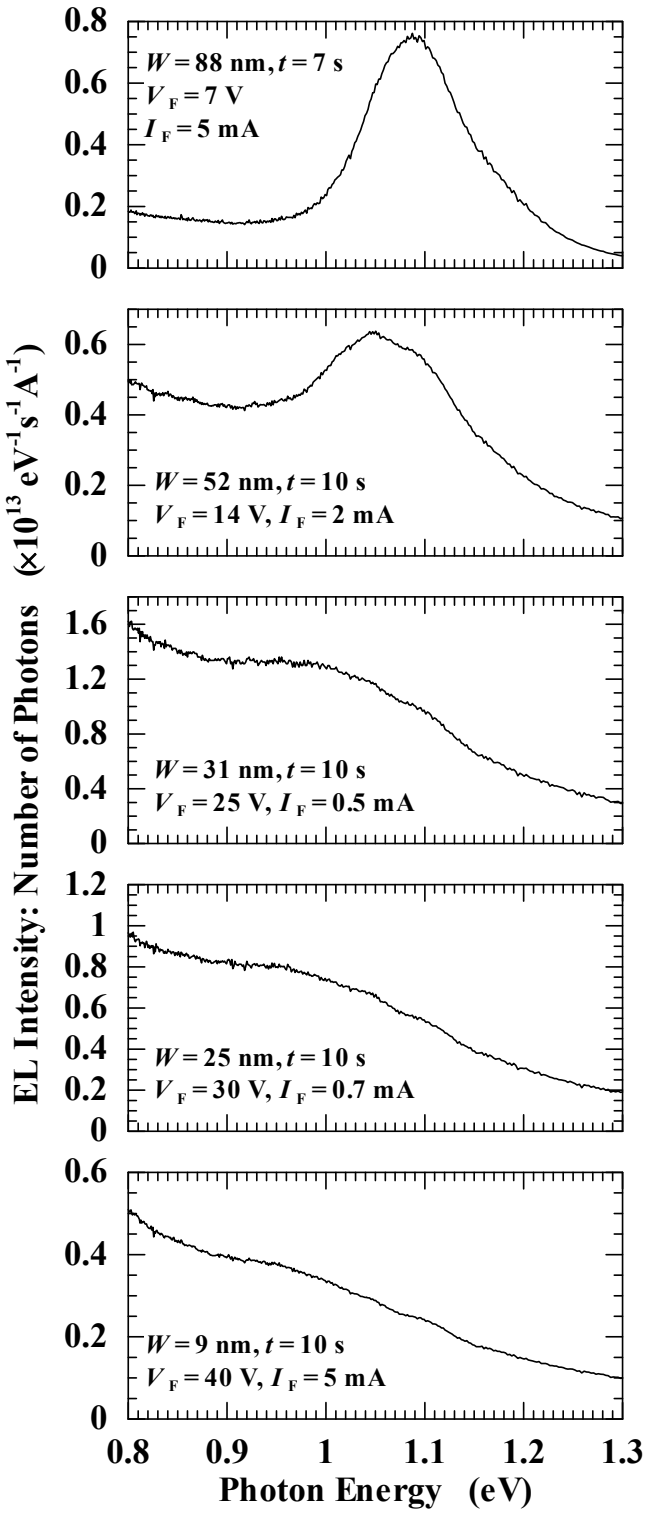

Fig. 6.7 Electroluminescence (EL) spectra of various Si-NW pn-diodes in the infrared region.

emission by band-edge transition in bulk Si (Si wires with large cross-sectional size). The peak intensity weakened with a W decrease. The intensity of the background spectrum, which monotonously increased with a photon-energy decrease, relatively increased with a W decrease. The origin of the background spectra has not been clarified. To analyze the emission from Si NWs in detail, the background spectra were subtracted from the original spectra as shown in Fig. 6.10(a). Figure 6.8 shows the EL spectra from Si NWs after the background subtraction. For $W < 31$ nm, the luminescence from Si NWs consisted of three peaks: a broad peak with lower energy (~ 1.0 eV) and two small peaks at about 1.046 and 1.104 eV. The broad peak, the 1.046-eV-peak, and the 1.104-eV-peak were observed for $W < 31$ nm, $W < 52$ nm, and $W < 31$ nm, respectively. Although the peak energy of 1.104eV is slightly larger than peak energy of 1.092 eV for $W = 88$ nm, the peak probably originates in the emission by band-edge transition in the Si NWs. To analyze the two small peaks in detail, the background and broad peak (~ 1.0 eV) spectra were subtracted as shown in Fig. 6.10(b), and Fig. 6.9 shows the EL spectra after this subtraction of the broad peak spectra. The width of the peak at 1.104eV for $W < 31$ nm was narrower than that of the peak by bulk band-edge transition for $W = 88$ nm, which may originate in the realization of the one-dimensional density of states in Si NWs. The one-dimensional density of states takes a peak at band edge ($\propto E^{-0.5}$), by which band-edge transition rate increases. The origins of the broad peak (~ 1.0 eV) and 1.046-eV-peak have not been clarified.

Figure 6.11 shows the current (I_F) dependence of the EL spectrum for $W = 9$ nm after the subtracting the background and broad peak spectra. The intensity of the two peaks increased with an I_F increase, and the peak intensity at 1.104 eV increased relative to the peak intensity at 1.046 eV. The peak energy was not changed with I_F.

External-quantum-efficiency of the 1.104-eV-peak of the NW diode with $W = 9$ nm at $I_F = 5$ mA was estimated. External-quantum-efficiency (γ) was estimated from the number of photons entering the slit ($I(E)$ at $I_F = 5$ mA shown in Fig. 6.11) by

$$\gamma = e\frac{S_f}{S_s}\frac{4\pi}{\omega}\int I(E)dE\,, \tag{6.4}$$

where integration ranges from1.07 to 1.14 eV, S_f/S_s is the ratio of the fiber (S_f) and slit (S_s) areas and the vale is 8.078. The $\omega/4\pi$ is the ratio of the fiber (ω) and total (4π) solid angles and given by

$$\frac{\omega}{4\pi} = \sin^2\left(\frac{1}{2}\tan^{-1}\left(\frac{d}{2L}\right)\right) = 1.225\times10^{-2}\,, \tag{6.5}$$

where d is diameter of fiber (600 μm) and L is distance between the device and fiber (1.33 mm). For the estimation, it is assumed that the luminescence is isotropic and loss in chip is zero. The γ was 7×10^{-7}, which was very low in comparison with Si nanostructure diodes reported so far (10^{-5}~10^{-2}) [4,6,12].

Figure 6.12 shows the W dependence of the energy of three EL peaks, and Fig. 6.13 shows the bandgap-energy shift obtained from the EL peak by band-edge transition provided that the phonon energy involved in the band-edge transition in NW remained the same as that of the bulk. The

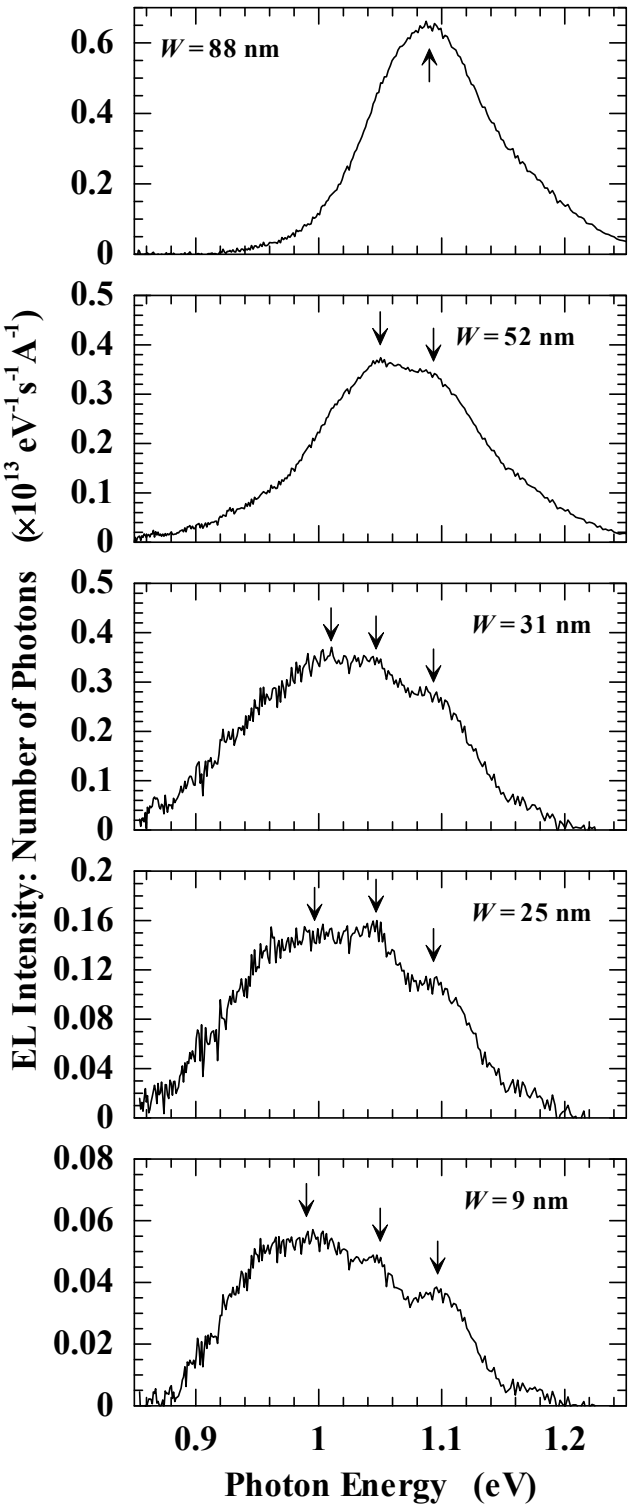

Fig. 6.8 Electroluminescence (EL) spectra of various Si-NW pn-diodes after the subtraction of background spectrum.

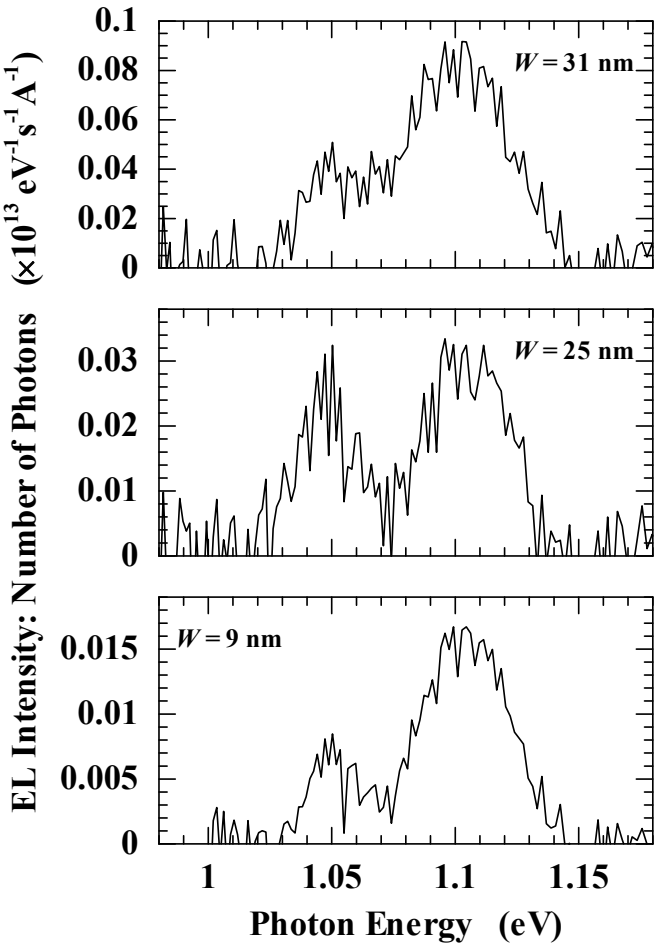

Fig. 6.9 Electroluminescence (EL) spectra of Si-NW pn-diodes after the subtraction of the background spectrum and the broad peak spectrum.

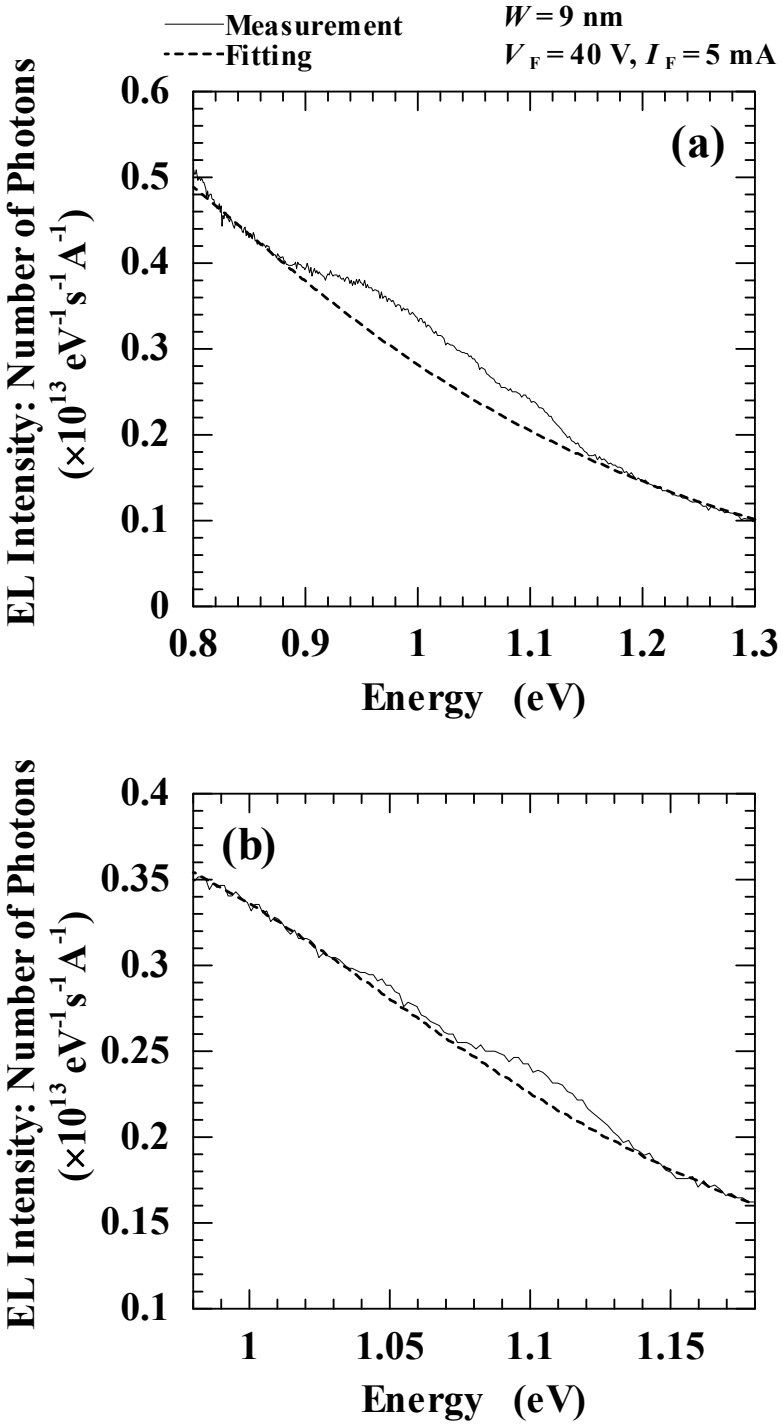

Fig. 6.10 The large scale spectrum around peaks for $W = 9$ nm. (a) The broken line is a line fitting to the background spectrum and shows subtracted amount to extract the broad peak and small two peaks. (b) The broken line is a line fitting to the background and broad-peak spectra and shows subtracted amount to extract the small two peaks.

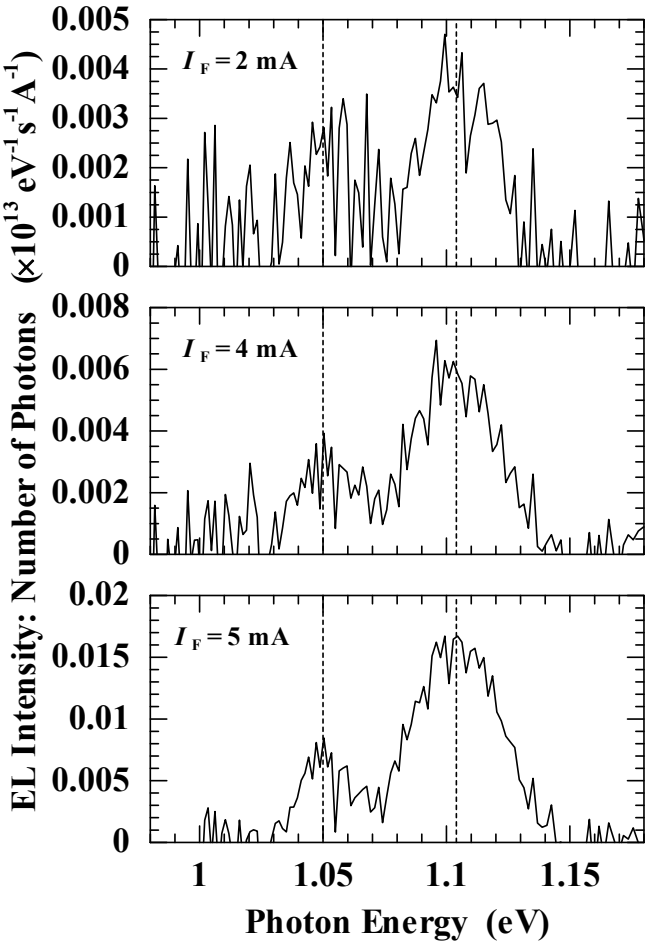

Fig. 6.11 The forward current dependence of spectrum for W = 9 nm after the subtraction of the background spectrum and the broad peak spectrum.

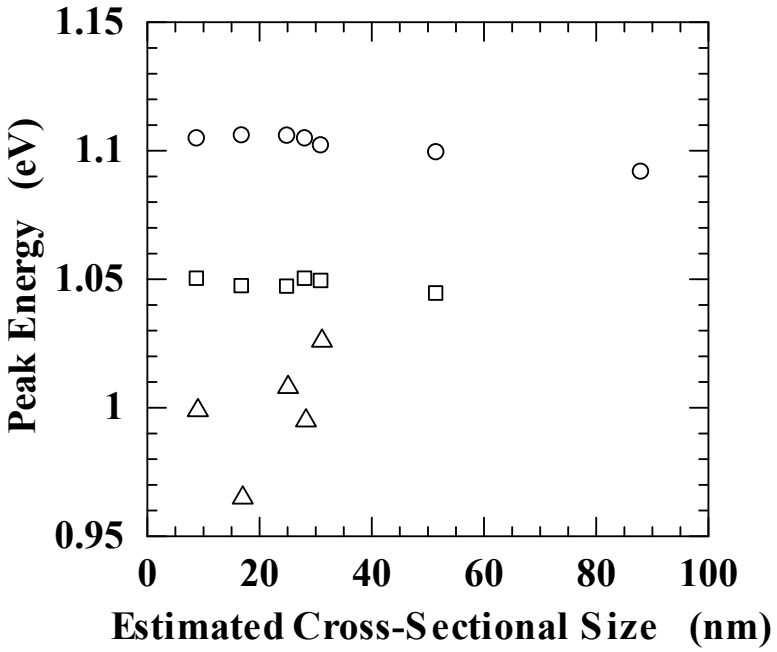

Fig. 6.12 The estimated cross-sectional size (W) dependence of energy of three EL peaks from Si NWs. The energies of three peaks are plotted with different symbols.

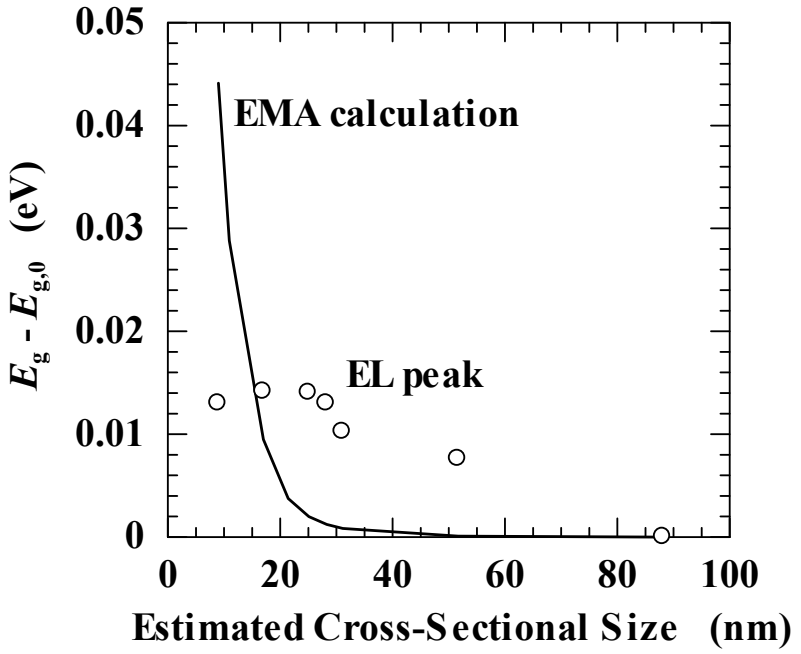

Fig. 6.13 The estimated cross-sectional size (W) dependence of band-gap shift obtained from EL peak of Si NW diodes by band edge transition (open circles) and calculated by effective mass approximation (EMA) (solid line). The $E_{g,0}$ shows band-gap energy of Si NWs with W = 88 nm.

bandgap shift, calculated by effective mass approximation (Section 1.2.2), is also shown, where the estimated cross-sectional size (Fig. 6.3) was used. Although the energy shift obtained from the EL peak does not agree well with that calculated by effective mass approximation, the shift of the EL peak with a *W* decrease from 1.092 eV (*W* = 88 nm) to 1.104 eV (*W* = 31~9 nm) perhaps originates in the bandgap increase by the quantum confinement effect. For *W* < 31 nm, the shift energy obtained from the EL peak slightly decreased with a *W* decrease, which might originate in the bandgap narrowing due to temperature increase caused by high current density (~ 1×10^6 A/cm^2); larger current density was applied for smaller *W* during the EL measurement.

6.5 Summary

Si-NW pn-diodes were fabricated, and the dependence of electroluminescence on the NW size was investigated. The diodes showed normal rectification for all *W*s. For a diode with an estimated cross-sectional size (*W*) of 88 nm, a single peak at 1.092 eV was observed, which undoubtedly originates in the emission by band-edge transition in bulk Si (Si wires with large cross-sectional size). For the diodes with an estimated *W* smaller than 31 nm, three peaks were observed. The peak energies were 1.104 eV, 1.050 eV, and about 1.0 eV for an expected *W* of 9 nm. Since the peak energy 1.104 eV is slightly larger than bulk-Si energy of 1.092 eV, the peak at 1.104 eV perhaps originates in the band-edge transition in Si NWs where the bandgap is widened by quantum confinement effect.

References

[1] R. A. Soref, Proc. IEEE **81**, 1687 (1993).
[2] P. Ball, Nature **409**, 974 (2001).
[3] B. Jalali and S. Fathpour, J. Lightwave Technol. **24**, 4600 (2006).
[4] F. Buda and J. Kohanoff, Prog. Quant. Electr. **18**, 201 (1994).
[5] D. Kovalev, H. Heckler, G. Polisski, and F. Koch, Phys. Stat. Sol. (b) **215**, 871 (1999).
[6] M. S. Hybertsen, Phys. Rev. Lett. **72**, 1514 (1994).
[7] C. Delerue, G. Allan, and M. Lannoo, Phys. Rev. B **48**, 11024 (1993).
[8] L. Pavesi, L. D. Negro, C. Mazzoleni, G. Franzò, and F. Priolo, Nature **408**, 440 (2000).
[9] N. M. Park, T. S. Kim, and S. J. Parka, Appl. Phys. Lett. **78**, 2575 (2001).
[10] N. Koshida and H. Koyama, Appl. Phys. Lett. **60**, 347 (1992).
[11] P. Steiner, F. Kozlowski, and W. Lang, Appl. Phys. Lett. **62**, 2700 (1993).

[12] B. Gelloz and N. Koshida, J. Appl. Phys. **88**, 4319 (2000).

[13] A. G. Nassiopoulos, S. Grigoropoulos, and D. Papadimitriou, Appl. Phys. Lett. **69**, 2267 (1996).

[14] S. Saito, D. Hisamoto, H. Shimizu, H. Hamamura, R. Tsuchiya, Y. Matsui, T. Mine, T. Arai, N. Sugii, K. Torii *et al.*, Jpn. J. Appl. Phys. **45**, L679 (2006).

[15] W. L. Ng, M. A. Lourenço, R. M. Gwilliam, S. Ledain, G. Shao, and K. P. Homewood, Nature **410**, 192 (2001).

[16] M. A. Green, J. Zhao, A. Wang, P. J. Reece, and M. Gal, Nature **412**, 805 (2001).

[17] Y. Kanemitsu, T. Ogawa, K. Shiraishi, K. Takeda, Phys. Rev. B **48**, 4883 (1993).

[18] S. M. Sze, *Semiconductor Devices: Physics and Technology 2nd ed.* (John Wiley, New York, 2002).

[19] A. S. Grove, *Physics and Technology of Semiconductor Devices* (John Wiley, New York, 1967).

[20] A. M. Emel'yanov, N. A. Sobolev, E. I. Shek, Physics of the Solid State **46**, 44 (2004).

Chapter 7

Conclusions

7.1 Conclusions

Electronic states, carrier transport, and optical properties of Si nanowires (NWs) were investigated to utilize the unique properties of Si NWs for advanced MOSFETs and light-emitting devices. First, a fabrication process of Si NWs was established. The quantum confinement effect (QCE) was clearly confirmed in Si-NW MOSFETs by threshold-voltage shift, unique dependence of mobility on NW size, and transconductance oscillation. One-dimensional transport model in Si-NW MOSFETs that reproduces the drain-current oscillation was proposed. The dependence of absorption coefficients on the NW size and its anisotropy were revealed by the calculation based on density functional theory. Electroluminescence from Si-NW pn-diodes was observed.

In Chapter 2, a fabrication process of Si NWs was established. A nearly-ellipsoid Si-NW with a minimum cross-sectional size W (square root of the area) of 4 nm (height: 2 nm, width: 7 nm) was successfully formed. The small W well below 10 nm enables to investigate QCE in Si NWs. Moreover, the W of Si NWs was gradually changed from 18 to 4 nm by changing the patterning width, which enabled to investigate size dependence of characteristics of Si-NW MOSFETs in Chapter 3. The fabrication method was also applied to Si-NW pn-diodes characterized in Chapter 6.

In Chapter 3, Si-NW MOSFETs were characterized, where Si NWs fabricated in Chapter 2 were used as a channel. Both n- and p-channel MOSFETs showed good gate control with a nearly ideal subthreshold swing of 63 mV/decade. The bandgap widening by the QCE was clearly confirmed from the threshold-voltage shift. Two confinement conditions of carriers were indicated from the W dependence of ratio of electron and hole mobilities. Carriers in NW MOSFETs with $W > 7$ nm are confined at the surface of NWs by electric field induced by gate voltage like carriers in bulk MOSFETs. On the other hand, carriers in NW MOSFETs with $W < 7$ nm are confined by a SiO_2 potential surrounding the Si NW and distributed throughout the NW (volume inversion). Both of electron and hole mobilities conspicuously decreased for $W < 9$ nm, which probably originates in the increase of the surface-roughness scattering. This result indicates that carriers in NWs with $W <$ 9 nm are distributed more close to the interface than carriers in bulk MOSFETs because of carrier confinement in small NW. [100]- and [110]-NW MOSFETs were characterized and no anisotropic characteristics were observed, which is inconsistent with the theoretically-expected large differences

of the hole effective mass between [100] and [110] NWs.

In Chapter 4, the drain-current oscillation peculiar to NW MOSFETs was experimentally and theoretically investigated. The transconductance of a fabricated Si-NW MOSFET with W = 6 nm showed clear oscillation up to 309 K. The magnitude of the oscillation was larger for lower temperature, lower drain voltage, or smaller W. A carrier transport model, assuming one-dimensional electronic states for carriers and elastic and isotropic phonon scattering, was proposed. The carrier concentration calculated by the model changed linearly with gate voltage, while the mobility showed clear oscillation with gate voltage. The calculated transconductance of NW MOSFETs showed similar oscillation to the experimental results. The model shows that the oscillation originates from the periodic variations in the mobility (scattering rate) caused by one-dimensional density of states ($\propto E^{-0.5}$), and one set of peak and valley of the oscillation corresponds to one subband.

In Chapter 5, the electronic states and absorption coefficients of Si NWs by direct band-to-band transition were calculated. The <100> NWs showed direct band structure, while the band structure of <111> NWs changed from indirect to direct with a W decrease. The absorption coefficients of <100> Si-NWs for the polarization parallel to the NW showed a peak at the bandgap energy, and the peak increased with a W decrease. For W < 2 nm, the absorption coefficient at the bandgap energy was larger than the measured absorption coefficient at the bandgap energy of bulk Si. The <111> NWs showed a smaller absorption coefficient than the <100> NWs. Therefore, the <100> NWs with a size below about 2 nm are attractive from the standpoint of efficient luminescence. The absorption edge for the perpendicular polarization shifted to the higher energy side than the bandgap energy because of the forbidden transitions.

In Chapter 6, the dependence of the electroluminescence of Si-NW pn-diodes on W was investigated. For the diode with an expected W of 88 nm, a single peak at 1.092 eV was observed, which undoubtedly originates in the emission by band-edge transition in bulk Si (Si wires with large cross-sectional size). For the diodes with expected Ws smaller than 31 nm, three peaks were observed. The peak energies were 1.104 eV, 1.050 eV, and about 1.0 eV for an expected W of 9 nm. Since the energy 1.104 eV is slightly larger than the bulk-Si energy of 1.092 eV, the peak at 1.104 eV perhaps originates in band-edge transition in Si NWs with the bandgap widened by QCE.

7.2 Future work

(1) Reduction of NW fluctuation

The cross-sectional size of Si NWs and the characteristics of Si-NW MOSFETs were well controlled by patterning width with a small dispersion (Figs. 2.7, 3.7 and 3.8), from which it can be claimed that the NW fluctuation was controlled within a few nm. However, the interface of NWs

characterized by TEM was not very clear and fluctuation of about 1 nm still existed (Fig. 2.5), which probably originates in the line edge roughness during electron beam lithography. Mobility degradation in Si-NW MOSFETs for $W < 9$ nm also indicates the existence of fluctuation.

Electron beam lithography conditions must be further optimized. Additional treatments such as wet etching in an alkaline solution may be proper to reduce the fluctuation, though the NW direction can not be selected freely.

(2) Improvement of mobility

The author revealed that QCE in NW MOSFETs becomes conspicuous for $W < 7$~9 nm, but the increase or anisotropy of mobility was not observed. The author proposes two ways to increase the mobility: selection of small conductivity effective mass and reduction of surface-roughness scattering. Surface-roughness scattering would be decreased by the reduction of NW fluctuation.

The model proposed in Chapter 4 revealed that one set of peak and valley of the drain-current oscillation corresponds to one subband. Although the simplest subband structure was assumed in this study, subband structure (band-edge energy and effective mass of each subband) can be determined so as to fit each peak and valley of calculated oscillation to experimental results. On the other hand, the subband structure of expected Si NWs can be determined by theoretical calculation. But determining the subband structure of actual NWs only by calculation is difficult because knowing structure of actual NWs precisely is difficult. Both analyses of experimental oscillation at low temperature and theoretical calculation of band structure are necessary to determine the subband structure. After knowing the subband structure, by selecting shape, size, or direction of Si NWs so as to have small conductivity effective mass, mobility at room temperature will be increased.

(3) Improvement of electroluminescence efficiency

Since electroluminescence from Si-NW pn-diodes was observed, the next step is improvement of electroluminescence efficiency. For example, the improvement of contact resistance between Si-NWs and electrodes for easy current injection and optimization of NW length so as to maximize recombination of electrons and holes in Si NWs will result in the improvement of the efficiency.

The NW size dependence and the anisotropy of absorption coefficients by direct band-to-band transition were revealed by calculation. Making good use of the direct transition and anisotropy will also result in the improvement of the efficiency. Investigation on anisotropy of electroluminescence from Si-NW pn-diodes, and separation of luminescence by phonon-related transition and direct transition by low temperature measurement is important to clarify the origin of luminescence and increase the efficiency.

List of major symbols and abbreviation

Symbol	Quantity	Value
c	Light velocity in vacuum	2.998×10^{8} m·s^{-1}
e	Elementary electric charge	1.602×10^{-19} C
h	Plank constant	6.626×10^{-34} J·s
$\hbar$	Reduced Plank constant	1.055×10^{-34} J·s
k	Boltzmann constant	1.381×10^{-23} J·K^{-1}
m_0	Electron mass	9.109×10^{-31} kg
ε_0	Dielectric constant in vacuum	8.854×10^{-12} F·m^{-1}

Symbol	Quantity
a	Lattice constant of bulk Si
C	Capacitance
C_{OX}	SiO_2 capacitance between gate electrode and NW channel per unit length of NW
E	Energy
E_C	Energy of conduction-band minimum
E_F	Energy of Fermi level
E_g	Bandgap energy
E_V	Energy of valence-band maximum
$g(E)$	Density of states
g_m	Transconductance of MOSFET
I_D, I_{DS}	Drain current of MOSFET
I_F and I_R	Forward and reverse current of diode
k	Wave number
m^*	Effective mass of carriers
T	Temperature
V_D, V_{DS}	Drain voltage of MOSFET
V_F and V_R	Forward and reverse voltage of diode
V_G, V_{GS}	Gate voltage of MOSFET
V_{th}	Threshold voltage of MOSFET
W	Cross-sectional size of NW
W_P	Patterning width of NW
α	Absorption coefficient

λ	Wave length
μ	Mobility

Abbreviations

CBM	conduction band minimum
CMOS	complementary metal oxide semiconductor
DFT	density functional theory
DOS	density of states
EB	electron beam
EL	electroluminescence
EMA	effective mass approximation
LSI	large-scale integrated circuit
MOSFET	metal-oxide-semiconductor field effect transistor
NW	nanowire
QCE	quantum confinement effect
RIE	reactive ion etching
RT	room temperature
SCE	short-channel effect
SEM	scanning electron microscopy
SOI	Si-on-insulator
TB	tight-binding method
TEM	transmission electron microscopy
VBM	valence band maximum

List of publications

A. Full length papers

1. **H. Yoshioka**, N. Morioka, J. Suda, and T. Kimoto,
   "Mobility oscillation by one-dimensional quantum confinement in Si-nanowire metal-oxide-semiconductor field effect transistors,"
   Journal of Applied Physics **106**, pp. 034312–1-034312–6 (2009).
2. **H. Yoshioka**, N. Morioka, J. Suda, and T. Kimoto,
   "Band edge transitions in <100> and <111> Si-nanowires calculated by density functional theory,"
   submitted to IEEE Transactions on Nanotechnology.
3. **H. Yoshioka**, N. Morioka, J. Suda, and T. Kimoto,
   "Electron and hole mobility in Si-nanowire MOSFETs,"
   in preparation.

B. Proceedings of international conference

1. **H. Yoshioka** and T. Kimoto
   "Investigation of mobility degradation in ultra-thin silicon-on-insulator by Hall effect measurements,"
   Ext. Abstr. of Asia-Pacific Workshop on Fundamentals and Applications of Advanced Semiconductor Devices, pp. 47-52, Gyeongju, Korea, June 2007.
2. **H. Yoshioka**, Y. Nanen, J. Suda, and T. Kimoto,
   "Fabrication and electronic characteristics of silicon nanowire MOSFETs,"
   Proc. of Materials Research Society 2008, Spring Meeting, 1080-O12-02, San Francisco, USA, March 2008.
3. **H. Yoshioka**, N. Morioka, J. Suda, and T. Kimoto,
   "One-dimensional quantum confinement effects in Si-nanowire MOSFETs,"
   Ext. Abstr. of IEEE International Meeting for Future of Electron Devices, Kansai, pp. 106-107, Osaka, Japan, May 2009.

C. Other full length papers

1. H. Wada, **H. Yoshioka**, and T. Goto,
   "Novel magnetic phase transitions and magnetoresistance of $GdMn_2Ge_2$,"
   Journal of Physics: Condensed Matter **14**, pp. L687-L693 (2002).

2. H. Wada, **H. Yoshioka**, T. Goto, K. Koyama, and K. Watanabe,
"Novel field-induced magnetic transitions of $GdMn_2Ge_2$,"
Journal of the Physical Society of Japan **72**, pp. 3197-3203 (2003).
3. H. Wada, **H. Yoshioka**, T. Goto, and K. Koyama,
"Field-induced magnetic transitions of exchange competing system $GdMn_2Ge_2$,"
Journal of Magnetism and Magnetic Materials **272**, pp. 591-592 (2004).
4. W. Saito, I. Omura, S. Aida, S. Koduki, M. Izumisawa, **H. Yoshioka**, and T. Ogura,
"High breakdown voltage (>1000V) semi-superjunction MOSFETs using 600-V class superjunction MOSFET process,"
IEEE Transactions on Electron Devices **52**, pp. 2317-2322 (2005).
5. Y. Nanen, **H. Yoshioka**, M. Noborio, J. Suda, and T. Kimoto,
"Enhanced drain current of 4H-SiC MOSFETs by adopting a three-dimensional gate structure,"
IEEE Transactions on Electron Devices **56**, pp. 2632-2637 (2009).

D. Other proceedings of international conference

1. W. Saito, I. Omura, S. Aida, S. Koduki, M. Izumisawa, **H. Yoshioka**, and T. Ogura,
"A 20mΩcm^2 600V-class superjunction MOSFET,"
Proc. of International Symposium on Power Semiconductor Devices & IC's, Kitakyushu, Japan, pp. 459-462, May 2004.
2. W. Saito, I. Omura, S. Aida, S. Koduki, M. Izumisawa, **H. Yoshioka**, and T. Ogura,
"Over 1000V semi-superjunction MOSFET with ultra-low on-resistance below the Si-limit,"
Proc. of International Symposium on Power Semiconductor Devices & IC's, Santa Barbara, USA, pp. 27-30, May 2005.
3. W. Saito, I. Omura, S. Aida, S. Koduki, M. Izumisawa, **H. Yoshioka**, H. Okumura, M. Yamaguchi and T. Ogura,
"A 15.5 mΩcm^2-680V superjunction MOSFET reduced on-resistance by lateral pitch narrowing,"
Proc. of International Symposium on Power Semiconductor Devices & IC's, pp. 293-296, Naples, Italy, June 2006.
4. Y. Nanen, **H. Yoshioka**, M. Noborio, J. Suda, and T. Kimoto,
"Improved on-current of 4H-SiC MOSFETs with a three-dimensional gate structure,"
Proc. of International Conference on Silicon Carbide and Related Materials 2008, pp. 753-756, Barcelona, Spain, September 2008.